Magnetic Resonance Imaging in Proximity to Metal Implants at 3 Tesla

Dissertation

zur Erlangung des naturwissenschaftlichen Doktorgrades
der Julius-Maximilian-Universität Würzburg

vorgelegt von

Theresa Bachschmidt
aus Roth

Würzburg 2015

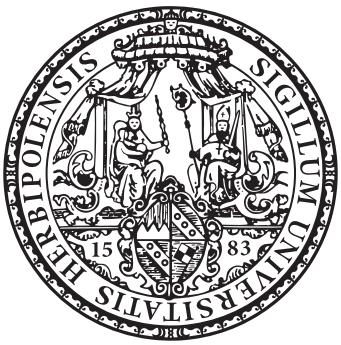

Eingereicht am: 02.07.2015
bei der Fakultät für Physik und Astronomie

1. Gutachter: Prof. Dr. Peter M. Jakob
2. Gutachter: Prof. Dr. Randolf Hanke
3. Gutachter:
der Dissertation

Vorsitzende(r): Prof. Dr. Jean Geurts

1. Prüfer: Prof. Dr. Peter M. Jakob
2. Prüfer: Prof. Dr. Randolf Hanke
3. Prüfer: Prof. Dr. Wolfgang Kinzel
im Promotionskolloquium

Tag des Promotionskolloquiums: 16.06.2016
Doktorurkunde ausgehändigt am:

Abstract

Magnetic resonance imaging is derogated by the presence of metal implants and image quality is impaired. Artifacts are categorized according to their sources, the differences in susceptibility between metal and tissue and the modulation of the magnetic radiofrequency (RF) transmit field. Generally, these artifacts are intensified at higher field strength. The purpose of this work is to analyze the efficiency of current methods used for metal artifact reduction at 3 T and to investigate improvements. The impact of high-bandwidth RF pulses on susceptibility-induced artifacts is tested. In addition, the benefit of a two-channel transmit system with respect to shading close to total hip replacements and other elongated metal structures in parallel to the magnetic field is analyzed.

Local transmit/receive coils feature a higher peak B_1 amplitude than conventional body coils and thus enable high-bandwidth RF pulses. Susceptibility-induced through-plane distortion relates reciprocally to the RF bandwidth, which is evaluated in vitro for a total knee arthroplasty. Clinically relevant sequences (TSE and SEMAC) with conventional and high RF pulse bandwidths and different contrasts are tested on eight patients with different types of knee implants. Distortion is rated by two radiologists. An additional analysis assesses the capability of a local spine transmit coil. Furthermore, B_1 effects close to elongated metal structures are described by an analytical model comprising a water cylinder and a metal rod, which is verified numerically and experimentally. The dependence of the optimal polarization of the transmit B_1 field, creating minimum shading, on the position of the metal is analyzed. In addition, the optimal polarization is determined for two patients; its benefit compared to circular polarization is assessed.

Phantom experiments confirm the relation of the RF bandwidth and the through-plane distortion, which can be reduced by up to 79 % by exploitation of a commercial local transmit/receive knee coil at 3 T. On average, artifacts are rated “hardly visible” for patients with joint arthroplasties, when high-bandwidth RF pulses and SEMAC are used, and for patients with titanium fixtures, when high-bandwidth RF pulses are used in combination with TSE. The benefits of the local spine transmit coil are less compared to the knee coil, but enable a bandwidth 3.9 times as high as the body coil. The modulation of B_1 due to metal is approximated well by the model presented and the position of the metal has strong influence on this effect. The optimal polarization can mitigate shading substantially.

In conclusion, through-plane distortion and related artifacts can be reduced significantly by the application of high-bandwidth RF pulses by local transmit coils at 3 T. Parallel transmission offers an option to substantially reduce shading close to long metal structures aligned with the magnetic field. Effective techniques dedicated for metal implant imaging at 3 T are introduced in this work.

Zusammenfassung

Metallimplantate beeinträchtigen die Funktionsweise der Magnetresonanztomographie und verschlechtern die Bildqualität. Die Artefakte werden entsprechend ihres Ursprungs kategorisiert, in einerseits Suszeptibilitätsunterschiede zwischen Metall und Gewebe und andererseits die Modulation des B_1-Feldes. Im Allgemeinen verstärken sich diese Artefakte bei höheren Feldstärken. Das Ziel dieser Arbeit ist es, die Effizienz vorhandener Methoden zur Artefaktreduktion bei 3 T zu bewerten und mögliche Verbesserungen herauszuarbeiten. Der Einfluss von breitbandigen Hochfrequenz-Pulsen (HF-Pulsen) auf Suszeptibilitätsartefakte wird untersucht. Zusätzlich wird der Einfluss eines Zwei-Kanal Sendesystems auf Abschattungen analysiert, die in der Nähe von Hüftimplantaten und anderen länglichen Implantaten auftreten, welche parallel zu $\mathbf{B_0}$ liegen.

Im Gegensatz zu konventionellen Ganzkörper-Sendespulen erlauben lokale Sende-/Empfangsspulen eine höhere maximale B_1-Amplitude, die breitbandigere HF-Pulse ermöglicht. Die reziproke Abhängigkeit der Suszeptibilitätsartefakte in Schichtrichtung zur HF-Bandbreite wird in vitro für eine Kniegelenkplastik evaluiert. An acht Patienten mit verschiedenen Knieimplantaten werden klinisch relevante Sequenzen (TSE und SEMAC) mit konventionellen und breitbandigen HF-Pulsen in verschiedenen Kontrasten getestet und die Verzerrungen werden von zwei Radiologen bewertet. Eine weitere Studie untersucht das Potenzial einer lokalen Sendespule für die Wirbelsäule. Darüberhinaus werden B_1-Effekte nahe länglicher Metallstrukturen durch ein analytisches Modell beschrieben, das numerisch und experimentell überprüft wird. Des Weiteren wird die Abhängigkeit der optimalen Polarisation des B_1-Feldes, die minimale Abschattung verursacht, von der Position des Metalls untersucht. Für zwei Patienten wird die optimale Polarisation bestimmt und deren Vorteil gegenüber der zirkularen Polarisation analysiert.

Phantomversuche bestätigen die Abhängigkeit zwischen HF-Bandbreite und der Schichtverzerrung, die durch die Verwendung einer lokalen Kniespule mit Sende- und Empfangsfunktion bei 3 T um 79 % reduziert werden kann. Die Artefakte bei Patienten mit Vollimplantaten, bzw. Titanimplantaten, werden als „kaum sichtbar“ bewertet, wenn SEMAC, bzw. TSE, mit breitbandigen HF-Pulsen kombiniert appliziert wird. Im Vergleich zur lokalen Kniespule fallen die Vorteile der lokalen Wirbelsäulen-Sendespule geringer aus; dennoch kann die 3,9-fache HF-Bandbreite der Ganzkörpersendespule erreicht werden. Die B_1-Modulation aufgrund von Metall wird im dargestellten Modell gut wiedergegeben und die Position des Metalls im Objekt hat großen Einfluss auf den Effekt. Die Verwendung der optimalen Polarisation kann Abschattungen stark reduzieren.

Zusammenfassend können Artefakte aufgrund von Schichtverzerrungen durch die Verwendung lokaler Sendespulen und breitbandiger HF-Pulse bei 3 T stark abgeschwächt werden. Die individuelle Wahl der Polarisation des B_1-Feldes bietet eine gute Möglichkeit,

Abschattungen in der Nähe von länglichen Metallstrukturen zu reduzieren, soweit diese näherungsweise parallel zu $\mathbf{B_0}$ ausgerichtet sind. Somit werden in dieser Arbeit wirksame Methoden zur Metallbildgebung bei 3 T eingeführt.

Contents

1 Introduction

Over the last decades, magnetic resonance imaging (MRI) has become an indispensable device in medical imaging and diagnostics. Its principles trace back to 1946, when Felix Bloch and Edward Mills Purcell discovered independently from each other the fundamentals of magnetic resonance (MR) spectroscopy. The foundation for its application in imaging was laid by the introduction of gradient fields and slice selection in the 1970s by Paul Lauterbur and Peter Mansfield. Images of human anatomy followed and after satisfying the demands to enable whole-body MRI, aspirations towards higher field strength started. While first commercially available clinical scanners in the 1980s were based on field strengths of less than 0.5 Tesla (T), 1.5 T scanners are the workhorses in today's clinical routine. Though, benefits of higher field strength are tempting and since the introduction of commercial 3 T scanners in 2001, their market share has increased substantially and whole-body scanners up to 11.7 T are developed for research purposes.

First attempts to fix broken hollow bones and to replace hinge and hip joints were made almost a century before the first clinical MR image. Though, the use of materials like ivory, bone of oxes, resin and nickelized screws failed due to infection. The advent of metal as primary material for implants took place in 1940, when a metallic intramedullary rod and a femoral hip replacement made of a cobalt-chromium alloy were introduced independently by two surgeons. However, indignation arose, as marrow was credited with essential features for the healing of the bone at that time. Good outcomes and compatibility established metal as material for implants. Today's aging population and the expanding obesity in developed countries increase the demand for joint replacements and metal fixtures.

Since MRI is capable of visualizing soft tissue in general and fluid retention and inflammation in particular, this modality is highly attractive to image the surrounding of metal implants. Initial investigations of MRI in the presence of metal were conducted already in the early 1980s, when safety was addressed and MRI was compared to computed tomography (CT). It was noted that image quality was deteriorated significantly by the metal, although degradation was less intense than in the respective CT images. Conductive properties of metal and its magnetic susceptibility can differ significantly from tissue's characteristics and may perturb the homogeneity of different types of magnetic fields, whose homogeneity is essential for MRI. Hence, image artifacts occur. In recent years, several techniques have been suggested to correct artifacts due to differences in susceptibility. Though, artifact compensation focused on scanners with 1.5 T field strength. In general, the intensity of artifacts increases with higher field strength and their correction becomes more challenging, especially in respect of scan time. With the establishment of 3 T in musculoskeletal MRI due to improved diagnostic value in absence of metal, the expansion of techniques for metal artifact reduction to 3 T seems natural. The aim of this work is to assess the efficiency of established methods used for metal artifact reduction at 3 T and to investigate possible

improvements. Techniques dedicated for metal implant imaging at 3 T are presented.

Chapter 2 provides a brief overview of MRI in general and defines fundamental terms required in the following work. Information about common implant types and their applications is given in chapter 3, as well as a detailed analysis of their physical impact on the functionality of MRI. In addition, state-of-the-art techniques for artifact reduction and compensation are described, followed by a comparison of metal implant imaging at 1.5 T and 3 T. Chapter 3 concludes with a critical analysis of the latest techniques for metal implant imaging. A technique to facilitate metal implant imaging at 3 T by the use of local transmit coils is described in chapter 4. Susceptibility-induced artifacts cause distortion during the process of spatial encoding and one type of distortion relates inversely to the bandwidth of the RF pulse. Thus, this distortion can be addressed by the use of high-bandwidth RF pulses, which are enabled by local transmit coils. A phantom study analyzes these effects in detail for a total knee arthroplasty and a commercial local transmit knee coil. A small patient study reveals its clinical impact. This technique is also tested with a prototype transmit coil dedicated for spinal imaging. Chapter 5 addresses current-related artifacts in the presence of hip replacements and femoral intramedullary rods in 3 T MRI. An analytical model describes this effect as a function of multiple parameters and indicates different possibilities to alleviate the resulting degradation of image quality. The model is validated in phantom experiments and by a numerical approach. The polarization of the transmit field is a controllable and very influential parameter on this effect and a patient study demonstrates its significance with respect to artifact reduction. This work concludes in chapter 6 with a general discussion about the clinical acceptance of the techniques presented and further manageable improvements to incorporate metal implant imaging at 3 T into clinical routine.

2 Basics of MR Imaging

This chapter provides a short overview of the physical background of nuclear magnetic resonance (NMR) and its application in clinical imaging (magnetic resonance imaging, MRI). Basic properties of MRI are introduced, as well as advanced hardware and technologies required for this work. Multiple books describe the basics of MRI [11, 25, 40, 70]. If no particular articles are cited in this chapter, these references can be consulted for in-depth information. It is important to note that **B** followed by any index is referred to as magnetic field in MR literature and its amplitude is named magnetic field strength. **H**, normally known as magnetic field, is referred to as "H field"; it occurs only once in this work.

2.1 Physical Background of NMR

The source of MRI is the nuclear spin. Atomic nuclei with nonzero nuclear spin quantum numbers feature an intrinsic angular moment **I**, the nuclear spin. Elements with these types of atomic nuclei can be used for MRI. Due to the high portion of hydrogen nuclei in human tissue, ^{1}H is commonly used in clinical MRI and in this work. Though, other elements with a nonzero spin like ^{31}P, ^{19}F and ^{13}C can be used. A magnetic moment $\boldsymbol{\mu} = \gamma\mathbf{I}$ is linked to the spin; γ denotes the gyromagnetic ratio. If a nuclear spin with a quantized z-component is immersed in a static magnetic field $\mathbf{B}_0 = \mathrm{B}_0\mathbf{e}_z$, the degeneracy of the wave function describing the state of the spin dissipates. According to the Zeeman effect, energy levels are created and their occupation is determined by Boltzmann statistics. Bohr's Correspondence Principle allows the description of large systems by classical calculations, which is valid for NMR due to the high density of hydrogen nuclei in water and tissue. Excessive spins on the lower energy level contribute to the net spin generating a macroscopic magnetization **M**. The equation of motion for this macroscopic magnetization is

$$\frac{d}{dt}\mathbf{M}(t) = \gamma\mathbf{M}(t) \times \mathbf{B}(t) \ . \tag{2.1}$$

It describes the rotation of **M** around the axis of **B** at an angular frequency of $\omega(t) = \gamma\,|\mathbf{B}(t)|$. In the absence of time-varying magnetic fields and static magnetic field inhomogeneities, $\gamma\mathrm{B}_0$ determines the Larmor frequency ω_0. For simplification, the system is considered to be in a frame rotating at Larmor frequency ω_0 about the z-axis. Axes in this frame are indicated by capital letters. Thus, the magnetization remains static in its equilibrium unless static field inhomogeneities $\Delta\mathbf{B}_0$ are present or a time-dependent magnetic field $\mathbf{B}_1(t)$ is irradiated. In case of resonance, i.e. $\mathbf{B}_1(t)$ precessing at Larmor frequency, the magnetization **M** rotates about $\mathbf{B}_1(t)/\mathrm{B}_1(t)$. In this work, $\mathbf{B}_1(t)$ is a vector of time-dependent amplitude and constant orientation in the rotating frame in the plane perpendicular to $\mathbf{B}_0$. This causes

an angular displacement of the net magnetization and the induced flip angle is

$$\alpha = \gamma \int_0^\tau \mathrm{B}_1(t)dt \tag{2.2}$$

for $\alpha \ll 1\,\mathrm{rad}$. This event is known as the irradiation of an RF pulse and it creates transverse magnetization, i.e. magnetization located in the x-y-plane unless α is integer multiples of $180\,^\circ$. Commonly, RF pulses are a temporary event and spins strive for the equilibrium determined by the Boltzmann statistics. During the respective transition from the upper to the lower energy level, energy is emitted and absorbed by the surrounding lattice. This effect delays the movement and is known as spin-lattice relaxation or T_1-relaxation. Immediately after an RF pulse, the magnetization of all displaced spins is coherent. Though, neighboring molecules and spins create local inhomogeneities of the static magnetic field, which cause a spatial variation of the Larmor frequency within a spin ensemble. This results in dephasing of the transverse magnetization and is summarized by the terms spin-spin relaxation or T_2-relaxation. Besides T_2-relaxation, local inhomogeneities $\Delta\mathbf{B}_0$ cause the dephasing of transverse magnetization within a spin ensemble. The total relaxation is described by T_2^*, given by ${T_2^*}^{-1} = T_2^{-1} + \gamma/2\pi\ \Delta\mathrm{B}_0$. Both T_1 and T_2 depend on the medium and the molecules surrounding the hydrogen nuclei and hence differ among tissue types. This can be exploited to generate different contrasts in MRI. The Bloch equation extends the equation of motion (2.1) by the effects of relaxation:

$$\frac{d}{dt}\mathbf{M}(t) = \gamma\mathbf{M}(t) \times \mathbf{B}(t) - \begin{pmatrix} \frac{M_x}{T_2^*} \\ \frac{M_y}{T_2^*} \\ \frac{M_z - M_0}{T_1} \end{pmatrix}. \tag{2.3}$$

Thus, transverse magnetization induced by an RF pulse follows a decay according to $\exp(-t/T_2^*)$ over time t. This behavior is known as *Free Induction Decay* (FID). Though, the dephasing caused by $\Delta\mathbf{B}_0$ can be restored in an echo. Assuming an RF pulse with $\alpha = 90\,^\circ$ to be aligned with the X-axis, the initial coherent transverse magnetization is aligned with Y. An RF pulse with $\alpha = 180\,^\circ$ along the X- or Y-axis mirrors the direction of rotation of the dephasing spins. Assuming an interval of $T_\mathrm{E}/2$ between the $90\,^\circ$- and the $180\,^\circ$-RF pulse, spins will rephase after another period of $T_\mathrm{E}/2$ has elapsed. At this moment, rephased spins form a *spin echo* and cause macroscopic magnetization. Fast alternating magnetic gradient fields can be used for the generation of echoes as well. Those are called *gradient echoes*. The time-varying macroscopic magnetization induces an electromagnetic force in a conducting material enclosing an area, known as receive coil, which can be used as a measure for the signal intensity in MRI. However, this signal intensity does not reflect its spatial origin, but the magnetization of the total volume affected by the RF pulses. Besides the creation of echoes and signal detection, spatial encoding is fundamental in MRI.

2.2 NMR in Imaging

2.2.1 Principles of MRI

The T_2^*-relaxation process causes dephasing of spins due to field inhomogeneities of two sources. Though, dephasing can be controlled and exploited for spatial encoding. In general,

all three directions are addressed by the application of a suitable magnetic gradient field $\mathbf{G}$ modifying the z-component of the static magnetic field at the spatial position $\mathbf{r}$ to $B_z(\mathbf{r}) = \mathrm{B}_0(\mathbf{r}) + \mathbf{G} \cdot \mathbf{r}$. The vector

$$\mathbf{k}(t) = -\gamma \int_0^t \mathbf{G}(t')dt' \tag{2.4}$$

is a measure for the accumulated phase over time t. Assuming that the gradient modulation causes a certain vector $\mathbf{k}$, the resulting signal, which is detected in the rotating reference frame, is given by

$$S(\mathbf{k}) \propto \int_V \rho(\mathbf{r}) \cdot e^{-i\mathbf{kr}} d\mathbf{r} \tag{2.5}$$

for a spin density distribution of $\rho(\mathbf{r})$ in disregard of relaxation effects. Thus, signal is acquired in k-space and the spatial distribution $S(\mathbf{r})$ is obtained by Fourier transform. The time-dependent control of $\mathbf{G}$ in different directions and hence the coverage of k-space is an important issue. In Cartesian k-space sampling, which is used in this work, it is differentiated between two- and three-dimensional image acquisition. In 2D imaging, all RF pulses are accompanied by a gradient $\mathbf{G}_{\mathrm{SS}}$ to select a slice of defined thickness by exciting spins within this slice only. A gradient with half the negative gradient moment of $\mathbf{G}_{\mathrm{SS}}$ is applied for rephasing. Without loss of generality, this process describes the sampling of an axial slice located in the x-y-plane and $\mathbf{G}_{\mathrm{SS}} = \mathrm{G}_{\mathrm{SS}}\mathbf{e}_z$ points in direction of z. For the encoding of each slice, a gradient $\mathbf{G}_{\mathrm{RO}} = \mathrm{G}_{\mathrm{RO}}\mathbf{e}_x$ is switched on simultaneously with the analogue-to-digital converter (ADC) to receive the signal. A preceding gradient along the x-axis with half the negative gradient moment of $\mathbf{G}_{\mathrm{RO}}$ ensures symmetric sampling of k-space's x-component with respect to its zero-crossing. This process is known as readout encoding or frequency encoding. The y-direction is encoded by a phase-encoding gradient $\mathbf{G}_{\mathrm{PE}} = \mathrm{G}_{\mathrm{PE}}\mathbf{e}_y$, which imposes a defined phase on the spins depending on their y-position before the readout. This phase can be restored immediately after the readout. As phase encoding neither can be synchronized with excitation nor with the readout, the y-resolution is a measure for the required numbers of RF pulses and readouts to cover total k-space and thus for the time needed to complete the coverage, depending on selected imaging parameters. This encoding type is prone to folding artifacts: According to the Nyquist condition, aliasing occurs if the object exceeds the field of view (FoV). In general, this applies to the x-direction as well, but additional readout sampling hardly influences the total time needed for coverage. In 3D imaging, the z-dimension is not encoded by slice selection, but by phase encoding. The thickness of the selected slab corresponds to the spatial extent of numerous slices or RF pulses are not selective at all, i.e. they are not accompanied by gradients. Several approaches exist to accelerate the sampling procedure; parallel imaging is widely-used. It exploits the presence of numerous receive coils and includes knowledge about their spatial receive sensitivities in the reconstruction process. Depending on the number and quality of receive coils, subsampling factors are usually below four in clinical routine. The specific method for parallel imaging used in this work is GRAPPA [37].

To summarize the functionality of MRI, the most important components of a clinical magnetic resonance scanner can be listed. A static magnetic field of usually 1.5 T or 3 T and high homogeneity is generated by a superconducting magnet. In its bore, gradient coils are inserted to create time-varying magnetic gradient fields in all three spatial directions. A body coil in shape of a birdcage is located at their inner layer to give rise to the B_1 field, i.e. the RF pulses. All three components are shaped like hollow cylinders with decreasing

diameter. Within the remaining bore, the patient table carries the patient, usually covered with local receive coils. Multiple computers are used to control the scanner, to reconstruct images from the acquired data and to monitor the patient during the exam.

2.2.2 RF Pulses and SAR

The body coil is capable to generate RF pulses, i.e. a time-dependent B_1 field rotating at Larmor frequency in the x-y-plane. A homogeneous spatial distribution of $\mathbf{B}_1(\mathbf{r})$ is desired within the FoV. In slice-selective imaging, a gradient is switched on simultaneously to excite the spins located at a certain position of z. Thus, the temporal change of the amplitude B_1 in the X-Y-plane determines the shape of the excited slice, the *slice profile*. The transition is described by the Fourier transform. In theory, a perfectly SINC-shaped B_1 results in a rectangular-shaped slice profile. Due to time limitations, SINC pulses are truncated, windowed and discretized and the time-bandwidth product (TBP) is an important parameter to determine the quality of the corresponding slice profile. Another RF pulse type commonly used in slice-selective imaging is determined by the Shinnar-Le Roux (SLR) algorithm [96]. In contrast, rectangular RF pulses result in a poor slice profile and are used for non-selective RF pulses only. Though, they allow to generate a specific flip angle within the shortest possible pulse duration (cf. equation (2.2)). The bandwidth f_{BW} of an RF pulse is an important parameter, as it reflects the spectral coverage of the slice profile at full width half maximum. For all three pulse types, the bandwidth increases with decreasing pulse duration.

RF pulses deposit energy in the patient, which is a limitation in clinical imaging. The amount of energy is measured by the *Specific Absorption Rate* (SAR), which is classically determined by the squared amplitude of the electric field linked to the B_1 field multiplied by the conductivity over the mass density of the tissue. For each single RF pulse of the types mentioned above,

$$\mathrm{SAR} \propto {B_0}^2 \, \alpha^2 \, f_{\mathrm{BW}} \tag{2.6}$$

describes the impact of the most important imaging parameters on the SAR, if only one parameter is changed at once. The International Electrotechnical Commission limits the maximum deposited SAR averaged over a tissue mass of 10 g to 10 W/kg and 20 W/kg for the trunk and the extremities, respectively. The whole-body averaged SAR must not exceed 2 W/kg [52].

2.2.3 MR Sequences

Previously, the fundamentals of gradient echoes and spin echoes were introduced. Both types of echoes can be used to generate images of clinical contrasts, when they are integrated in a *pulse sequence*. A pulse sequence describes the interaction of a consecution of RF pulses and gradient fields in combination with the correct timing of the ADC to sample the signal. In gradient echo sequences (GRE), a rather low flip angle is usually selected for excitation ($\alpha_{\mathrm{e}} \ll 90\,^\circ$) and the duration between excitation and the center of the echo is named *echo time* T_{E}. The acquisition of more than one echo is required for spatial encoding and the

individual excitation RF pulses are separated by the *repetition time* T_R. The denotations of the timing also apply to spin echo sequences (SE). Though, neither GRE nor SE are used for MRI in the presence of metal due to their susceptibility to static field inhomogeneities and their long duration, respectively.

Turbo spin echo sequences (TSE) are an advancement of SE. The excitation pulse is not followed by only one, but by multiple refocusing pulses causing not only one echo, but an *echo train*. Each refocusing pulse rephases the dephasing spins due to T_2^* and causes an echo. The total number of refocusing pulses following one excitation pulse is quantified by the *turbo factor* (TF). The amplitude of the transverse magnetization and hence the signal intensity obtained at the n^th echo ($n \leq \mathrm{TF}$) is determined by the time t_e elapsed between the excitation pulse and the n^th echo: $S \propto \exp(-t_\mathrm{e}/T_2)$. As the signal amplitude varies among echoes, this modulation must be considered during k-space coverage to minimize its impact on the contrast of the final image. That is determined mainly by the signal sampled in the center of the k-space; hence, the echo time T_E in TSE imaging does not state the duration between excitation and first echo, but the duration between excitation and the specific echo, which is used to fill the center of the k-space. The previous description of SAR emphasizes the high energy deposition of large flip angles. Classically, spin echoes are generated by a sequence of a 90 °- and a 180 °-RF pulse. Though, in TSE imaging, the SAR deposition is commonly reduced by the use of lower refocusing flip angles, which in turn degrade the signal-to-noise ratio (SNR) and the contrast of the image.

The contrast between different types of tissues can be varied by the sequence timing (T_E, T_R), by RF-pulse properties (flip angle, phase) or contrast preparation modules. Contrasts emphasizing differences in T_1, T_2 and proton density (PD) are commonly used. In addition to these contrasts, the separation of fat from water is usually achieved by the suppression of fat. Methods for fat suppression exploit different physical properties originating from the environment of hydrogen protons in water and lipid. Spectral fat suppression is based on the chemical shift of lipid with respect to water, i.e. its different resonance frequency. In spectral fat suppression, a narrowband RF pulse excites fat only and is followed by a spoiler gradient, which destroys all transverse magnetization by strong dephasing. This module can precede any imaging sequence and does not affect the contrast of that sequence except that signal originating from lipid protons is suppressed. *Short T_1 Inversion Recovery* (STIR) is based on the short T_1-relaxation time of fat compared to water. A 180 °-RF pulse precedes the imaging sequence. As the longitudinal magnetization of lipid protons decays faster compared to water protons, the excitation pulse can be irradiated at the time of its zero-crossing, resulting in the excitation of water protons only. Though, longitudinal magnetization of water protons has decayed as well, resulting in less signal intensity than without the saturation module.

2.3 Polarization of the Transmit Field

The transmit field is generated by a birdcage coil, which is a volume coil. Exceptions like planar transmit coils exist, but are not used in clinical routine at scanners with field strengths of 3 T or less. At these field strengths, the birdcage coil is commonly equipped

with two ports, which are rotated by 90 °. Each of them generates a linearly polarized RF field at the angular frequency ω, which corresponds to the Larmor frequency of the scanner. Without loss of generality, one RF field ($\mathbf{B}_1^x = \mathbf{e}_x \mathrm{B}_1^x \mathrm{e}^{i\omega t}$) is aligned with the x-axis and the other one ($\mathbf{B}_1^y = \mathbf{e}_y \mathrm{B}_1^y \mathrm{e}^{i\omega t}$) is aligned with the y-axis. The ports are fed with a phase difference of $d\varphi$, which is reflected in the total transmit field by

$$\mathbf{B}_1^{\mathrm{sum}} = \mathbf{B}_1^x + \mathbf{B}_1^y \, \mathrm{e}^{-id\varphi} \ . \tag{2.7}$$

Though, not all components of $\mathbf{B}_1^{\mathrm{sum}}$ contribute to the modulation of nuclear spins visible in MR imaging. The MR-effective component $\mathrm{B}_1^{\mathrm{MR}}$ given in the rotating reference frame can be derived by

$$\begin{aligned} \mathrm{B}_1^{\mathrm{MR}} &= (\mathbf{e}_x + i\mathbf{e}_y) \ \mathbf{B}_1^{\mathrm{sum}} \ \mathrm{e}^{-i\omega t} \\ &= \mathrm{B}_1^x + \mathrm{B}_1^y \ \mathrm{e}^{i(\pi/2 - d\varphi)} \ . \end{aligned} \tag{2.8}$$

That field and its spatial homogeneity is decisive for MR imaging, and it is referred to as B_1^+ in literature or simply B_1 in the following. Equation (2.7) suggests an infinite number of polarizations for the transmit field, i.e. possible combinations to generate $\mathbf{B}_1^{\mathrm{sum}}$. However, their effectiveness differs according to equation (2.8). The most effective polarization regarding power consumption is given by $d\varphi = \pi/2$ and $\mathrm{B}_1^x = \mathrm{B}_1^y$, since the power for each channel j correlates to $|\mathrm{B}_1^j|^2$. This polarization is named circular or quadrature polarization and is commonly the only polarization available at scanners with a field strength of 1.5 T or less; a single RF power amplifier with a quadrature power splitter suffices to feed both ports. However, at 3 T field strength and above, the homogeneity of B_1 is deteriorated to an extent which may degrade image quality in patients severely: The wavelength of the RF field at 3 T is approximately 26 cm in human tissue. Tissue's conductive properties lead to an increase of currents due to a higher electric field component associated with the B_1 field at 3 T compared to 1.5 T. These effects derange the penetration of B_1 and result in shading, especially in the abdomen. In that case, polarizations different from circular polarization can be advantageous, as they may result in a more homogeneous spatial distribution of B_1 in the object to be imaged. Therefore, some 3 T scanners are equipped with two RF power amplifiers to enable the individual control of both ports. In the latter case, B_1 homogeneity can be balanced, which is also known as B_1 *shimming*. At field strengths exceeding 3 T, more than two ports can be helpful to generate homogeneous B_1 in a patient. Similar to parallel imaging, which exploits the presence of several receive coils, the use of two or more transmit coils is called *parallel transmission* (pTX). This hardware can also be used for more sophisticated RF pulse techniques, but in this work, it is used for the homogenization of B_1 only. For specific applications like MRI of the knee, dedicated transmit coils exist. Thus, not the body coil is used for transmission. In case of the knee coil, a small birdcage coil usually enables quadrature polarization only. Its diameter is adapted to enclose the average patient's knee.

3 Metal Implants and MRI

This chapter is an introduction to MRI in the presence of metal. The importance and variety of metal implants are illustrated, followed by the physical description of the impact of metal on MRI and techniques to counteract image deterioration. A comparison of the effects at 1.5 T and 3 T follows, before latest research is evaluated and options for improvement are elaborated.

3.1 Metal Implants

This section provides an overview of the prevalence of metal implants and gives detailed information about the most common types and materials.

3.1.1 General Information

Metal implants have become an important element in medical treatment and can be found in various application areas. The main reasons for joint arthroplasties are osteoarthritis, osteoporosis and fractures due to trauma [32] and the most common treatments affect hip and knee joints [117]. However, various other joints can be supported by metal, such as shoulders and elbows and unstable vertebraes can be immobilized by spinal fusion. These types of metal implants are connected to the bone, commonly by cementation, screw-rings or the press-fit technique [41]. Furthermore, fractures can be treated and stabilized with osteosyntheses comprising plates or intramedullary rods, often remaining in the patient for a limited period of time [14, 82].

In the years from 1990 to 2002, the amount of primary total hip arthroplasties (THA) increased by approximately 50 % to 193,000 in 2002 in the USA. The prevalence of total knee arthroplasties (TKA) nearly tripled in the specified 13 years, aggregating 381,000 TKA procedures undertaken in the year of 2002 [65]. An even quicker rise is predicted for the period from 2005 to 2030: In 2030, 572,000 primary THA procedures and 3.48 million primary TKA are projected. This fast increase requires innovations in the fields of implant durability and operative efficiency, as well as increased economic resources [66]. It is important to note that the durability of implants is limited. Abrasion, infection, loosening and dislocation can demand a revision of the joint replacement [13]. Although surgical methods are subject to change in the period from 2005 to 2030, no significant alterations of the revision rates are expected. The revision rate for THA (19.5 % in 2005 and 16.9 % in 2030) represents the more intense implant abrasion and the higher number of failures

compared to TKA (revision rate of 8.5 % in 2005 and 7.7 % in 2030) [66]. Not only the absolute numbers of joint arthroplasties are significant, but also their relevance compared to other surgeries. Considering the number of in-patient operation room treatments in the USA in 2007, arthroplasties of the knee and hip ranked third and seventh, respectively, and spinal fusions were listed at rank ten. The correspondent aggregated costs of those three types of treatments rank among the six most cost-intense operation room procedures and account for 24 billion dollar in total [27]. In regard of the economic burden related to every patient with musculoskeletal disorders, as well as the personal burden, non-invasive imaging methods are very important. The limited implant longevity demands a possibly late initial joint arthroplasty and its substitution at the latest possible and the earliest required. In order to determine the correct point in time to replace an existing implant, the visualization of the surrounding soft tissue of the metal is highly relevant. This requires artifact-free MRI for innocuous clinical diagnoses to provide best care for patients while reducing costs.

3.1.2 Types and Materials

The material of the implant must fulfill certain mechanical properties like hardness and elongation, it must be biocompatible, its surface must allow osseointegration and it must be resistant to corrosion and abrasion. The most common alloys are stainless steel or based on cobalt-chromium (CoCr) or on titanium [94]. Although stainless steel is least expensive and easy to process, its high elastic modulus and its vulnerability to friction limit its use for permanent devices. The high wear-resistance and fatigue strength of CoCr make this material especially suitable for load-bearing components. Titanium features an excellent biocompatibility and a small elastic modulus. It is used for permanent fixed devices and parts of joint replacements, which are not affected by the friction of the joint movement itself [77]. It is important to note, that these alloys are not or hardly ferromagnetic despite the content of cobalt or nickel. Ferromagnetic materials are contraindicated in MRI [10], since such objects can be exposed to strong forces and torques induced by the static magnetic field. These forces can be perilous to the patient. In general, implants can be manufactured of materials other than metal, e.g., ceramic, polymeric or even biodegradable materials [94]. Though, metal is commonly preferred due to its mechanical properties; it is sometimes coated by ceramic to reduce deterioration [98].

Figure 3.1 illustrates common implant types. The total knee replacement in figure 3.1a consists of a tibial and a femoral component being attached to the bone by cementation, while an insert of polyethylene controls the motion of the joint replacement and avoids direct contact of the two metal parts. The base of the tibial component can be of different material than its top and the femoral part, as requirements differ: Titanium enables good contact to the bone, while the mechanical properties of CoCr ensure long-term stability despite strain due to motion. Figure 3.1b shows the composition of a hip replacement. Starting from the bottom, the stem is usually made of titanium with notches or other structures on the surface to create spots for stress concentration. Again, the femoral head is of different material, since it is a load-bearing component. Commonly, either CoCr or ceramics are used and the femoral head is embedded in the acetabular cup. Mechanical properties of hip prostheses with a metallic femoral head and a metallic acetabular cup with no insert separating those components (metal-on-metal hip prostheses) are excellent. However, metallic particles due

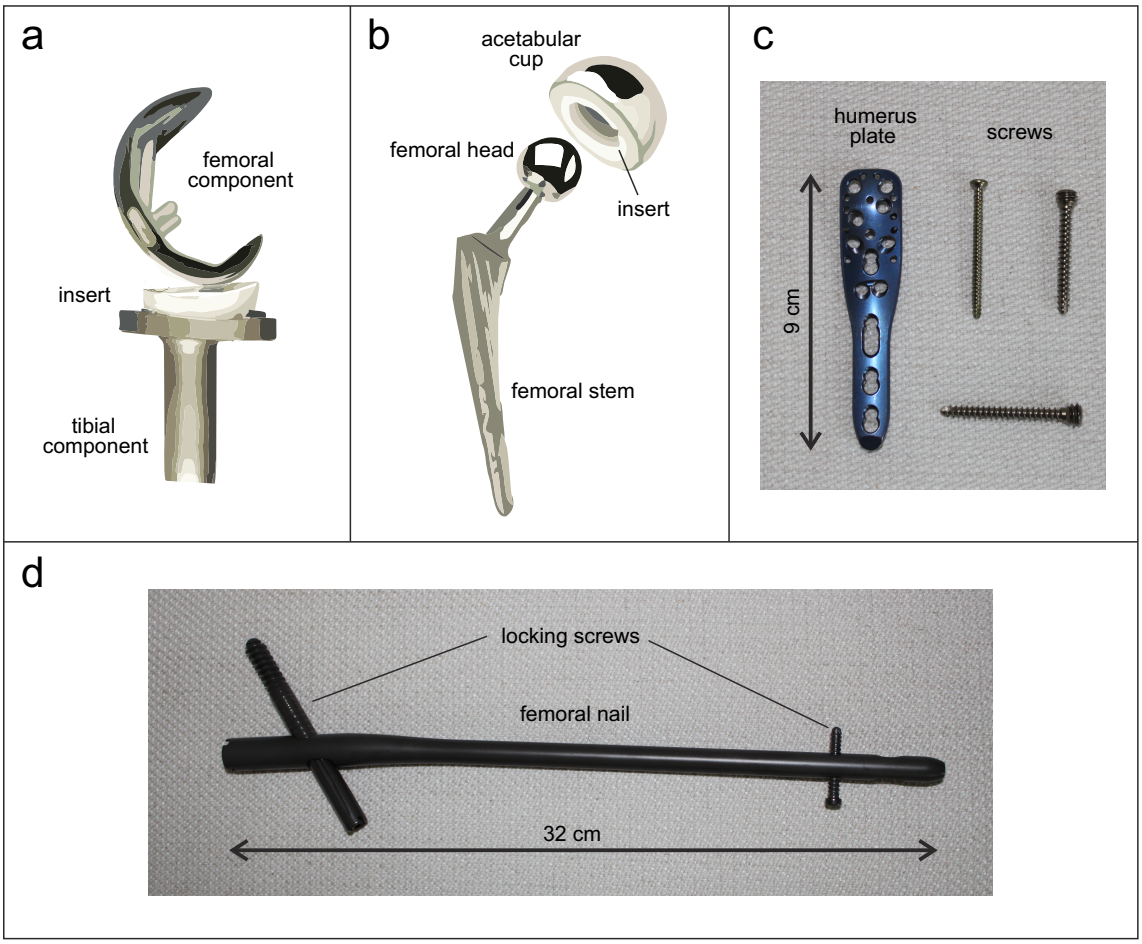

Figure 3.1: Common implant types: total knee replacement (a), total hip replacement (b), a plate and screws for osteosynthesis of the humerus (c) and an intramedullary femoral rod (d).

to abrasion result in an increased rate of failure [83]. To counter this issue, a polyethylene insert usually spaces both components. Figure 3.1c shows a plate used for the osteosynthesis of fractures of the humerus and screws for fixation perpendicular to the plate. The picture in 3.1d illustrates an intramedullary femoral rod, also known as femoral nail or gamma nail. Two titanium locking screws in the area of the femoral head and in distal position prevent its rotation. The structures in 3.1c and d are of titanium and their purpose is to support the correct healing of fractures. Stainless steel can be used as well, but titanium can remain in the body, redundantizing a surgery for the removal.

3.2 Physical Effects of Metal in MRI

The effects induced by metal implants of different types inserted in an MR scanner are summarized in this section. In general, metal-related artifacts are classified according to their sources, which is either a metal-based modulation of the static magnetic field or electric currents induced in the metal.

3.2.1 Modification of B_0

General Considerations

The static magnetic field as seen by the spins of the object determines their precession frequency and its homogeneity is decisive for MRI. Metal, however, introduces significant inhomogeneity: Assuming a homogenous H field in a specified FoV as generated by the superconducting coils of the magnet, the local magnetic field in the object is modified according to its magnetic properties. It is subject to an imposed magnetization

$$\mathbf{M}(\mathbf{r}) = \chi(\mathbf{r})\ \mathbf{H}(\mathbf{r}) \tag{3.1}$$

dependent on the object's magnetic susceptibility χ and the external field $\mathbf{H}$. The total static magnetic field can be calculated according to

$$\begin{aligned}\mathbf{B}_0(\mathbf{r}) &= \mu_0\ \ (\mathbf{H}(\mathbf{r}) + \mathbf{M}(\mathbf{r})) \\ &= \mu_0\ \ (1 + \chi(\mathbf{r}))\ \ \mathbf{H}(\mathbf{r})\ .\end{aligned} \tag{3.2}$$

The magnetic constant is named μ_0 and $(1+\chi)$ is known as relative permeability. Hence, the magnetic susceptibility is the critical physical parameter of the metal influencing the static magnetic field: Rapid spatial changes of χ result in strong local gradients of $\mathbf{B}_0$. Hence, this parameter demands more attention. Table 3.1 summarizes magnetic susceptibilities of tissue and metal types. While the difference between copper and tissue is negligible, it is slightly enhanced for titanium and becomes significant for alloys like CoCr, which is commonly used for the manufacturing of metal implants. The resulting inhomogeneity of

Material	χ [ppm]	Reference
Air	0.36	[104]
Tissue	-7 to -11	[104]
Water	-9.05	[104]
Copper	-9.63	[104]
Titanium	182	[104]
Cobalt-chromium	900	[56]
Cobalt-chromium-molybdenum	1300	[9]
Stainless Steel (non-magnetic)	3500 to 6700	[104]

Table 3.1: Magnetic susceptibility χ of tissue and selected metals.

the static magnetic field can affect the imaging process in different ways. In general, the off-resonance Δf is linked to the difference in susceptibility $\Delta\chi$ by

$$\Delta f(\mathbf{r}) \propto \frac{\gamma}{2\pi}\ \mu_0\ \Delta\chi(\mathbf{r})\ \mathbf{H}(\mathbf{r}) \tag{3.3}$$

and it causes the accumulation of an additional phase of the spins, dependent on the elapsed time t_e

$$\Phi(\mathbf{r}, t_\mathrm{e}) = 2\pi\ \Delta f(\mathbf{r})\ t_\mathrm{e}\ . \tag{3.4}$$

If strong variations of χ occur within a voxel, spins precess at different angular frequencies and dephase, such that the signal intensity of a voxel cancels. This process is known as

intravoxel dephasing. Spectral fat suppression, which relies on the shift of about 220 Hz at 1.5 T between the resonance frequency of fat and water, is highly disturbed by the off-resonances introduced by metal, which are usually in the order of multiple kHz. The linear relation of $\Delta f(\mathbf{r})$ to $\Delta \mathrm{B}_0(\mathbf{r})$ allows the quantification of static field inhomogeneities in both Hertz and Tesla. Usually, the measure of frequency is more convenient.

Failure of Spatial Encoding

The phase-encoding process is not affected by the additional phase Φ, as long as stepped phase encoding is used, i.e. k_y is altered by the amplitude of the phase-encoding gradient G_{PE}, not by its duration t_{PE}. Hence, a constant phase $\Phi(\mathbf{r}, t_{\mathrm{PE}})$ is added to each phase-encoding step, which does not affect the magnitude image obtained by Fourier transform of the k-space data. However, slice selection and signal readout are affected by $\Delta f(\mathbf{r})$. As a consequence, signal is mapped to a wrong spatial position. It has to be differentiated, whether signal is distorted within the imaging plane in 2D imaging or perpendicular to it. The first effect is subsumed by *in-plane distortion*, while the latter one is referred to as *through-plane distortion*.

Following the considerations above, in-plane distortion is caused during the process of signal acquisition, more precisely during the readout process. Since the static off-resonance $\Delta f(\mathbf{r})$ is present throughout the total readout time t_{RO}, the respective phase accumulation can be described by

$$\Phi_{\mathrm{RO}}(x, t_{\mathrm{RO}}) = (\gamma\ \mathrm{G}_{\mathrm{RO}}\ x + 2\pi\ \Delta f(x))\ t_{\mathrm{RO}} \tag{3.5}$$

in a one-dimensional approach for a constant readout gradient amplitude G_{RO}. Equation (2.5) can be simplified by assuming an infinitesimally thin slice, hence omitting the z-component, and it can be expanded by the term comprising $\Delta f(x, y)$:

$$S(k_x, k_y) \propto \int_{xy} \rho(x, y)\ e^{-ik_y y}\ e^{-ik_x(x + \frac{2\pi \Delta f(x,y)}{\gamma \mathrm{G}_{\mathrm{RO}}})} dx\ dy\ . \tag{3.6}$$

The resulting distortion in readout direction Δx due to $\Delta f(x, y)$ is

$$\Delta x = -\frac{2\pi\ \Delta f(x, y)}{\gamma\ \mathrm{G}_{\mathrm{RO}}}\ . \tag{3.7}$$

This equation illustrates that G_{RO} is the only modifiable parameter to directly influence the extent of the in-plane distortion. Usually, the strength of the readout gradient amplitude is reflected in the readout bandwidth, which defines the range of the spectrum sampled by the ADC, and the matrix size in readout direction. As a consequence, the readout bandwidth is commonly given in Hertz per pixel (Hz/Pix), although the term of the parameter suggests a different unit. Conveniently, the in-plane distortion in numbers of pixels can be estimated for a known off-resonance and readout bandwidth given in Hz/Pix.

The excitation of slices, as it is used in 2D imaging, induces through-plane distortion. Assuming an infinitesimally thin slice containing only one spin in z-direction, a spin with an off-resonance Δf would be excited if the spatial frequency modulation due to the slice select gradient $\mathbf{G}_{\mathrm{SS}}$ canceled the off-resonance of the specific spin, i.e.

$$\Delta f(z) + \frac{\gamma}{2\pi} \mathrm{G}_{\mathrm{SS}} \Delta z = 0\ . \tag{3.8}$$

Δz denotes the distance of the off-resonant spin to the desired position of the slice and the equation is a one-dimensional simplification. In a more general approach comprising the influence of the excitation slice profile [80], the amount of the excited spin density $\rho_e(x,z)$ is given by

$$\begin{aligned}\rho_e(x,z) &= \rho(x,z)\ \Gamma\left(\frac{\frac{\gamma}{2\pi}\ \mathrm{G_{SS}}\ z - f_{\mathrm{tr}} + \Delta f(x,z)}{f_{\mathrm{BW}}}\right)\\ &= \rho(x,z)\ \Gamma\left(\frac{z - z_0 - \Delta z}{z_{\mathrm{th}}}\right)\ .\end{aligned} \tag{3.9}$$

z_{th} represents the thickness of the slice, $f_{\mathrm{BW}} = \gamma/2\pi\ \mathrm{G_{SS}} z_{\mathrm{th}}$ the bandwidth of the RF pulse and f_{tr} the transmit frequency, defining the central slice position $z_0 = f_{\mathrm{tr}}\ {}^{2\pi}/_{\gamma \mathrm{G_{SS}}}$ of the excited slice. The direction of phase-encoding (along the y-axis) is neglected due to previous considerations. The function Γ represents the spectral properties of the RF pulse. For an ideally SINC-shaped RF pulse, the spectrum would be rectangular-shaped and

$$\Gamma\left(\frac{f}{f_{\mathrm{BW}}}\right) = \begin{cases} 1 & \text{for } |f| \leq f_{\mathrm{BW}}/2 \\ 0 & \text{else .} \end{cases} \tag{3.10}$$

As a consequence, slices are tilted in the presence of strong field inhomogeneities and can no longer be described as planes. This is illustrated in figure 3.2. For a static field distribution resembling a dipole pattern (figure 3.2a), which can be induced by spherical metal structures like heads of total hip replacements, the distortion of the slice profiles is given for different excitation parameters. Distortion in readout direction is omitted in this consideration and the plane perpendicular to this direction is selected (y-z-plane). Rectangular slices with a thickness of 3 mm are separated by 0.3 mm for better visualization and only six slices are used for demonstration of the impact of the slice select gradient on the distortion. In figure 3.2b, a slice select gradient of 10 mT/m is used. Spins in immediate proximity to the metal are exposed to very high off-resonances and are not covered during the excitation process of the depicted six slices, such that signal voids occur at this location in the final image. According to equation (3.8), the excitation of far-distant slices could cover these off-resonances. Please note, that the spatial gradient of $\mathrm{B_0}$ increases with decreasing distance to the center of the dipole. Hence, the spatial margin in this area decreases with each additional slice on the left and right side of the stack of slices. Figures 3.2e-j illustrate the distorted profiles of the individual slices 1 to 6. The thickness of one slice can vary and the slice itself can be discontinuous and be present at two different locations of z at one position (x,y). The red lines in 3.2f indicate the position and the extent of slice 2 in the absence of off-resonances. If image acquisition follows a conventional 2D acquisition scheme, the distorted slice is projected onto the intended planar slice, as no information about the off-resonance and the resulting distortion is available. In figure 3.2c, the slice-select gradient is inverted compared to 3.2b, such that it decreases from the left to the right side of the selected amount of slices. Due to asymmetric positioning of the stack of slices with respect to the center of the off-resonance, signal void due to insufficient off-resonance coverage is increased significantly on the left side of the stack (white arrow), while coverage of negative off-resonances is improved (black arrow). The effect of the gradient amplitude is visualized in figure 3.2d: Again, six slices are excited with a slice thickness of 3 mm; the slice-select gradient is of same polarity as in image 3.2b, but its amplitude is quadruplicated (40 mT/m). Slices are less distorted compared to 3.2b and signal void in proximity to the

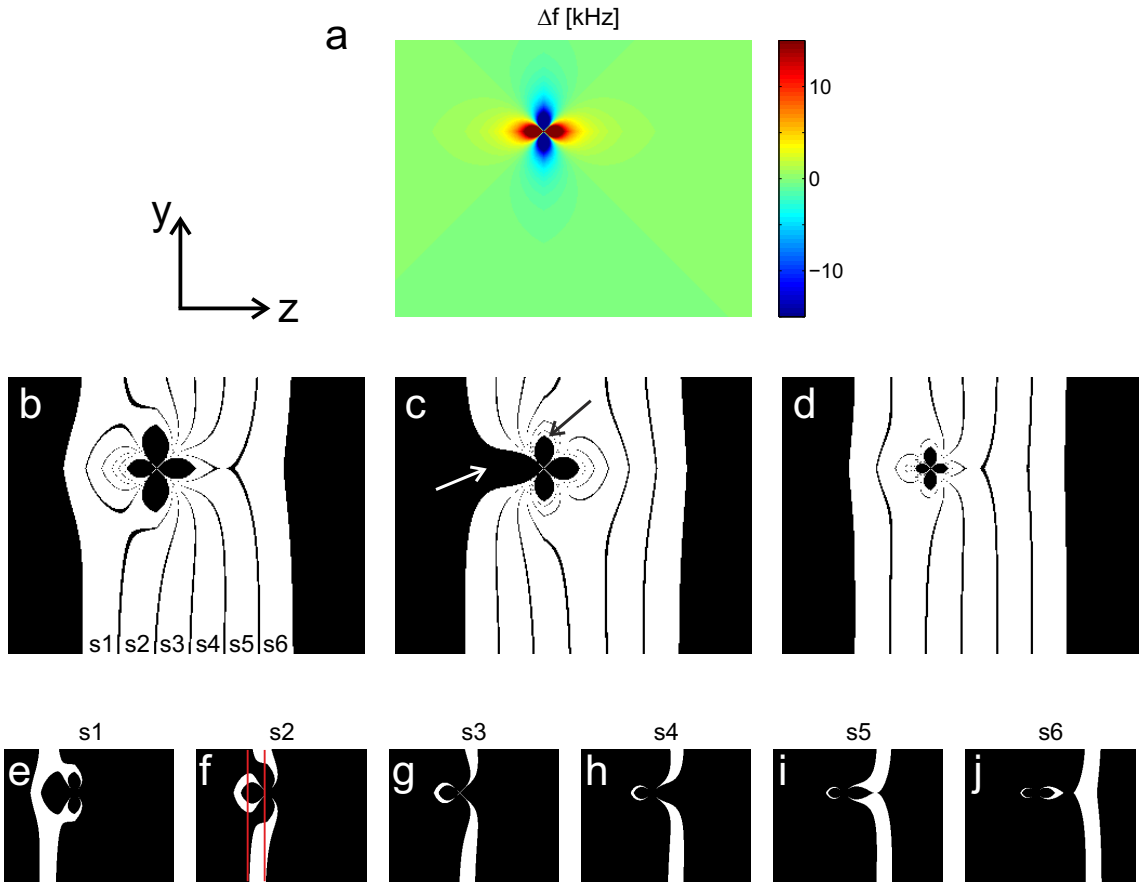

Figure 3.2: Through-plane distortion: Static field map representing a dipole pattern (a); corresponding distorted rectangular slice profiles (thickness 3 mm, inter-slice distance 0.3 mm) of six slices with a slice-select gradient of 10 mT/m (b), −10 mT/m (c) and 40 mT/m (d); white and black arrows in (c) mark signal void due to positive off-resonances and increased signal coverage in the area of negative off-resonances, respectively; (e-j) show the individual slices (s) 1 to 6 for $G_{SS} = 10$ mT/m and the red lines in (f) indicate the borders of slice 2 in the absence of off-resonances.

source of the off-resonance is reduced. Summing up, through-plane distortion is caused by tilted slice profiles due to static off-resonances.

In total, both in- and through-plane distortions and intravoxel dephasing produce areas, where no signal is obtained in plain 2D imaging. This can be either caused by insufficient spin excitation, signal shift during the readout process or pure dephasing. The excitation and readout process can also account for areas with hyperintense signal. These effects superpose and the final image is a mixture of signal voids and signal pile-ups, whose intensities depend on the B_0 inhomogeneities induced by the metal. Figure 3.3 shows TSE images at 3 T of exemplary implant types acquired with conventional protocols, which were not optimized for metal implant imaging. The implants correspond to the arrangements in figures 3.1a-c, except the hip implant, as only the femoral part is imaged. Plastic structures like toy blocks are used for positioning and visualization of distortion. All images suffer from signal voids and signal pile-ups; the artifact intensity differs according to the materials and shapes of the implants. It is also important to note the impact of the alignment of the

implant with respect to the static magnetic field. Signal modulation due to screws in 3.3c shows significant differences between the vertical ones and horizontal one, which are aligned in parallel and perpendicular to $\mathbf{B}_0$, respectively.

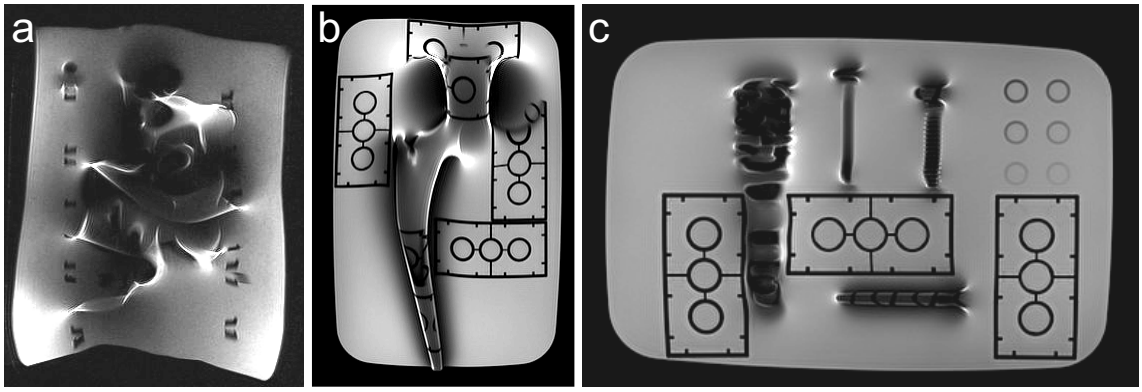

Figure 3.3: TSE images with non-optimized protocols for metal implant imaging: Sagittal view of a total knee arthroplasty of CoCr with a polypropylene insert (a), coronal images of the femoral part of a total hip arthroplasty, whose head is of CoCr and stem is of titanium (b) and of a proximal humerus titanium plate with screws (c). Plastic structures are immersed in all three phantoms.

3.2.2 Modification of B_1

Metal implants feature high electrical conductivity compared to the surrounding tissue and are prone to effects inducing electric current. In MRI, both the RF field and alternating magnetic gradient fields are intuitive sources for currents. The latter one happens at a frequency lower than the Larmor frequency. It merely superimposes temporary inhomogeneities to the static magnetic field and thus results in signal loss due to spin dephasing, which cannot even be recovered by spin echoes due to the temporal modulation of the total static magnetic field [35, 108]. Currents induced by gradient switching do not impact directly the transmit B_1 field and are therefore of minor importance in this work. In contrast, RF-induced currents give rise to a magnetic RF field, which superimposes on the original transmit B_1 field. As a consequence, the total B_1 can cancel at certain positions or it can be multiple times the original one. The flip angles induced by the RF pulses reflect this inhomogeneity, such that hypo- and hyper-intense signal and a spatially varying contrast disrupt the final image. The exact signal modulation depends on the individual MR sequence used. RF-induced currents can be further distinguished by their origins: the electric or the magnetic component of the electromagnetic RF field.

An electric field component is associated with the transmitted electromagnetic B_1 field according to Maxwell's equation [75] and it can be expressed by

$$\mathbf{E}(\mathbf{r}) = \frac{i\omega}{2}\,\mathbf{r} \times \mathbf{B}_1(\mathbf{r}) \tag{3.11}$$

for the vector $\mathbf{r}$ describing the position with respect to the isocenter of the transmit coil. The vectorial notation expresses, that not only the MR-effective component of $\mathbf{B}_1$, but the total transmit field may give rise to the electric field. Dependent on the shape and

the material of the metal, this electric field can apply voltage to the implant and cause an electric current. This current relates linearly to the electric field component and hence depends highly on the position and orientation of the metal inside the object. It is known as directional current.

Independent of the electric field, the component of $\mathbf{B}_1$ perpendicular to the surface of the metal can give rise to a shielding current according to Faraday's law of induction [34]. The cross-section of the metal as seen by $\mathbf{B}_1$ and the skin depth are decisive for this effect. For the example of a wire or a thin rod completely immersed in a medium, the shielding current causes an electromagnetic field in dipolar pattern, attenuating faster with increasing distance to the metal than the one induced by the directional current.

All described forms of shading and distortion and the associated signal voids and pile-ups in the apparent image are summarized as artifacts.

3.3 Methods for Artifact Reduction

The previous section demonstrated a variety of effects in MRI, which originate from the presence of metal. Different approaches exist to reduce or to eliminate the resulting artifacts and these techniques can be categorized according to the sources of the artifacts. There are general guidelines for imaging protocols and methods addressing specific types of artifacts. While susceptibility-induced in-plane distortion can be tackled by techniques, which require minor modifications of imaging sequences and hardly prolong scan time, through-plane distortion demands more sophisticated approaches. This section gives an overview of established techniques for magnetic resonance imaging in proximity to metal. Since B_1 artifacts have been recognized, but have not yet been addressed by techniques for artifact reduction, they are omitted in this section.

3.3.1 General Approaches

In the following, approaches are summarized which do not require special sequences, but are merely a list of standard sequences and protocol parameters which can be selected to decrease metal artifacts [38, 47, 55, 87, 115].

Strong gradients of B_0 result in short T_2^* and can cause intravoxel dephasing, especially prominent in gradient echo sequences. If gradient echo sequences are used, **minimum echo time** is suggested. In contrast, **spin-echo based sequences** benefit from their rephasing capability, such that fully refocused signal at the center of k-space can be expected up to the limit, where the local B_0 gradient is in the range of the readout gradient. While spectral fat saturation is ineffective, the **STIR technique** is not affected by static inhomogeneities, as it is based on the specific relaxation time of fat. The downside of this technique is a lower SNR compared to spectral fat saturation and a prepulse, which increases the SAR deposition.

According to equation (3.7), a **high readout gradient** is beneficial to reduce distortion along the readout direction. It scales inversely with the amplitude of the gradient and involves an increased receive bandwidth of the ADC. For slice selection, equation (3.8) suggests to use a **high gradient amplitude** G_{SS} **during the excitation process**, to limit through-plane distortion for a given off-resonance Δf. For a well-defined RF pulse, an increased G_{SS} reduces the slice thickness, such that either the distance between neighboring slices or the number of slices must be increased to cover the desired anatomy. Again, SNR is decreased by an increased gradient amplitude. **High-bandwidth RF pulses** achieve a similar effect. Figures 3.2b and c suggest another technique to reduce through-plane artifacts: If information about the spatial distribution of B_0 is available, either the polarity of the slice-select gradient or the position of the stack of slices can be optimized to minimize signal voids due to insufficient slice coverage [5]. One approach to avoid distortion during slice selection is the use of **non-selective 3D sequences**, like 3D RARE techniques [50]. Phase encoding in slice direction is not affected by static off-resonances and the readout is the only process prone to distortion. Based on the findings about phase encoding, **single-point imaging** (SPI) is a method to circumvent distortion completely. It employs phase encoding in all three spatial directions, hence uses non-selective RF pulses and the signal readout is not accompanied by a gradient. Additional prepulses can modify the contrast. Though, the drawback of this method is a long acquisition time detaining its application in clinical routine [7, 48, 99]. In general and for imaging techniques other than SPI in particular, the shape of susceptibility artifacts depends on the **orientation of the implant** with respect to $\mathbf{B}_0$ and the direction of frequency encoding. Since in-plane distortion occurs along the readout direction, it is suggested to align this direction with the long axis of the metal such that in-plane distortion along the long edge of the metal is minimized [38]. Elongated metal structures produce least susceptibility artifacts, when they are aligned with $\mathbf{B}_0$ [67]. For an infinitesimally thin and infinitely long metal structure in parallel to $\mathbf{B}_0$, the external field $\mathbf{B}_0$ is not modified according to magnetic boundary conditions. Maximum susceptibility-induced off-resonances can be expected for an orientation of the long axis of the metal perpendicular to $\mathbf{B}_0$. In addition, off-resonances linked to differences in susceptibility become smaller as the strength of the static magnetic field decreases (cf. equation (3.3)). Hence, the related artifacts are less intense at smaller field strength such that 1.5 T clinical scanners are preferred over 3 T scanners for patients with metal implants.

Modifications of B_1 due to metallic objects depend strongly on the individual implant and its location and orientation inside the object and relative to the magnet bore. Neither magnetic or electric RF-induced currents, nor currents due to gradient switching can be predicted without numerical approaches for an arbitrary implant type and there is no universally valid technique to reduce related artifacts. However, for special implant shapes, RF artifacts can be reduced on the basis of the alternation of the transmit field polarization. This topic is investigated later in this work in detail.

3.3.2 Correction of In-Plane Distortion: VAT

Besides the previously mentioned intuitive techniques to limit in-plane distortion, another more complex approach is commonly used to recover this type of distortion. *View Angle*

Tilting (VAT) was initially introduced in 1988 to correct the distortion in readout direction due to the chemical shift between fat and water [20]. Typically, VAT is combined with a selective 2D SE or TSE sequence, minimizing dephasing effects. An additional gradient $\mathbf{G}_{\mathrm{VAT}}$ in slice direction is switched on simultaneously with the readout gradient and its amplitude equals the amplitude of the gradient used for slice selection. The diagram of this modified spin echo sequence is shown in figure 3.4. Figuratively, off-resonant spins with a well-defined distance to the desired slice are excited, because they fulfill equation (3.8). The VAT gradient ensures equal precession frequency of all excited spins during readout to enable a correct correlation between the readout frequency and the position along the direction of readout. In other words, the real direction of readout is no longer aligned with the x-axis, but its orientation is defined by the amplitudes $\mathrm{G}_{\mathrm{VAT}}$ and G_{RO}, introducing a tilted view onto the slice located in the x-y-plane. Without loss of generality, this consideration is valid in case of an axial slice (cf. section 2.2.1). The view angle to describe this effect is given by $\theta = \tan^{-1}(\mathrm{G}_{\mathrm{VAT}}/\mathrm{G}_{\mathrm{RO}})$.

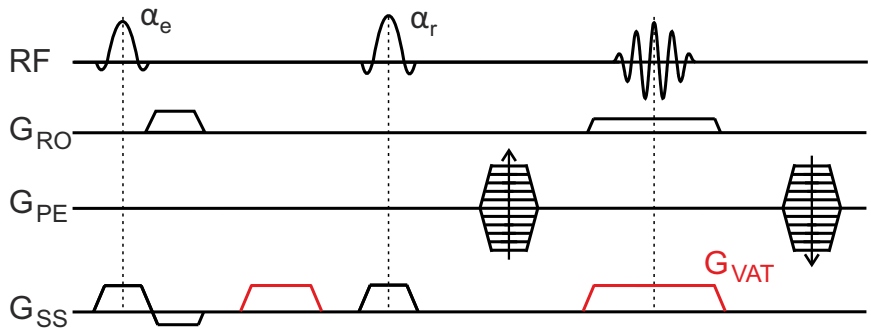

Figure 3.4: Sequence diagram for VAT.

For an analytical explanation, the readout process of the excited spin entity must be considered. Expressing the process of excitation by equation (3.9) and neglecting phase encoding, the signal intensity as a function of the readout time t_{RO} in the presence of a VAT gradient can be expressed as

$$\begin{aligned} S(t_{\mathrm{RO}}) &\propto \int_{xz} \rho_e(x,z)\, \exp\left[i\gamma t_{\mathrm{RO}}\, (x\mathrm{G}_{\mathrm{RO}} + z\mathrm{G}_{\mathrm{VAT}})\right]\, \exp\left[i2\pi\Delta f(x,z)t_{\mathrm{RO}}\right] dx\, dz \\ &= \int_{xz} \rho_e(x,z)\, \exp\left[i\gamma t_{\mathrm{RO}}\, (x\mathrm{G}_{\mathrm{RO}} + z\mathrm{G}_{\mathrm{VAT}})\right]\, \exp\left[-i\gamma t_{\mathrm{RO}}\Delta z(x,z)\mathrm{G}_{\mathrm{SS}}\right] \cdot \\ &\cdot\ \exp\left[i(2\pi f_{\mathrm{tr}} - \gamma z_0 \mathrm{G}_{\mathrm{SS}})t_{\mathrm{RO}}\right] dx\, dz\ . \end{aligned} \tag{3.12}$$

If $\mathrm{G}_{\mathrm{VAT}}$ equals G_{SS},

$$\begin{aligned} S(t_{\mathrm{RO}}) &\propto \int_{xz} \rho_e(x,z)\, \exp\left[i\gamma t_{\mathrm{RO}}\, (x\mathrm{G}_{\mathrm{RO}} + \mathrm{G}_{\mathrm{SS}}\, (z - \Delta z(x,z) - z_0))\right]\, \exp\left[i\ 2\pi f_{\mathrm{tr}}\ t_{\mathrm{RO}}\right] dx\, dz \\ &= \int_{xz} \rho_e(x,z)\, \exp\left[i\left(\gamma \mathrm{G}_{\mathrm{RO}}\left(x + \frac{\mathrm{G}_{\mathrm{SS}}}{\mathrm{G}_{\mathrm{RO}}}\ \delta z(x,z)\right) + 2\pi f_{\mathrm{tr}}\right) t_{\mathrm{RO}}\right] dx\, dz\ . \end{aligned} \tag{3.13}$$

$\delta z(x,z) = z - \Delta z(x,z) - z_0$ reflects the modulation of the slice profile according to equation (3.9) and thus is limited by $\delta z \leq |z_{\mathrm{th}}/2|$. The residual maximum distortion Δx_{max} in readout direction is given by

$$\Delta x_{\mathrm{max}} = \frac{\mathrm{G}_{\mathrm{SS}}}{\mathrm{G}_{\mathrm{RO}}}\ \frac{z_{\mathrm{th}}}{2}\ . \tag{3.14}$$

Comparing this remanent in-plane distortion with the distortion in the absence of the VAT gradient (cf. equation (3.7)), it becomes independent of Δf and its extent is reduced significantly. Irrespective of VAT, the distortion is inverse to the amplitude of the readout gradient. In contrast, higher gradient amplitudes for slice selection are capable of reducing through-plane distortion on the one hand. On the other hand, they possibly introduce higher off-resonances to the imaging process (cf. equation (3.8)), which in turn account for potentially higher in-plane distortion. The VAT gradient introduces an additional term containing the transmit frequency f_{tr} to the readout process, which causes an in-plane shift. When a stack of slices is acquired, each slice needs to be demodulated such that relative phase shifts cancel.

It is important to note, that the VAT technique does not involve an increase in scan time, but it introduces blurring. The tilted view onto the slice blurs sharp edges perpendicular to the slice and a second source is based on the k-space sampling in z-direction during frequency encoding. The subsequent Fourier transform also reflects the slice profile within the slice, which results in blurring. This is comprised in equation (3.13) by the z-dependence of $\rho_e(x, z)$ and $\delta z(x, z)$. Expanding this term in a first-order Taylor-series, a SINC-shaped filter modulates the signal intensity in the x-y-plane [55], outweighing the blur introduced by the view angle [15]; again, a high readout-gradient can soften the effect.

3.3.3 Correction and Reduction of Through-Plane Distortion

In comparison to in-plane distortion correction, techniques restoring through-plane distortion involve a significant prolongation of scan time. The two most common techniques are introduced, followed by a method to limit the impact of through-plane distortion in slice-selective imaging.

SEMAC

According to previous considerations, phase encoding is immune to static off-resonances and can be used to resolve through-plane distortion. *Slice Encoding for Metal Artifact Correction* (SEMAC) [80] combines phase encoding in slice direction (named SEMAC encoding) with a two-dimensional slice-selective VAT-TSE sequence. Each excited slice is additionally phase-encoded with a well-defined number of SEMAC-encoding steps (n_{S}). Figure 3.5 shows the corresponding sequence diagram. The excitation of one slice is followed by the encoding of the k_x-k_y-plane for each of the n_{S} partitions separately, all of them defined by different phase-encoding gradients in z-direction. Each partition is Fourier-transformed and reconstructed individually. Thus, for each position of z, multiple (up to n_{S}) single partitions exist and originate from the excitation of different slices.

This is illustrated in figure 3.6: Referring to the field distortion and the six slices shown in figure 3.2a and b, the effect is demonstrated for five SEMAC-encoding steps symmetric about each excited slice. In reality, both the number of slices and the number of SEMAC-encoding steps would be higher. However, the small numbers are convenient for demonstration pur-

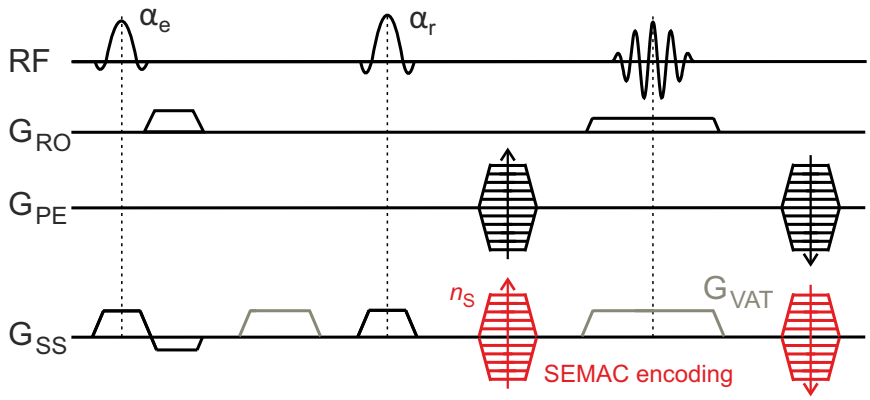

Figure 3.5: Sequence diagram for SEMAC.

poses. The red dashed lines in 3.6c-h indicate the borders of each partition covered by one SEMAC-encoding step in slice direction for the slices 1 to 6. Considering slice 3 in detail (boxed in figure 3.6a), partitions of slices 1 to 5 enclosed by red boxes in figures 3.6c-g locate signal at the position of slice 3. All the signal inside these red boxes is considered for the reconstruction of slice 3. In this work, partitions were combined using a sum-of-squares (SOS) technique to obtain a high signal-to-noise ratio. Further, neighboring slices were selected adjacent to each other for efficient sampling and the thickness of the phase-encoded partitions equaled the thickness of the excited and refocused slices. In general, the latter two parameters are independent of each other. It is important to note, that the SEMAC encoding does not cover all signal excited by slices 4 to 6, visible in figures 3.6f-h. Comparable to phase encoding in-plane, signal not covered during the encoding process aliases and superposes on false positions, leading to signal pile-ups. For example, slice 6 excites signal at the location of slice 3. Due to insufficient SEMAC encoding, this signal is mapped to the position of the imaginary slice 8 and does no longer contribute to slice 3. This results in signal void close to the center of the source of the static field inhomogeneity, although these spins are excited during the excitation process of slice 6. Both the signal void and the aliasing become visible in figure 3.6b, representing the through-plane slice coverage, when SEMAC is applied with 5 SEMAC-encoding steps. The red box indicates the extent of the located stack of slices. In this example, aliasing shifts signal originating from the excitation of slices 5 and 6 outside the stack and signal of slice 4 appears in an area of signal void on the very right end of the stack (arrow in 3.6b). To assign all through-plane distortions to their true position, i.e. to resolve the slices as shown in figure 3.6a, a higher number of SEMAC-encoding steps is required. For the reduction of residual signal voids in areas of extreme off-resonances, a higher number of both excited slices and SEMAC-encoding steps must be provided. If no SEMAC encoding was applied, all distorted slice profiles in figures 3.6c-h would be mapped to the center of the red partitions. In-plane distortion is addressed by the VAT technique.

This example demonstrates the importance of the selection of a sufficient number of SEMAC-encoding steps. However, scan time scales linearly with n_S and high acceleration factors are required. The long scan time involves high SNR which facilitates parallel imaging [46] or compressed sensing [118]. Multiple dedicated receive coils are beneficial in either case. Despite these techniques, scan time can easily hit ten minutes per protocol. Hence, the application of SEMAC in clinical routine is detained by patient comfort, vulnerability to

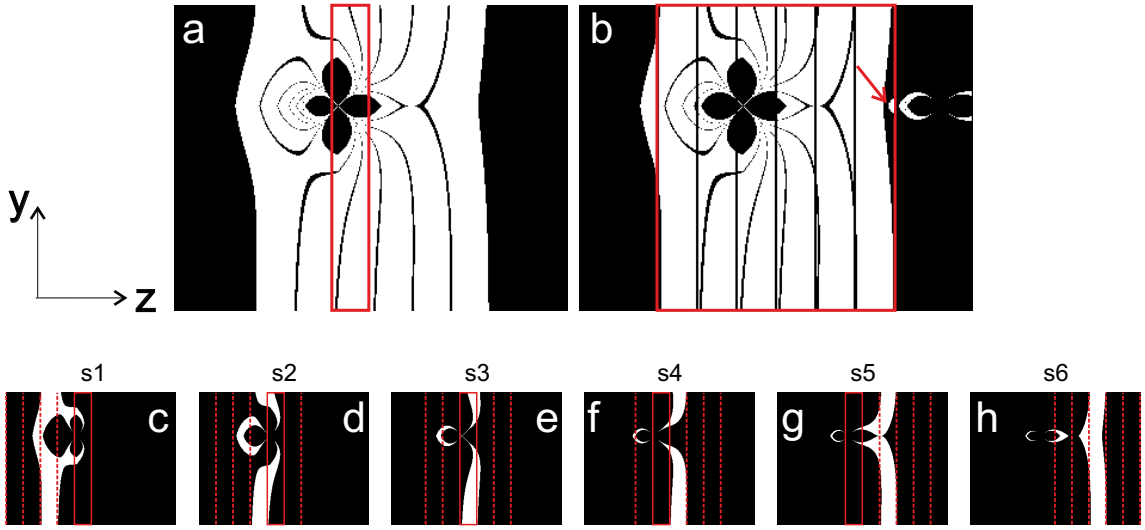

Figure 3.6: The SEMAC-encoding process: (a) 6 distorted slices in the surrounding of the field inhomogeneity given in figure 3.2a; the red box indicates the shape of slice 3 in the absence of inhomogeneity; (b) through-plane coverage with 5 SEMAC-encoding steps; the spatial extent of the stack of slices is boxed in red and the arrow denotes aliasing; (c-h) show the spatial distribution of the signal obtained by the individual slices (s) 1 to 6 and the red dashed lines indicate the borders of the 5 partitions encoded for each slice; the boxed partitions of slices 1 to 5 contain encoded signal belonging to slice 3.

motion artifacts and economic considerations. Another artifact typical for SEMAC arises from the composition of several partitions into one slice. Slices ideally adjacent to each other in the absence of field inhomogeneity can either overlap or be separated by a gap, dependent on the polarity and strength of the gradient of the static magnetic field [44]. This effect occurs particularly in close proximity to metal and depends on the slice profile; it is known as ripple artifact (cf. arrow in figure 3.9g).

MAVRIC

While SEMAC is spatially selective and covers off-resonances dependent on their spatial position, there is also the possibility to exploit directly the spectral properties of the off-resonant signal. As stated in the section of general approaches for metal implant imaging, non-selective 3D sequences are beneficial due to their inherent phase encoding in two dimensions. Hence, non-selective 3D spin-echo-based sequences can be repeated on multiple transmit frequencies to cover a defined spectral range. This is known as *Multi-Acquisition Variable-Resonance Image Combination* (MAVRIC) [61]. Figure 3.7 illustrates this technique.

A non-selective RF pulse approximately flips the spins precessing in the range of its bandwidth. More precisely, the spectral properties of the RF pulse determine the magnitude of the B_1 field, which is imposed on spins precessing with respective frequencies. For the example of a B_0 dipole pattern in the center of the field of view and a perfectly rectangular spectral coverage of the RF pulse, excitation at transmit frequency f_{tr} with an RF

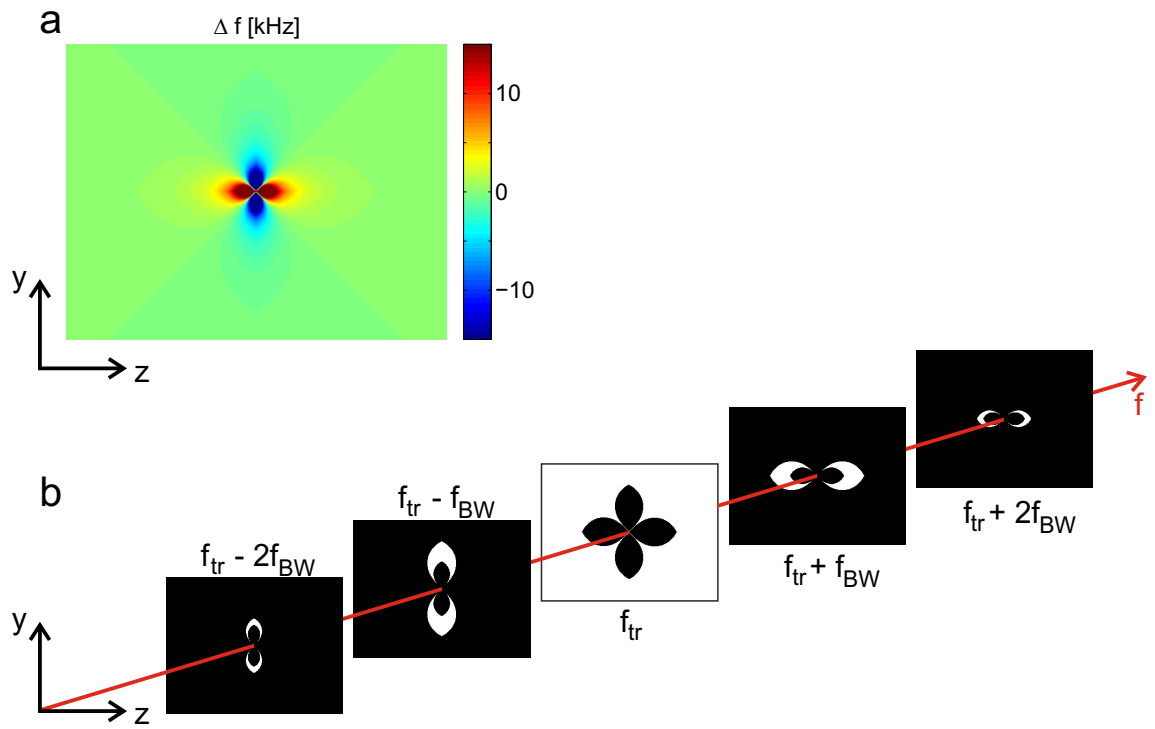

Figure 3.7: The MAVRIC-encoding process (b) visualized for a given spatial distribution of Δf (a).

bandwidth of 1.2 kHz covers the outer areas of the field of view, but not areas of higher off-resonances (figure 3.7b). The transmit frequency corresponds to the spins' Larmor frequency in the absence of off-resonances. To cover higher positive spectral deviations, the spectral coverage of the RF pulse must be shifted. For an ideal rectangular-shaped bin, the adjacent bin is covered by the RF pulse irradiated at the frequency $f_{\mathrm{tr}} + f_{\mathrm{BW}}$. This step-wise acquisition of off-resonant signal can be repeated in positive and negative direction and in each step, the imaged volume corresponds to the total field of view. Usually, areas containing signal become smaller for higher off-resonances, but provide signal closer to the source of the static field homogeneity, i.e. the metal. These multiple volumes must be added to yield an image. Again, transitions between different spectral bins are critical, since real RF profiles are not rectangular and overlap or cause gaps. Various approaches for the selection of the RF profile and for the combination of neighboring bins have been suggested [54, 61] and overlapping Gaussian-shaped bins have proved suitable to ensure homogeneous image reconstruction. In addition, MAVRIC cannot be combined with VAT, since no gradients are applied during slice selection, that can be reversed during the readout process. Hence, distortion in readout direction cannot be addressed by familiar techniques. However, the range of off-resonances capable of inducing this type of distortion is limited according to the bandwidth of the RF pulse, which determines the maximum Δf. Again, metal implant imaging is a trade-off between in- and through-plane distortion: High RF pulse bandwidths increase distortion in readout direction, but reduce the number of required spectral MAVRIC bins to cover a predefined range of off-resonances. The major drawback of MAVRIC lies in the principles of non-selective 3D imaging: Due to phase encoding along two axes, this technique is prone to aliasing, if the FoV is not selected sufficiently large. The extent of the required FoV depends on the part of the body to be imaged and on the coils used. For example, in knee imaging with a dedicated volume coil, the required FoV is

significantly smaller than in hip imaging, where theoretically the total axial cross section of the body trunk must be covered. This impedes the application of MAVRIC to certain parts of the body like hips. To maintain high resolution, the matrix size must be increased, prolonging scan time in addition to the already long scan time of multiple spectral bins. Hence, acceleration techniques are highly important and non-selective spin-echo-based sequences with a high number of refocusing pulses are commonly used. These refocusing pulses often aim for flip angles much smaller than 180 ° for SAR reasons, approximating the desired contrast by advanced techniques developed for RARE imaging [1, 49]. Thus, the contrast of MAVRIC becomes prone to variations of B_1, especially visible in areas of overlapping spectral bins. In addition to the missing correction of in-plane distortion, long echo trains introduce blurring.

An improvement of MAVRIC with respect to applicability is based on a version of a slab-selective 3D sequence. The development consolidates elements of both MAVRIC and SEMAC and is known as MAVRIC-SL or MSVAT-SPACE [54, 72]. In contrast to SEMAC, selective RF pulses do not excite a single slice, but a stack of slices (slab), which is phase-encoded in slice direction. This opens its scope of application to all parts of the body, allows VAT for distortion correction in-plane and benefits from the long echo train of a 3D sequence. Though, disadvantages of MAVRIC regarding blurring and contrast behavior are not addressed by hybrid techniques. Thus, SEMAC is favored in this work. All these techniques mentioned in this paragraph, including SEMAC and MAVRIC, are subsumed by the term *Multispectral Imaging* (MSI).

Off-Resonance Suppression

In spin-echo imaging and variations of it like VAT, slice-selective RF pulses are used. According to equation (3.9), the gradient $\mathbf{G}_{\mathrm{SS,e}}$ accompanying the slice-selective RF pulse used for excitation is decisive for an off-resonant spin to be excited or not. The same applies to the refocusing process and the gradient $\mathbf{G}_{\mathrm{SS,r}}$; spins both excited and refocused contribute to the final image only. Usually, gradients used for excitation and refocusing match. Though, in general, gradient amplitudes are individual parameters, which can be used for *Off-Resonance Suppression* (ORS) [43]. This technique can be applied to any spin-echo based imaging technique employing slice-selective excitation. A maximum off-resonance can be defined by the selection of the ratio of the gradients, such that spins exceeding this off-resonance do not form an echo, irrespective of their distance to the center of the desired slice. This cutoff-frequency Δf_{cut} shall define a spectrum symmetric to the transmit frequency f_{tr} and can be derived from equations (3.8) and (3.9) with different gradient amplitudes $\mathrm{G}_{\mathrm{SS,e}}$, $\mathrm{G}_{\mathrm{SS,r}}$ and RF pulse bandwidths $f_{\mathrm{BW,e}}$ and $f_{\mathrm{BW,r}}$ for excitation and refocusing, respectively. The excitation process shall fulfill the lower and the refocusing process the upper boundary frequency condition:

$$\Delta f_{\mathrm{cut}} = \frac{\gamma}{2\pi}\ \mathrm{G}_{\mathrm{SS,e}}\ \Delta z_{\mathrm{cut}} - \frac{f_{\mathrm{BW,e}}}{2} \tag{3.15}$$

$$\Delta f_{\mathrm{cut}} = \frac{\gamma}{2\pi}\ \mathrm{G}_{\mathrm{SS,r}}\ \Delta z_{\mathrm{cut}} + \frac{f_{\mathrm{BW,r}}}{2}\ . \tag{3.16}$$

Δz_{cut} is an auxiliary variable and it defines the maximum distance to z_0, which is both covered during excitation and refocusing. Thus, for an intended slice thickness z_{th} equal for

both excitation and refocusing, the cutoff-frequency is given by

$$\begin{aligned}\Delta f_{\text{cut}} &= \frac{\gamma}{2\pi}\, z_{\text{th}} \left(\frac{1}{\text{G}_{\text{SS,r}}} - \frac{1}{\text{G}_{\text{SS,e}}} \right)^{-1} \\ &= \left(\frac{1}{f_{\text{BW,r}}} - \frac{1}{f_{\text{BW,e}}} \right)^{-1} . \end{aligned} \tag{3.17}$$

Figure 3.8 visualizes the effect: Both spectral bins for excitation and refocusing are aligned, when equal gradients are used (a). Minor deviations occur due to different slice profiles. For different gradient strengths (b), both spectral bins cover the z-range given by the slice thickness in the absence of off-resonances. With increasing off-resonance, the overlapping area fades out and ceases at the cutoff-frequency.

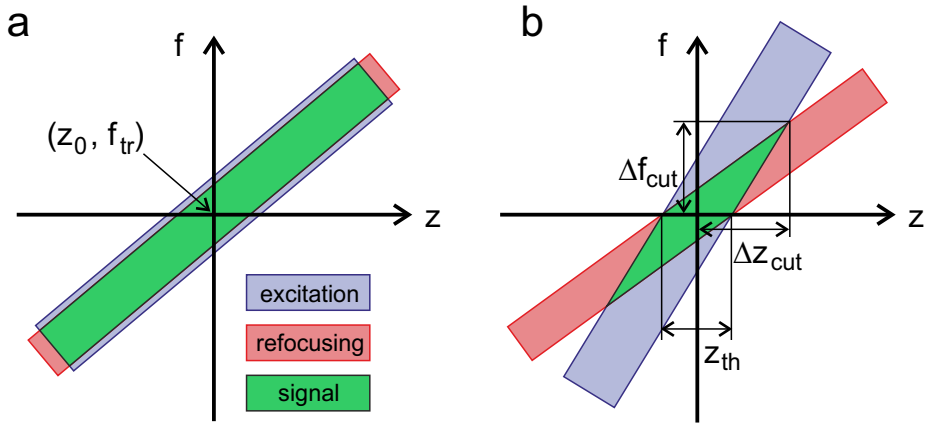

Figure 3.8: Off-resonance suppression: (a) equal gradients for excitation and refocusing lead to maximal overlapping spectral bins; (b) different gradients ($\text{G}_{\text{SS,e}} > \text{G}_{\text{SS,r}}$ in this example) both cover the slice thickness at the transmit frequency, but the respective bins diverge for off-resonances; if a spin's resonance frequency is outside the range of $f_{\text{tr}} \pm \Delta f_{\text{cut}}$, it can either be excited or refocused or none of both, such that it does not generate any signal.

The process of slice selection allows regions in far distance to the desired slice to be projected onto this, if they are exposed to sufficiently strong off-resonances. This can occur in TSE and in VAT imaging, for example, where no through-plane correction is performed. Hence, it is reasonable to detain signal from projection, as clinical misinterpretations are encouraged by strongly dislocated signal. Even when through-plane distortion is corrected, the techniques' acquisition times usually relate linearly to the covered through-plane distortion. A cutoff-frequency, hence a maximum possible distortion, guarantees the absence of projected signal, if the respective spectral range is covered by an MSI sequence. Similar to VAT, ORS does not prolong scan time and it is intuitive to implement without the need for dedicated post-processing.

Following the spectrum from the transmit frequency f_{tr} to $f_{\text{tr}} \pm \Delta f_{\text{cut}}$, the amount of spins possibly being both excited and refocused declines from the spin quantity within a total slice thickness to zero. Combining ORS with SEMAC to restore signal in the range of $[f_{\text{tr}} - \Delta f_{\text{cut}};\ f_{\text{tr}} + \Delta f_{\text{cut}}]$, ORS degrades the homogeneity of the composite slice in addition

to the discontinuities among neighboring partitions, especially in areas of high off-resonances close to either end of the spectral range. It is important to select a sufficiently large cutoff-frequency, reflected in the required number of SEMAC-encoding steps. The smaller the number of SEMAC partitions is, the more ringing and ghosting artifacts in- and through-plane are introduced by their Fourier transform, further increasing signal inhomogeneity.

Figure 3.9 visualizes the effects of different methods for artifact reduction at 3 T for a TKA (a-d) and the femoral stem of a THA (e-h). The non-optimized TSE images of these exact setups are shown in figures 3.3a and b, respectively. Compared to these two images, excitation and readout bandwidth are increased in the first column in figure 3.9. The spatial extent of artifacts is reduced in both cases. In the second column, VAT is applied additionally. Image quality of the TKA (figure 3.9b) is not improved, while in-plane distortion of the plastic structures is visibly suppressed in the image of the THA (arrow in f). SEMAC covering ±5.1 kHz (third column) reveals the shape of both the TKA and THA, still suffering from signal voids, aliasing and ripple artifacts (arrow in g). In the last column, SEMAC is combined with ORS, introducing a cutoff-frequency of 5.1 kHz. For the TKA, folding artifacts are replaced by signal voids and the area of signal loss is increased for both implant types compared to the pure SEMAC acquisition.

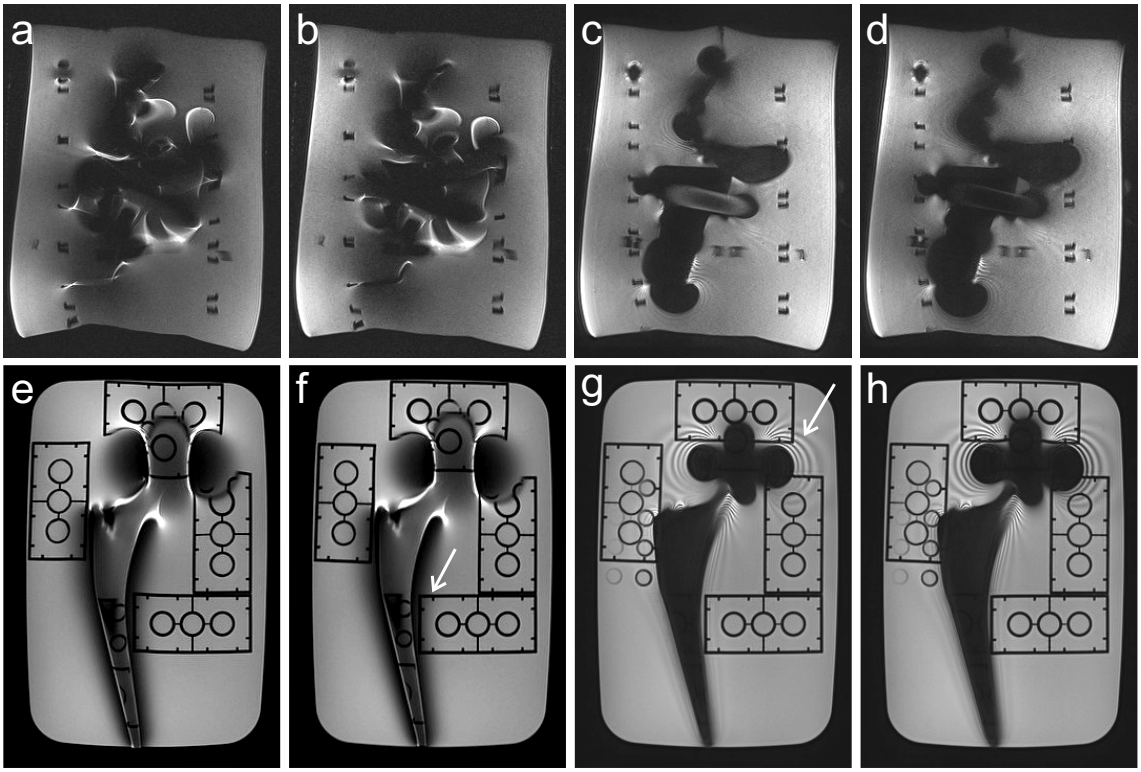

Figure 3.9: Visualization of different artifact reduction techniques for a TKA (a-d) and THA (e-h): TSE with bandwidth optimization (a,e), VAT (b,f), SEMAC covering ±5.1 kHz (c,g) and SEMAC combined with ORS with a cutoff-frequency to match the spectrum covered by SEMAC (d,h); arrow in f indicates in-plane distortion correction, arrow in g shows ripple artifacts; non-optimized images of these slices are shown in figures 3.3a and b.

3.3.4 B_0 Mapping in the Presence of Metal

Aggravated spatial encoding suggests the determination of off-resonances prior to the imaging process and to consider this information in a post-processing step, as known from EPI imaging [18, 53, 55]. However, steep gradients of B_0, e.g. occurring close to full joint replacements of materials other than titanium, cannot be unwarped in this process. The acquisition of undistorted field maps is time-consuming. Still, methods for the acquisition of a full field map based on MSI techniques are introduced, as one investigation in the following chapter is based on such a technique. To determine the range of off-resonances related to one slice, not a full field map, but a scout scan might suffice. Such a sequence is less time-consuming than the acquisition of a full field map and it can be used for the prior determination of the range of off-resonances to be covered during SEMAC or MAVRIC.

B_0 Mapping using MSI Techniques

The SEMAC sequence aims for undistorted clinical images by mapping off-resonant signal to its correspondent partitions in slice direction. Signal of several partitions $S^p(\mathbf{r}_i)$ contributes to the total signal $S(\mathbf{r}_i)$ of slice i at the position $\mathbf{r}_i = (x_i, y_i)$ in-plane. The signal $S^p(\mathbf{r}_i)$ originates from the image acquisition and SEMAC encoding of slices other than slice i, except the central partition of slice i. Each partition p can be assigned not only a spatial deviation from the center of the excited slice (Δz^p), but also an off-resonance Δf^p within the accuracy of the bandwidth of the RF pulse f_{BW}. This information can be used for the generation of a B_0 field map. In general, more than one partition contains signal at position $\mathbf{r}_i$ due to imperfect slice profiles. Interpolation of the off-resonances according to the relative signal intensity in each partition at position $\mathbf{r}_i$ increases accuracy and dilutes the incremental illustration. To further increase precision, RF pulses with rectangular spectral profiles and small RF bandwidths shall be used. For the efficient coverage of a large spectral range, high-bandwidth RF pulses are suitable. In either case, a large number of SEMAC-encoding steps is required to ensure the coverage of all occurring off-resonances and hence to avoid aliasing. The resulting scan time can easily exceed half an hour for total joint replacements, which is too long for its application in vivo. This technique cannot be used for a preliminary investigation in clinical routine, but for scientific experiments with phantoms. Based on the data obtained during a MAVRIC sequence, the B_0 field map can be determined in a similar approach [54].

A Scout for Off-Resonance Detection

Different approaches have been presented to quickly assess the approximate range of off-resonances in the presence of metal implants [6, 45, 71, 95]. Compared to common B_0 field-mapping techniques, which are usually implemented for a range of few hundred Hz, off-resonances up to several kHz must be detectable. The acquisition of the spectrum of a slice by turning off phase encoding and the readout gradient [45] gives a rough idea of the metal-induced off-resonances for each slice. Another technique is a refinement of this method such that the spectrum not of the total slice, but of each phase-encoding step is

projected: A conventional spin echo sequence is equipped with a readout gradient not along the direction of the conventional readout, but along the direction of slice encoding [6, 71]. The individual selection of the resolution in direction of phase encoding allows a trade-off between acquisition time and precision. At last, a SEMAC sequence accelerated by the omission of in-plane phase encoding can be used to assess relevant off-resonances. The resulting projected signal intensity in each partition is a measure for the distortion and hence the induced off-resonance [95].

The challenge of these scout scans is not their acceleration, but the post-processing of the projected data. Noise as well as the individual, sometimes bulk and discontinuous occurrence of off-resonances complicate the determination of a threshold. As a consequence, these techniques are not sufficiently robust for clinical routine yet.

3.4 Comparison 1.5 T vs. 3 T

Previous sections describe the effects during magnetic resonance imaging caused by metal and methods to reduce and correct the related artifacts. Most effects are linked to the strength of the static magnetic field. Their impact on the imaging process at 3 T is compared to 1.5 T in this section. Although metal implant imaging at 3 T appears much more complex than at 1.5 T, several issues motivate the improvement of applications for this field strength.

Considering the modulation of the homogeneity of the static field in the presence of metal, the absolute deviation of the resonance frequency Δf scales linearly with the strength of the static field, assuming the susceptibility to be independent of external magnetic and electromagnetic fields. For a constant readout gradient, the spatial in-plane distortion is proportional to Δf and hence to the field strength. Though, the increased SNR at higher field strength allows faster signal collection in readout direction to limit in-plane distortion. The VAT technique is not affected by the field strength, but high readout gradients are also beneficial to this technique to limit the residual distortion and the filter effect. Not only the spatial in-plane distortion, but also the through-plane distortion is proportional to Δf and thus to the field strength. However, increased SNR at higher field strength allows for thinner slices. According to

$$2\pi f_{\mathrm{BW}} = \gamma \, \mathrm{G}_{\mathrm{SS}} z_{\mathrm{th}} \, , \tag{3.18}$$

thinner slices require a higher gradient amplitude for slice selection, when the RF pulse and thus its bandwidth remains unchanged, and limit shifts through-plane. This is beneficial in TSE and VAT imaging, when no through-plane correction is performed and slices can be selected to have gaps in between. In SEMAC encoding, though, slices need to be adjacent or overlapping such that a higher number of slices is required to cover the desired anatomy compared to the use of thicker slices. The imaging of more slices commonly involves an increase of acquisition time, as SEMAC protocols usually hit the SAR limit. In addition, keeping the spatial extent of SEMAC partitions equal to the slice thickness will not change the number of required SEMAC-encoding steps and thus the scan time, as compared to the use of thicker slices. RF pulses with higher bandwidths decrease spatial distortion on the one hand and increase spectral coverage during SEMAC encoding on the other hand, such that

less SEMAC-encoding steps are required as compared to RF pulses with lower bandwidths. Higher RF pulse bandwidths commonly involve a shorter pulse duration, which increases the specific absorption rate additionally to the higher field strength. In general, this approach is of limited effectiveness due to safety regulations. In 3D-imaging techniques like MAVRIC, the higher level of perturbation of B_0 at 3 T requires a higher off-resonance coverage in the spectral domain. This can be tackled by an approach combining an increased RF pulse bandwidth, also facing the limits of SAR, with a larger number of acquired spectral bins, prolonging scan time.

Although the change of susceptibility-related effects is the most obvious when proceeding to higher field strength, the Larmor frequency increases as well and hence the transmit frequency of the magnetic RF field. Thus, the associated electric field component increases and applies a possibly higher voltage to the metal, rising the induced current. For elongated metal structures like guidewires, needles and intramedullary rods, resonance effects can occur independently of their orientation. Significant impact can be expected for wire lengths in the range of half the wavelength of the transmit RF field [34, 102]. In tissue, the wavelength is approximately 52 cm at 1.5 T and it is halved at 3 T, such that the resulting resonance length is about 13 cm. Hence, both guidewires and intramedullary rods can give rise to resonance effects, causing severe flip angle modulations during the imaging process. Shielding currents induced directly by the B_1 field perpendicular to the surface of the metal according to Faraday's law of induction decrease at higher field strength: Usually, the magnitude of B_1 does not depend on the field strength, though RF pulses imposing less SAR on the patient may be required at higher field strength, involving a lower peak B_1. The skin depth decreases for higher frequencies, such that less shielding currents can be expected. However, irrespective of the field strength, the impact of this effect is minor compared to the other two sources. The entity of currents is assumed to increase at higher field strength and inhomogeneity of B_1 is expected to become more prominent. Currents in metal implants can cause heating due to a local increase of the electric field, which correlates with the local SAR [2, 24, 89, 97]. Hence, the risk of local burning is enhanced for patients and monitoring is difficult [12, 36].

In general, SAR is a limiting factor in imaging at high field strength. Additionally, techniques for metal artifact correction like SEMAC are very demanding with respect to SAR, as spin-echo-based sequences use refocusing pulses with high flip angles and a dense succession of RF pulses is needed to cover a sufficient spectral range. Usually, SAR is a limiting factor in protocol development and an artificial prolongation of the imaging protocol is required. Comparing 3 T to 1.5 T, the inherent SAR associated with one RF pulse is quadruplicated and techniques for the reduction of SAR become more prominent at 3 T. One efficient option is the reduction of the flip angles of the refocusing pulses, since they account for the majority of the total SAR due to their high share in total RF pulses in TSE-based sequences. Though, contrast and SNR are affected [1, 49].

In addition to the limitations arising from the imaging sequences, not only the magnet generating the static field, but other hardware components change and may oblige to stricter limits. For example, body coils of commercial scanners may be designed to achieve less peak B_1, as SAR limitations hamper the exploitation of the maximum B_1 at higher field strength. The general SAR deposition may also vary for different hardware designs.

Despite the difficulties arising from metal and their intensification at 3 T compared to 1.5 T, MRI benefits from other advantages of higher field strength, also in the presence of metal. For example, the increased SNR and higher resolution are advantages of 3 T over 1.5 T and already in 2007, Kuo et al. stated that "state-of-the-art musculoskeletal MRI is moving to 3 T" [64]. Advantages of 3 T over 1.5 T MRI have been reported for various orthopedic issues [106, 107, 116] and 3 T is becoming more established in clinical routine. There are dedicated orthopedic practices and freestanding imaging centers, which may own only one MR scanner. Dedicated for musculoskeletal imaging, a field strength of 3 T is beneficial with respect to image quality and economic considerations. It is important that all patients of those imaging centers can benefit from the better diagnostic quality at 3 T and that these sites do not have to reject patients with metal implants. Hence, it is important to equip 3 T scanners with options to improve image quality in proximity to metal implants and to minimize related artifacts.

3.5 Recent Developments in Metal Implant Imaging

Investigations of MRI in the presence of metal go back to the beginning of the 1980s and the previously presented methods have been developed since then. However, the wide clinical availability of 3 T scanners and the increasing amount of metal joint replacements demand dedicated techniques. This section discusses state-of-the-art methods and their effectivity at 3 T to infer options for improvement.

Technical Developments

The general approaches presented in section 3.3 comprise merely specific protocol parameters and guidelines for patient positioning originating from the early years of metal implant MRI. The use of spin-echo-based sequences is suggested over GRE sequences to avoid intravoxel dephasing. Improved hardware performance of recent years allows gradient-echo imaging with very short echo times, also known as *Ultrashort* T_E (UTE) imaging [101]. Radial center-out k-space sampling immediately after the RF pulse has ceased allows signal acquisition during the FID. Its primary advantage is the possibility of visualizing tissues with short T_2-relaxation times like tendons, ligaments, cortical bone and dental enamel. Signal of these tissues cannot be detected by means of spin-echo-based MRI. Magnetization preparation RF pulses preceding the excitation RF pulse can modulate the contrast. The short lapse of time between RF excitation and readout minimizes intravoxel dephasing due to static off-resonances. The off-resonance spectrum covered by the 3D UTE sequence can be increased by a consolidated UTE-MAVRIC sequence [17]. In comparison to the original MAVRIC, this sequence is not based on a non-selective 3D spin echo sequence, but on non-selective 3D UTE. Its contrast is unique and not yet established in clinical routine. In addition, radial sampling increases scan time and its non-selective properties are a drawback for certain joints.

Not only UTE, but also SPI techniques benefit from the possibility to visualize tissues with very short T_2 values. First investigations of SPI in presence of THA were conducted in

vitro already in 2003 [99]. Although signal voids close to metal were negligible, scan times of several hours detained further investigations in vivo. Besides parallel imaging, recent advances in sub-Nyquist sampling of MRI data, e.g. compressed sensing [81], facilitate acceleration of MR data acquisition. In addition, several recent publications have risen the awareness of the limitations imposed by the process of frequency encoding [44, 60, 110]. As frequency encoding is redundant in SPI, these facts motivate new approaches. However, recently published studies [3, 4, 33, 62, 100] are still in the early stage of development and face challenges like insufficient resolution, insufficient off-resonance coverage and too long acquisition times. The most mature approach is based on a spectrally-resolved fully phase-encoded (SR-FPE) 3D TSE sequence combined with a multiband RF pulse technique enabling a broad spectral coverage reasonably fast [3, 4].

Regarding the VAT technique, the analysis of the main source of blurring, the low-pass filter, was the accomplishment of highest impact about ten years ago [15]. The related suggestion to use multiple readouts has not found its way into clinical routine. A propeller readout has been suggested as another technique for efficient deblurring, though increasing scan time [73]. Recently, a spiral trajectory for k-space sampling proved suitable for the combination of VAT with a 3D spin echo sequence [121]. Still, VAT and the use of a high readout gradient are the only techniques to address in-plane distortion. As through-plane distortion is more complex and time-consuming, recent research focused on this source of artifacts.

The long acquisition time of MSI techniques, which correct through-plane distortion, are their main drawback. Thus, methods for acceleration have been exploited. While early conference contributions proved the compatibility of MAVRIC with parallel imaging [19] and compressed sensing [57], a wider range of acceleration techniques has been investigated for SEMAC. First publications exploited parallel imaging and partial Fourier for SEMAC [46], as well as combinations with compressed sensing using different sparsifying transforms [78, 88, 118]. The results look promising and scan time reduction is attractive. Though, a large variety of parameters demanding further optimization and the long duration required for reconstruction still hamper its use in clinical routine.

A different approach accomplishing a scan time reduction of 40 % is named “adaptive SEMAC” [45]. This technique deploys the linear relation of the through-plane distortion to the thickness of the excited slice. Based on a scout scan, the off-resonances of all evenly distributed desired slices are determined. Subsequently, an algorithm adapts the slice widths for a given desired off-resonance coverage, such that each slice spans an approximately equal spectrum. Despite the additional acquisition time for the scout scan, savings in scan time are significant. Though, the disadvantages of this technique, enhanced blurring and decreased SNR, have not been addressed so far and scout scans have not proven robust.

Another recent publication claiming twofold acceleration employs hexagonal undersampling in y-z-direction [112]. Instead of full k-space sampling, a hexagonal pattern is acquired, causing diagonally positioned image replicas. Due to the spatial boundedness of the distorted slice, signal aliases in the boundary area of the y-z-plane and tends not to interfere with the unaliased signal. Subsequently, aliased signal can be zeroed.

A similar procedure, named *Off-Resonance Encoding* (ORE), was developed by Smith et al.

[109]. It can be combined with any MSI technique, but its application to MAVRIC is most plausible: Each bin does not only reflect a defined spectral range, but also a unique spatial distribution of the signal (cf. figure 3.7b). These singular spatial sensitivities provide redundancy to full k-space sampling analogous to parallel imaging. Different spatial sensitivities allow different undersampling schemes according to the amount of signal and the sign of the bin's off-resonance. Although the technique is implemented similarly to GRAPPA, ORE and parallel imaging are independent of each other. Images of good quality with an ORE acceleration factor of 2.1 were presented for a total knee replacement [109].

Further developments of SEMAC mainly focused on the optimal combination of the single partitions contributing to one slice. The initial approach aimed for non-overlapping partitions, which were combined as a linear complex sum [80]. This type of combination yields a flat spectral response, but results in low SNR. The high level of noise excludes STIR or parallel imaging techniques for high resolution SEMAC images [54]. In contrast, sum-of-squares combinations produce high SNR, but penalize partitions with low signal amplitudes and thus lead to inconsistent signal intensity. A technique to reduce the noise from the first reconstruction method has been investigated [79]. Though, its SNR is still inferior compared to the sum-of-squares technique. One distinct artifact in SEMAC imaging has been investigated only recently. Ripple artifacts occur due to discontinuities between slices and thus partitions, which are combined to one SEMAC slice. Den Harder et al. [44] analyzed the sources of these ripples in detail and demonstrated that B_0 must vary both in- and through-plane to induce this type of artifact. Since areas of strong off-resonances usually feature strong gradients, ripples occur particularly in close proximity to complex metal structures. Overlapping slice profiles attenuate ripples substantially. Though, thicker slices generated with the help of lower gradient amplitudes G_{SS} result in increased through-plane distortion. Using higher RF pulse bandwidths to cover the larger slice width imposes higher SAR on the subject. In either case, overlapping slices involve an increase of scan time.

Another residual in-plane artifact neither addressed by MSI techniques nor by any other methods is induced during frequency encoding: The impact of extreme local gradients of the static magnetic field on the readout process has been analyzed recently [60]. In areas, where the amplitude of the static local gradient equals the readout gradient amplitude, but is of opposite polarity, frequency encoding fails and signal pile-ups can be identified. A further increase of the magnitude of the static local gradient leads to signal loss. Signal loss can be detected as well in regions, where both gradients are of same polarity and approximately equal amplitude. This type of artifact appears as ripples with variations of hyper- and hypointense signal in readout direction. For MAVRIC imaging, Koch et al. have shown that signal pile-ups can be addressed by Jacobian multiplier methods in a limited way, while signal loss cannot be restored [58]. Thus, frequency encoding in presence of strong static local gradients limits the efficiency of MSI techniques. The only way to avoid this type of artifact is the use of SPI methods.

Blurring in MAVRIC images due to missing correction of in-plane distortion has been addressed by advanced post-processing algorithms. Off-resonance data obtained from the MAVRIC acquisition process can be used to allocate the distorted signal in-plane to its original position [54]. A Jacobian-based approach does not consider the spatial distribution of B_0 only, but also its first derivative, reducing blurring additionally [58].

Artifacts due to the modulation of B_1 in orthopedic MRI have been recognized and their sources have been investigated [16, 34, 59]. It is important to note that both sources for currents (RF pulses and gradient switching) are also present in single-point imaging. Thus, even new techniques promising minimum susceptibility-induced artifacts are affected by B_1-related artifacts. Yet, no techniques to alleviate these types of artifacts have been investigated and suggested up to now.

Shift towards 3 T

Since the establishment of commercial 3 T scanners on the market in the very beginning of the 21st century, their benefits and challenges with respect to image quality and range of applications have been investigated. First studies on metal implants at 3 T in 2005 compared artifacts for aneurysm clips at 3 T to 1.5 T originating from differences in susceptibility [92] and RF induced currents [68]. In addition, an increasing impact of RF artifacts in the presence of orthopedic metal hardware was noted at 3 T [34]. A first numerical and rough analytical explanation of this effect followed in 2010 [59]. Later investigations analyzed potential heating in the presence of a metallic plate and screws [76] and bilateral hip replacements [97]. Neither publication identified increased local SAR or local heating at 3 T compared to 1.5 T. The extent of susceptibility artifacts close to metal implants at 3 T has been compared to 1.5 T in a cadaver study [31] and protocol parameters including the readout bandwidth and the turbo factor have been optimized for a TSE sequence. The authors did not consider through-plane artifact correction. Only a recent in-vitro comparison included the field strength and the imaging sequence (TSE versus MAVRIC-SL) as parameters [74]. In 2007, MRI was disadvised in the presence of metal at 3 T [69] due to a lack of techniques to counter the enhanced level of artifacts. The use of scanners with low field strength was suggested instead. Authors focusing solely on 3 T imaging illustrated possibilities for scan time reduction in SEMAC imaging with help of compressed sensing in spinal imaging [118] and quantified the level of artifact reduction in MSI techniques compared to standard TSE imaging for numerous dental implants [121]. Lately, the clinical benefit of MAVRIC-SL over TSE sequences was investigated at 3 T focusing on hip replacements [21, 63] and general orthopedic metal devices [39]. All authors emphasize the significantly reduced volume affected by signal voids and pile-ups due to the presence of metal in MAVRIC-SL images compared to TSE images. MAVRIC-SL simplifies the assessment of the need for a surgery or the type of surgery. Though, the general image quality of MAVRIC-SL is deteriorated compared to TSE with respect to spatial resolution, SNR, contrast and fat saturation.

Potential Improvements at 3 T

Artifacts in the presence of metal, which are intensified at 3 T, are challenging and no technique dedicated for 3 T has been developed up to now. The enhanced level of susceptibility-induced through-plane distortion is addressed by a high spectral coverage, further prolonging MSI techniques at 3 T compared to 1.5 T. This is problematic in terms of limited patient comfort, increased likeliness of motion artifacts and finally economic considerations.

However, dedicated transmit coils for orthopedic applications exist, as stated in section 2.3. These coils differ from the body coil not only by size and shape, but offer specifications, which are expedient in metal implant imaging. For example, local transmit coils dedicated for knee imaging have an outstanding increased peak B_1 amplitude compared to the whole-body transmit coil. In addition, the coil's local use in extremities only implicates a partial exposure of the body and less strict local SAR limits (10 W/kg in extremities compared to 20 W/kg in the body trunk). These characteristics are highly beneficial in implant imaging, since high B_1 amplitudes allow broad RF pulse bandwidths, which cannot be generated by the body coil due to limitations in RF power and SAR. In addition, a precise and dense arrangement of multiple receive coil elements enables high acceleration factors in parallel imaging. These coils are widely-used in orthopedic MRI and are available on most current scanner platforms. Considering the high number of TKA and adding the amount of other metal fixtures in the knee like plate osteosyntheses, the benefit of such application is highly attractive. One objective of this work is to investigate the effects of high-bandwidth RF pulses in respect of through-plane distortion, image quality and the reduction of scan time for SEMAC and TSE in the presence of metal.

In contrast to susceptibility-induced distortion, artifacts based on the modulation of the RF field have not been addressed by any technique involving the control of the MR scanner. As currents generating RF artifacts are mainly based on transmit field characteristics, their amelioration demands the modification of the B_1 field. Several commercial 3 T scanners are equipped with hardware enabling parallel transmission with two independent channels. This opens new possibilities to tackle RF artifacts. As published earlier, RF artifacts become prominent especially for elongated metal structures in parallel to the static magnetic field. Thus, MR images of the shafts of hip replacements and proximal femur nails, for example, are affected. As these implant types are not weight-bearing, they are commonly made of titanium. The related susceptibility-induced artifacts are moderate. Consequently, shading and brightening due to RF effects is emphasized, even if through-plane distortion correction fails or is not addressed at all. This work deduces a model to describe the RF effects in the presence of a metal rod analytically. Not only the geometry of the setup, but also the polarization of the transmit field is considered to determine the spatial distribution of B_1. Also the clinical impact of the transmit polarization and its optimal selection are analyzed.

4 High-Bandwidth RF Pulses

The purpose of this chapter is to investigate the impact of high-bandwidth RF pulses on image quality in the presence of metal implants. These specific RF pulses can be applied by local transmit coils only and assist to reduce susceptibility-induced distortion perpendicular to the imaging plane. Two scopes of application are presented: knee implant imaging and MRI of the postoperative spine.

4.1 Materials and Methods

In the beginning, a theoretical analysis of the impact of the RF pulse bandwidth on susceptibility-induced distortion is presented. It illustrates the challenges with respect to hardware requirements and SAR limitations. Phantom experiments demonstrate the influence of high-bandwidth RF pulses for a total knee arthroplasty at 3 T. A clinical study with eight subjects with similar pathologies illustrates the relevance of this RF pulse type in routine imaging. To conclude, this RF pulse type is also used for spine imaging in a prototype setup.

4.1.1 Theory: Effects of High-Bandwidth RF Pulses

General physical principles of magnetic resonance imaging in the presence of metal are described in chapter 3, as well as techniques to reduce them. One potential approach to limit susceptibility-induced artifacts is the use of high-bandwidth RF pulses, which has not been investigated up to now. To start with, the impact of the RF bandwidth on the distortion is analyzed, as well as its influence on imaging techniques, which correct this type of artifact.

The spatial distortion both in- and through-plane is influenced by the bandwidth f_{BW} of the RF pulse. Assuming an off-resonance of Δf and neglecting slice profile information, the spin is excited by a slice-selective excitation pulse, if it satisfies the equation

$$\frac{\Delta f}{f_{\mathrm{BW}}} = -\frac{\Delta z}{z_{\mathrm{th}}} \,. \tag{4.1}$$

z_{th} denotes the intended slice thickness and Δz represents the distance of the spin to the position of desired slice on the z-axis, that means Δz is a measure for the through-plane distortion. Hence, spins located at the position of the desired slice ($\Delta z = 0$) are excited in case of resonance, i.e. $\Delta f = 0$. As stated earlier, the correction of through-plane distortion

is time-consuming and particularly challenging at 3 T. Using the SEMAC technique for correction, all through-plane distortion must be covered by SEMAC encoding in the third dimension to avoid image degradation due to aliasing. As the number of SEMAC-encoding steps relates linearly to the through-plane distortion (Δz), it is beneficial to reduce this parameter. It can be decreased by the use of high-bandwidth RF pulses and by the selection of thinner slices. The use of thinner slices can be linked with an increase in scan time: More slices are required to cover the anatomy and TSE-based sequences are often restricted by SAR. Hence, the temporal density of RF pulses cannot be increased and acquisition time must be prolonged. One option to keep the number of slices constant is to increase the distance between slices. This is possible in TSE imaging and can be combined with VAT. However, advanced methods like SEMAC require slices located adjacent to each other and scan time may be prolonged. In addition, a reduced slice thickness results in decreased SNR. The downside of high-bandwidth RF pulses is an increased in-plane distortion: Spins featuring higher off-resonances are excited. During the readout process, the signal is mapped to a wrong in-plane position independently of the through-plane distortion (cf. equation (3.7)). VAT and high readout gradients are techniques to limit this type of distortion at the cost of SNR and image sharpness.

The bandwidth of RF pulses cannot be changed deliberately: The peak B_1, determined by the specifications of the scanner, and SAR regulations limit this parameter. The bandwidth of amplitude-modulated RF pulses, which are used in this chapter, is reciprocal to their duration τ, i.e. $f_{\mathrm{BW}} \propto \tau^{-1}$. TSE imaging requires specific flip angles, but the peak B_1 is limited. Thus, a minimum τ is linked to each type of RF pulse and flip angle, which in turn determines the maximum RF pulse bandwidth. In addition, the energy deposition correlates with the bandwidth of each single RF pulse (cf. equation (2.6)). If the flip angle of the RF pulse is kept constant, SAR scales linearly with its bandwidth. The number of required SEMAC steps $n_{\mathrm{S,r}}$ to avoid aliasing can be expressed as a function of the excitation bandwidth:

$$n_{\mathrm{S,r}} = \frac{\max(\Delta f) - \min(\Delta f)}{f_{\mathrm{BW}}} \ . \tag{4.2}$$

This illustrates the benefit of high-bandwidth RF pulses in scan time, which scales linearly with $n_{\mathrm{S,r}}$, and motivates their use.

To sum up, high-bandwidth RF pulses cause an increased in-plane distortion, which can be limited by the use of high readout gradients and VAT. However, restrictions related to the peak B_1 and the SAR appear insuperable. One possibility to bypass these limitations is the use of local transmit coils. Details are covered in the following section about hardware.

4.1.2 Hardware

Clinical standard protocols in metal implant imaging employ RF pulses with increased bandwidths, which require slightly less than the peak B_1 of the body coil. A significant gain in bandwidth can be accomplished only by the use of a transmit coil with increased peak B_1. Hence, the transmission of such RF pulses requires other hardware than the common whole-body birdcage coil and thus is limited to applications covered by the range of local transmit coils. Local transmit coils dedicated for knee imaging are widely-used in

orthopedic imaging centers and commercially available on most current scanner platforms. These coils are birdcage coils, just as whole-body transmit coils are, but their diameter and longitudinal extent are smaller. Besides the enhanced B_1 amplitude due to the smaller diameter of the volume coil, multiple receive coil elements surrounding the knee allow high acceleration factors for parallel imaging techniques. With respect to SAR, this coil offers an additional advantage: Due to its geometry as a dedicated knee coil, imaging can be limited to particular extremities. In contrast to whole-body transmit coils, energy can be irradiated on extremities only and the body trunk is not affected. Hence, less restrictive SAR limits apply (cf. section 2.2.2).

Phantom experiments to analyze the effect of high-bandwidth RF pulses and the patient study used the following setup: The local knee coil (Quality Electrodynamics (QED), Mayfield Village, OH, USA) with one channel for transmission and 15 receive channels (figure 4.1a) was used for all experiments in combination with a 3 T whole-body MR scanner (MAGNETOM Skyra^{fit}, Siemens Healthcare, Erlangen, Germany). The peak B_1 of the local transmit coil is approximately three times the amplitude of the whole-body birdcage coil of the scanner. Two patients participating in the study had reference scans on a 1.5 T-scanner to compare image quality. For these experiments, a MAGNETOM Espree (Siemens Healthcare, Erlangen, Germany) with a whole-body transmit coil was used in combination with an 8-channel receive-only knee coil (InVivo, Gainesville, FL, USA).

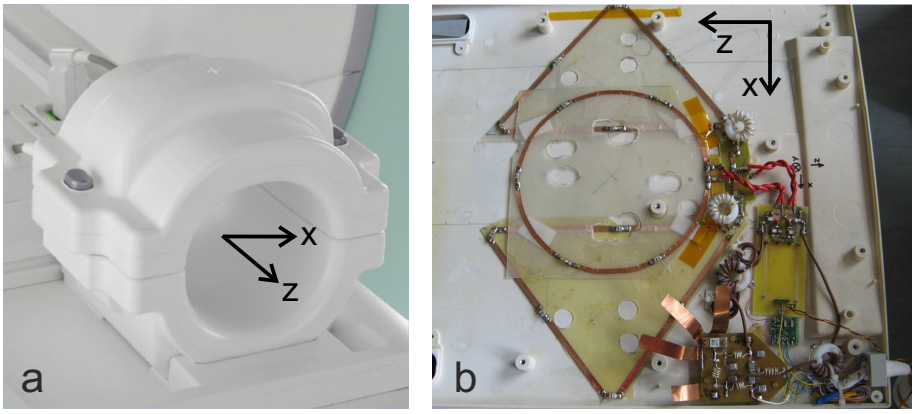

Figure 4.1: (a) Transmit/receive knee coil; (b) hardware setup of the transmit/receive spine coil.

In a third experiment, not the local transmit knee coil was used for the application of high-bandwidth RF pulses, but a prototype of a local transmit spine coil [105]. Unlike the transmit/receive knee coil, this coil is not designed as a volume coil, but as a planar structure with three loop antennas. One circular loop with a diameter of 20 cm in the center of the setup accounts for a strong B_1 with adequate penetration depth perpendicular to the loop. Two triangular loops parenthesizing the circle on the left and right side (figure 4.1b) generate a B_1 component orthogonal to the one excited by the circular loop, mainly supported by the bases of the triangles, which are in parallel with the z-axis of the scanner. The transmit antennas are also used during the receive process, i.e. the coil is a 1-channel transmit and 2-channel receive coil. A MAGNETOM Skyra (Siemens Healthcare, Erlangen, Germany) served as 3 T whole-body scanner.

4.1.3 RF Pulses in Knee Implant Imaging

The aim is to illustrate the effects of high-bandwidth RF pulses compared to conventional RF pulses. To gain the maximum benefit in reduction of through-plane distortion, the maximum B_1 according to the specifications of the local transmit knee coil was exploited. In the phantom experiment, a SEMAC sequence was utilized, while in the patient study, the sufficiency of both TSE and SEMAC with a defined number of SEMAC-encoding steps was analyzed for different implant types for a reduced through-plane distortion. Since TSE-based sequences, which are robust towards off-resonances due to strong differences in susceptibility, employ slice-selective RF pulses only, the RF bandwidth is limited by the largest desired flip angle, i.e. by refocusing pulses. The refocusing flip angle α_r is larger than the flip angle α_e used for excitation and the respective pulse durations behave similarly. According to equation (2.6), f_{BW} is limited by the longest RF pulse duration provided that equal RF pulses are used for excitation and refocusing. As reference, RF pulse types of the standard product TSE were selected and their maximum bandwidth was determined by the minimum possible duration of the refocusing pulses τ_r to induce a flip angle of 180 ° for any object to be imaged, when the body coil is used for transmission. The duration of the excitation pulse τ_e was modified such that its bandwidth matches the bandwidth of the refocusing pulse train. The resulting specifications of the reference sequence are the following: An SLR pulse with a time-bandwidth product of 2.2 and a bandwidth of 850 Hz is used for excitation, while windowed SINC-pulses (TBP = 2) serve for refocusing. Their bandwidth matches the excitation bandwidth in SEMAC sequences, while it is reduced to 758 Hz in TSE imaging for ORS. The entity of these RF pulses is referred to as conventional mode in the following; the conventional mode can be applied by both the body coil and the local transmit coils, i.e. the knee and the spine coil, which are used in the following experiments. RF pulses, which exploit the increased peak B_1 of the local knee coil, are SINC-shaped with a TBP of 4. This pulse type is used, because its TBP can be modified easily; in comparison to the numerically optimized SLR pulses, no adverse effects due to a potentially lower accuracy of the slice profile were detected. Excitation pulses in both TSE and SEMAC sequences and SEMAC refocusing pulses have a bandwidth of 4 kHz and for ORS, the bandwidth of the refocusing pulses in TSE sequences is 3.3 kHz. This RF mode is summarized as high-bandwidth (HiBW) mode.

In this work, SEMAC is always used in combination with VAT and the thickness of the SEMAC partitions matches the nominal thickness of the slices to be imaged. The reconstruction algorithm to combine single SEMAC partitions uses the sum-of-squares technique. Protocols for fat suppression used in the clinical study are based on the STIR technique to encounter the strong off-resonances of the static magnetic field. For either RF mode, the bandwidth of the selective adiabatic inversion pulse matches the bandwidth of the excitation RF pulse [114]. In HiBW mode, the range of off-resonances, which is covered by each slice and hence SEMAC partition, is 4.7 times as high as in conventional mode. Therefore, the number of required SEMAC-encoding steps to cover the same range of off-resonances in conventional mode is expected to be 4.7 times as high as in HiBW mode. A similar relation can be expected for the required scan time. To focus on the RF bandwidth as unique difference in the comparison of the HiBW with the conventional mode, both RF modes are transmitted and received by the knee coil, although the whole-body birdcage coil is capable to apply the conventional mode.

4.1.4 Phantom Experiments with a Total Knee Arthroplasty

Experimental correlations of the reduction of through-plane distortion and the RF pulse bandwidth were investigated on a cylindrical phantom containing a total knee arthroplasty (BPK-S, Peter Brehm, Weisendorf, Germany). The tibial and femoral parts made of $CoCr_{28}Mo_6$ were spaced by an insert made of polyethylene and immersed in agar doped with 1.25 $NiSO_4 \times 6\,H_2O$ and 5 g NaCl per liter. Grids made of polypropylene were placed on two sides of the TKA (figure 4.2). This phantom was inserted in the transmit knee coil with the long axis of the cylinder aligned in z-direction and scanned with the 3 T-setup and a readout bandwidth of 685 Hz/Pix. To evaluate the intensity of the induced off-resonances

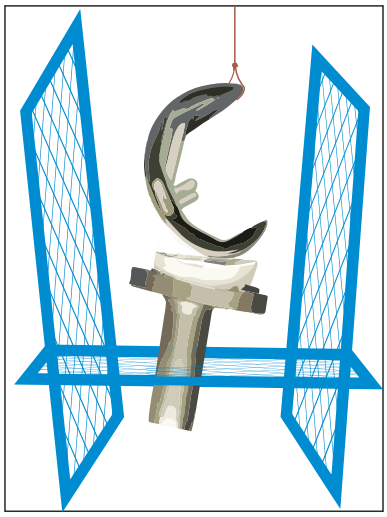

Figure 4.2: Schematic of the phantom setup with total knee replacement made of $CoCr_{28}Mo_6$ with a polyethylene insert, polypropylene structures on both sides (marked in blue) and a string for fixation during production.

of the static field, a B_0 map was obtained on the basis of a SEMAC acquisition, which covered ±60 kHz in steps of 2 kHz, which corresponds to the bandwidth of the RF pulses used for excitation. 60 slices and 60 SEMAC-encoding steps were acquired with a slice thickness of 1.5 mm and an in-plane resolution of $0.4 \times 0.4\,mm^2$ for a matrix size of 312×384. The turbo factor was 9, echo time $T_E = 36$ ms and $T_R = 8100$ ms. The algorithm for the generation of the field map on the basis of the acquired SEMAC data was implemented in Matlab (MathWorks, Natick, USA). This software was also used for any subsequent offline analysis of experimental data in this work. To compare the impact of the conventional and the HiBW mode on distortion, SEMAC images of the phantom were acquired in both RF modes. 60 slices with a thickness of 3 mm and an in-plane resolution of $0.4 \times 0.4\,mm^2$ for a matrix size of 300×384 were obtained in an acquisition time of 2:05 h for a parallel imaging acceleration factor of 3 (GRAPPA) and a turbo factor of 9, echo time $T_E = 28$ ms and repetition time $T_R = 9600$ ms. For both the number of slices and n_S, a quantity of 60 was selected to obtain maximum off-resonance coverage for the central slice; this number was restricted to 60 by the memory size of the scanner's reconstruction computer. To quantify the spatial through-plane distortion of the central slice, the maximum signal intensity of all SEMAC partitions contributing to the final reconstructed central slice is visualized as a function of neighboring slices. The respective graphs for both RF modes are compared.

The maximum signal intensity of each partition is selected for visualization, as this is of particular importance for the reconstructed SEMAC image: If a partition with high local signal intensity is not covered in the SEMAC-encoding process, aliasing induces signal pile-ups of high intensity in the final image, as well as signal voids, which can be overlapped by aliased signal. The degree of artifacts is determined by the signal intensity in the specific area of the original partition and can be evaluated well due to the signal homogeneity of the phantom. The graph summarizing the spatial distortion in conventional mode is expected to be stretched over more neighboring slices than the one in HiBW mode to express the ratio of the RF bandwidths. The generous data of 60 SEMAC-encoding steps provides the option to simulate SEMAC acquisitions with less than 60 SEMAC-encoding steps on the assumption that all off-resonances are covered by this data. Single partitions can be combined appropriately, such that the result of an arbitrary SEMAC acquisition can be reconstructed. This technique was used for the illustration of the level of artifacts dependent on the applied number of SEMAC-encoding steps and it is referred to as virtual reconstruction in the following. The number of SEMAC-encoding steps required to cover all off-resonances occurring in the central slice, $n_{S,r}$, was determined on the basis of the field map for the HiBW mode. A virtual reconstruction with this number of SEMAC-encoding steps was conducted for both the conventional and the HiBW data and the resulting images of the central slice were compared. A second value for n_S for a virtual reconstruction was determined with respect to a patient study, where scan time is limited due to the clinical environment and patient motion. The requirement to obtain all relevant clinical contrasts in a maximum scan time of 9 minutes at 3 T allows a maximum of $n_S = 8$. The data of both RF modes was reconstructed virtually for this amount of SEMAC-encoding steps.

4.1.5 Postoperative Knee Imaging In Vivo

All patients participating in this study signed informed consent and the study was approved by the institutional review board. The purpose of the study was to investigate the effects of TSE and SEMAC sequences equipped with high-bandwidth RF pulses in vivo. In total, eight patients with metal implants in their knees of various types and materials participated: In five cases, the total knee had been replaced by an arthroplasty, two patients had metal plate osteosyntheses and one an intramedullary rod in the tibia. For comparison of the HiBW mode with the conventional mode, three critical contrasts in different orientations (PD: sagittal, T_1: coronal, STIR: coronal) were selected and each contrast was acquired in both RF modes. The employed RF pulses are the only difference between both acquisition modes; all other parameters remained unchanged. Due to the long acquisition times for SEMAC sequences, not all patients could be scanned with both TSE and SEMAC sequences in all three contrasts. SEMAC was the preferred method for patients with TKA, since stronger distortions can be anticipated compared to fixtures of titanium. Table 4.1 summarizes the conducted scans for each patient and lists the contrasts, employed sequences, as well as the implant type of each patient. All listed contrasts were acquired in both RF modes.

In general, 25 slices were acquired of each knee with a slice thickness of 3 mm at 3 T. For T_1-weighted and PD-weighted contrasts, the in-plane resolution was $0.4 \times 0.4\,\mathrm{mm}^2$, while the STIR protocols were setup in lower resolution to increase SNR ($0.6 \times 0.6\,\mathrm{mm}^2$ in-plane). To keep scan time within a range, which is acceptable for a clinical setting, SEMAC protocols

Patient	Implant Type	3 T			1.5 T
		PD sag	STIR cor	T_1 cor	PD sag
# 1	TKA, CoCr	S	S	S	-
# 2	TKA, CoCr	S	S	S	-
# 3	TKA, CoCr	S	S	S	-
# 4	TKA, CoCr	S, T	-	S, T	S, T
# 5	TKA	-	T	S, T	-
# 6	Tibia intramedullary rod, Ti6AL4V	S, T	T	T	S, T
# 7	Plate osteosynthesis with screws, Ti	T	S, T	T	-
# 8	Plate osteosynthesis, Ti	T	T	S, T	-

Table 4.1: Patient study: implant types, contrasts, orientations and applied methods (S = SEMAC, T = TSE); each 3 T-acquisition was performed in conventional and HiBW mode.

with $n_S = 8$ were used. Detailed sequence parameters are given in table 4.2. Due to different RF pulses in HiBW and conventional mode, sequence timing can slightly differ and the echo time may deviate up to 3 ms from the values given in the table.

		T_E/T_R	TF	α_r	matrix	resolution	PAT	T_A
PD sag	TSE	37/4500	9	140	346×384	$0.4 \times 0.4 \times 3.0$	off	3:02
	SEMAC	36/4500	9	135	270×384	$0.4 \times 0.4 \times 3.0$	3	7:18
STIR cor	TSE	40/7200	9	140	256×256	$0.6 \times 0.6 \times 3.0$	off	3:38
	SEMAC	40/7500	10	140	205×256	$0.6 \times 0.6 \times 3.0$	3	9:09
T_1 cor	TSE	16/774	2	140	288×384	$0.4 \times 0.4 \times 3.0$	2	2:04
	SEMAC	16/800	3	130	288×384	$0.4 \times 0.4 \times 3.0$	3	8:10
PD sag 1.5 T	TSE	23/4500	9	145	269×384	$0.5 \times 0.5 \times 4.0$	off	2:21
	SEMAC	36/4500	9	145	269×384	$0.5 \times 0.5 \times 4.0$	3	7:17

Table 4.2: Imaging parameters for each contrast and acquisition mode: T_E and T_R are given in [ms], the total acquisition time T_A in [min] and the flip angle of the refocusing pulses α_r in [°]; the resolution corresponds to the reconstructed voxel size in [mm^3]; PAT represents the GRAPPA acceleration factor in-plane and TF the turbo factor. If not stated differently, parameters reflect the setting at 3 T.

To compare the level of artifacts and the general image quality obtained in HiBW mode to the gold standard at 1.5 T, two patients had additional TSE and SEMAC scans on a 1.5 T-scanner. One RF mode typical for metal implant imaging at 1.5 T was applied by the body coil. The sequence parameters of the 3 T-setup were adopted apart from the voxel size ($0.5 \times 0.5 \times 4\,mm^3$), RF pulse bandwidth (2.7 kHz) and readout bandwidth (566 Hz/Pix instead of 685 Hz/Pix at 3 T). Besides the lower field strength of 1.5 T and thus a generally reduced total SAR deposition, different hardware specifications of the MR scanner including the whole-body birdcage coil enable the transmission of RF pulses of increased bandwidth at 1.5 T compared to the conventional mode at 3 T. The impact of the RF pulse bandwidth on image quality cannot be quantified analytically like in the phantom experiment, since scan times of more than two hours are not feasible for patients. Hence, two radiologists rated distortion qualitatively and independently on a five-point scale: 1 = no artifacts; 2 =

hardly visible artifacts; 3 = clearly visible artifacts, but without impairment of diagnostic quality; 4 = substantial artifacts with moderate impairment of diagnostic quality; 5 = severe artifacts and non-diagnostic image [111].

4.1.6 Spine Imaging with a Local Tx/Rx Coil

Spinal fusions rank among the ten mostly conducted surgeries in the USA [27]. The potential of a prototype local transmit/receive spine coil for postoperative spine imaging was investigated. The hardware specifications of the setup are given in section 4.1.2. Significantly different transmit-B_1 characteristics compared to volume transmit coils result in declining B_1 with increasing distance from the surface of the planar coil. This requires the acquisition of a B_1 map to calibrate the induced flip angle in the region of interest and a preliminary assessment of the feasible peak B_1 in a depth of 3 cm results in a maximum B_1 slightly less than the local Tx/Rx knee coil can achieve. For exploitation of the peak B_1, the same RF pulse types as in the HiBW mode of the knee coil were used, i.e. SINC pulses with a TBP of 4, but the duration was prolonged such that a bandwidth of 3.3 kHz was obtained. This experiment employs TSE sequences only to investigate through-plane distortion. For this purpose, ORS is obstructive such that the high RF pulse bandwidth of 3.3 kHz was used both for excitation and refocusing. The conventional mode of the knee coil was adopted for spine coil imaging except that ORS was eliminated by shortening the duration of the refocusing pulses to match the bandwidth of the excitation pulse, which is 850 Hz. Again, the RF mode employing a bandwidth of 3.3 kHz can be applied by the local transmit coil only, while the conventional mode can be generated by the body coil as well.

In a phantom study, the level of distortion was analyzed for both RF modes applied by the local transmit spine coil. For this purpose, a small titanium rod (length 10 cm, radius 5 mm) with three notches of different lengths (0.5 cm, 1 cm and 1.5 cm) and a depth of 5 mm was used. It was placed in a bin filled with doped water and positioned on plastic bricks to ensure a well-defined distance of 2.9 cm between the metal and the planar coil (figure 4.3). To minimize RF-induced shading (cf. chapter 5) and to allow tracking of pure susceptibility-induced distortion, the titanium bar was aligned collinear with the x-axis of the scanner. A flip angle of 90 ° was calibrated iteratively in the area of the titanium by the acquisition of B_1 maps [23] and the adjustment of the reference voltage of the transmit system. For this procedure, the titanium bar was removed from the bin to obtain results

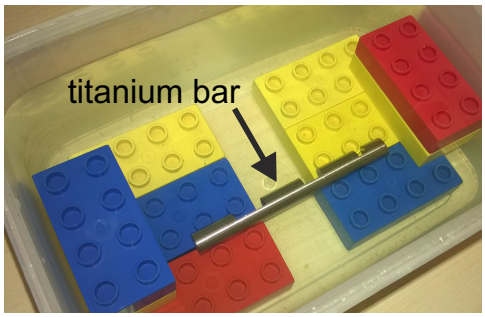

Figure 4.3: Phantom containing a titanium bar with notches placed on plastic bricks.

free from susceptibility- or RF-induced irritations. For the analysis of the impact of the RF pulse mode applied by the local transmit spine coil on distortion, T_2-weighted TSE images ($T_E = 76\,ms, T_R = 2000\,ms$) were acquired with an in-plane resolution of $0.5 \times 0.5\,mm^2$, a slice thickness of 3 mm and a readout bandwidth of 655 Hz/Pix. In addition, images of a volunteer were acquired using the spine transmit coil. High-bandwidth RF pulses ($f_{BW} = 3.3\,kHz$) were used in a TSE sequence and applied by the prototype coil, while this sequence equipped with the respective conventional RF pulses used the body coil for transmission and a commercially available receive spine coil. Eight receive channels were selected. Compared to the phantom experiments, the slice thickness was increased to 4 mm and repetition time was prolonged ($T_R = 4500\,ms$) due to SAR restrictions.

4.2 Results

Phantom results analyzing the impact of the RF pulse bandwidth are followed by the evaluation of the clinical study. The section concludes with the outcomes of the experiments with the prototype spine transmit coil.

4.2.1 Phantom Experiments with a Total Knee Arthroplasty

The field map acquired at 3 T of the central slice of the phantom containing the TKA (figure 4.2) is illustrated in figure 4.4a. While the acquisition process covered off-resonances in the range of ±60 kHz, maximum positive off-resonances of up to +24 kHz occur next to sharp edges and highest negative deviations arise between the medial and lateral condyle (−18 kHz). The graph illustrating the results of the through-plane analysis is shown in figure 4.4b. The signal intensity S_{max} of the brightest voxel in each singular SEMAC partition, which contributes to the final central slice, is plotted both for the conventional and the HiBW mode as a function of neighboring slices. The graphs' maximum values are scaled to one. Considering the broadening of the graphs, the spatial distribution in conventional mode spans a wider range of slices than the HiBW mode. A minor peak is visible in both graphs to the left side of their global maxima (arrows). In conventional mode, the distance of this minor peak to the on-resonant center is quantified by 12 slices, while in HiBW mode, the third neighboring slice excites that signal. This diagram plausibly pictures the correlation of the RF bandwidth and the amount of required SEMAC-encoding steps to cover a specified range of off-resonances.

Figure 4.5 shows images reconstructed from the extensive SEMAC data of the phantom simulating different numbers of SEMAC-encoding steps. The sagittal field map in figure 4.4a refers to the same slice. Figures 4.5a and d show images reconstructed from 60 SEMAC-encoding steps in conventional and HiBW mode. According to the field map, all off-resonances are covered in either case. In HiBW mode, blurring of plastic structures in vertical direction, i.e. the direction of frequency encoding, is more intense than in conventional mode. This is visible at the grip and at the position of the polyethylene insert, marked by the long arrows. In addition, SEMAC-specific ripple artifacts derange image quality in both acquisition modes. In conventional mode, the correspondent signal-pile ups

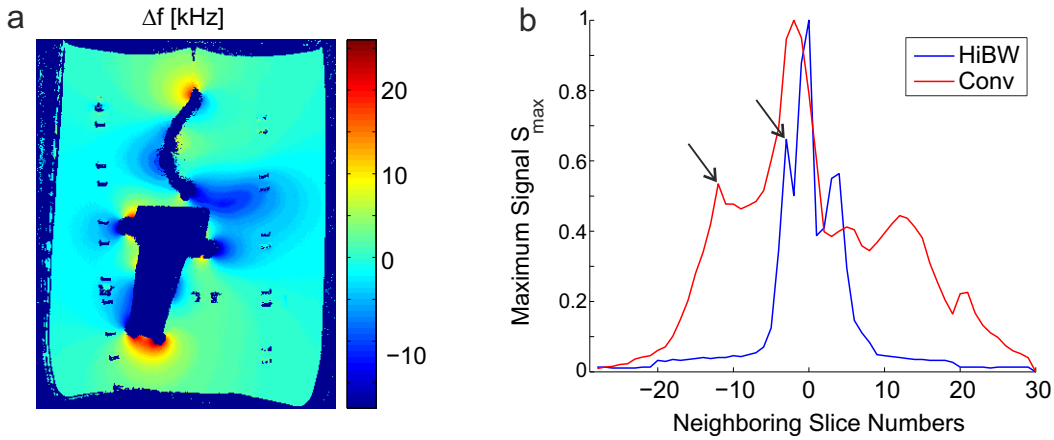

Figure 4.4: (a) Sagittal B_0 map of the central slice of the phantom containing a TKA (cf. figure 4.2); (b) analysis of through-plane distortion of the phantom containing the TKA: highest signal intensity of all voxels in each singularly reconstructed SEMAC partition of different slices contributing to the central slice in high-bandwidth (HiBW) and conventional-bandwidth (Conv) mode.

occur in higher density, but lower intensity than in HiBW mode. The location of the ripple-artifacts is marked by the short arrows. According to off-resonance information gained by the field map, highest efficiency in off-resonance coverage requires asymmetric positioning of the partitions considered for slice recombination with respect to the slice of interest: In conventional mode, 24 SEMAC-encoding steps in negative and 28 in positive direction, i.e. 53 steps in total cover all occurring off-resonances, while 5 in negative and 6 in positive direction, making 12 in total, are required in HiBW mode. The virtual SEMAC reconstruction with $n_S = 12$ from the extensive HiBW data is shown in figure 4.5e and it is comparable to the full reconstruction in 4.5d. No difference becomes apparent. When omitting one SEMAC-encoding step on either the positive or negative end of the phase-encoding process, slightly increased signal voids at either the bottom end of the tibial part or in the posterior center would emerge. Regarding the virtual reconstruction of the conventional data assuming $n_S = 12$ (figure 4.5b), the benefit of high-bandwidth RF pulses becomes obvious. The image is dominated by signal voids and aliasing artifacts. The source of the first artifact is related to strong off-resonances close to metal in the imaged slice, while aliased signal is caused by off-resonances which are covered by slice-selective excitation, but not included in the SEMAC-encoding process. That means, this type of artifact is independent of the field distortion in the imaged slice itself. To anticipate the degree of artifacts for TKA at 3 T occurring for SEMAC acquisitions with 8 SEMAC-encoding steps, figures 4.5c and f show the respective images in conventional and HiBW mode. Compared to the full reconstruction of the HiBW data in 4.5e, the extent of signal voids in regions of maximum and minimum off-resonances is slightly increased in 4.5f, e.g. in the caudal area of the tibial implant. Furthermore, slight signal pile-ups in the area of the tibial and femoral condyle picture aliased signal from areas not covered by the SEMAC-encoding process. While the image virtually reconstructed from conventional data with $n_S = 12$ is dominated by aliasing and signal voids, it is further impaired for a reconstruction based on $n_S = 8$ (figure 4.5c). To sum up, the HiBW image assuming 8 SEMAC-encoding steps illustrates clearly the shape of the metal, as well as the plastic grid. The corresponding conventional image is dominated by artifacts such that neither the profile of the metal, nor the plastic structures

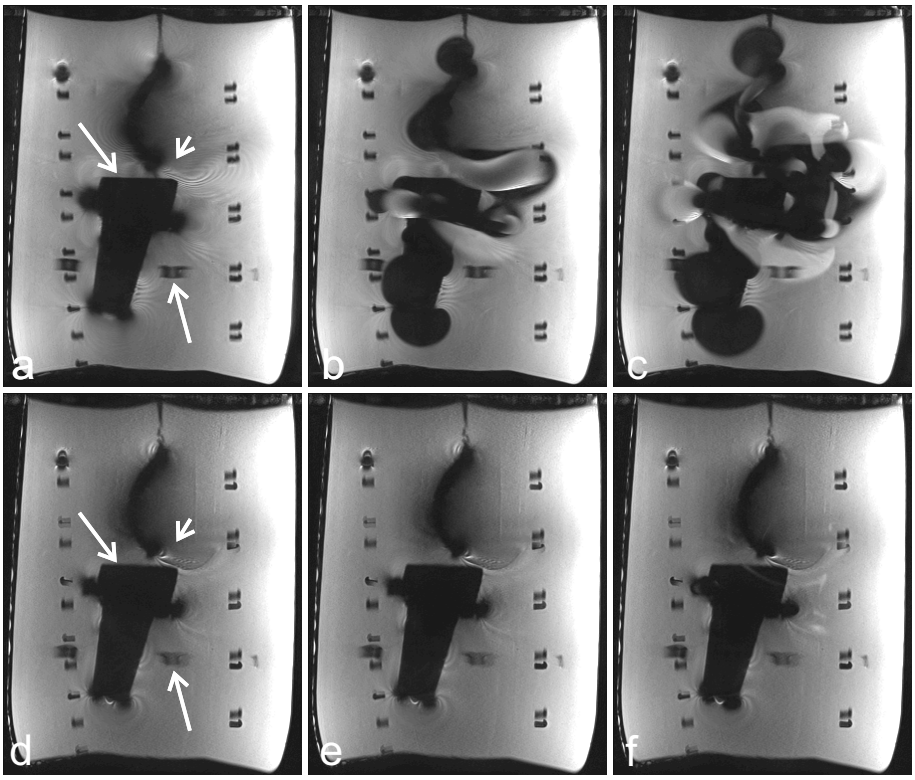

Figure 4.5: SEMAC images of the phantom in conventional (a-c) and HiBW mode (d-e) reconstructed with varying numbers of SEMAC-encoding steps (n_S): (a) and (d) show the images reconstructed from the maximum of $n_S = 60$ (exploits maximum memory size of reconstruction system), which cover ±25 kHz (a) and ±118 kHz (d); long arrows point to areas, where plastic is distorted in readout direction; short arrows point to areas of ripples, which differ for different bandwidths; considering results of figure 4.4a, the virtual reconstruction from a reduced number with $n_S = 12$ in HiBW mode (e) is sufficient to cover all occurring off-resonances; (b) is the corresponding conventional image with $n_S = 12$; virtual reconstructions with $n_S = 8$ in conventional (c) and HiBW mode (f) indicate the level of artifacts to be expected in SEMAC measurements of TKA in vivo.

can be identified at all positions.

4.2.2 Postoperative Knee Imaging In Vivo

Table 4.3 summarizes the qualitative results of the patient study and contains the evaluations of both radiologists. Patients #1, #2 and #3 have TKA of CoCr and the average distortion in SEMAC imaging is rated at a level of 4.3 ± 0.5 in conventional mode, while it is improved to a level of 2.0 ± 0.0 in HiBW mode. The mean distortion in TSE imaging of knees with titanium fixtures (patients #6 to #8) is rated at a grade of 3.1 ± 0.8 for conventional RF excitation and is also improved to a level of 2.0 ± 0.8 in high-bandwidth mode. Please note that the level of distortion in HiBW mode is comparable for TSE and SEMAC imaging for those six patients considered in the numbers above. The group is not only split accoring to the employed imaging sequences, but also according to their implant

Mode/ Patient	PD sag				STIR cor				T_1 cor				PD sag	
	T		S		T		S		T		S		T	S
	C	H	C	H	C	H	C	H	C	H	C	H	1.5 T	
# 1	-	-	4-4	2-2	-	-	5-5	2-2	-	-	4-5	2-2	-	-
# 2	-	-	4-4	2-2	-	-	5-5	2-2	-	-	4-5	2-2	-	-
# 3	-	-	4-4	2-2	-	-	4-5	2-2	-	-	4-3	2-2	-	-
# 4	4-5	3-3	4-4	2-2	-	-	-	-	3-5	2-4	4-4	2-2	3-4	2-2
# 5	-	-	-	-	5-5	3-4	-	-	4-4	3-4	4-4	2-2	-	-
Mean	4.5 ±0.7	3.0 ±0.0	4.0 ±0.0	2.0 ±0.0	5.0 ±0.0	3.5 ±0.7	4.8 ±0.4	2.0 ±0.0	4.0 ±0.8	3.3 ±1.0	4.1 ±0.6	2.0 ±0.0	3.5 ±0.7	2.0 ±0.0
# 6	3-3	1-1	1-1	1-1	3-3	1-1	-	-	2-2	1-1	-	-	2-2	1-1
# 7	2-3	2-2	-	-	4-4	3-3	3-3	3-2	2-3	2-3	-	-	-	-
# 8	3-4	2-3	-	-	4-4	3-2	-	-	3-4	2-3	2-3	2-2	-	-
Mean	3.0 ±0.6	1.8 ±0.8	1.0 ±0.0	1.0 ±0.0	3.7 ±0.5	2.2 ±1.0	3.0 ±0.0	2.5 ±0.7	2.7 ±0.8	2.0 ±0.9	2.5 ±0.7	2.0 ±0.0	2.0 ±0.0	1.0 ±0.0
Mean	3.4 ±0.9	2.1 ±0.8	3.4 ±1.3	1.8 ±0.4	4.0 ±0.8	2.5 ±1.1	4.4 ±0.9	2.1 ±0.4	3.2 ±1.0	2.5 ±1.1	3.8 ±0.8	2.0 ±0.0	2.8 ±1.0	1.5 ±0.6

Table 4.3: Distortion in vivo graded by two radiologists (first-second) on a scale from 1 (no artifacts) to 5 (severe artifacts) for all patients for different acquisition modes: S = SEMAC, T = TSE, H = high-bandwidth mode, C = conventional mode; the mean of all patients and two subgroups (#1-#5 TKA only, #6-#8 titanium inserts only) was calculated for each contrast.

types. SEMAC was the preferred technique for patients with TKA (table 4.1), anticipating stronger deviations of the static magnetic field for this type and material of implant than for titanium fixtures (cf. section 3.2.1). A detailed summary of the radiologists' evaluation of the distortion is given for five patients in the following two paragraphs. Information is allocated according to the implant types.

Patients With Total Knee Arthroplasties

The TKA of patient #4 is made of Protasul-1, which is a CoCrMo alloy. Figure 4.6 pictures the central sagittal PD-weighted images in all acquisition modes, i.e. SEMAC and TSE images in both RF modes at 3 T and the reference scans at 1.5 T. While the TSE image in conventional mode (figure 4.6a) is deranged by signal voids (distortion level 4.5 ± 0.7), the respective SEMAC image (4.6d) suffers from folding artifacts due to insufficient off-resonance coverage. Hence, the application of SEMAC in conventional mode with $n_S = 8$ does not improve the level of distortion distinctly (grade 4.0 ± 0.0). In HiBW mode (figures

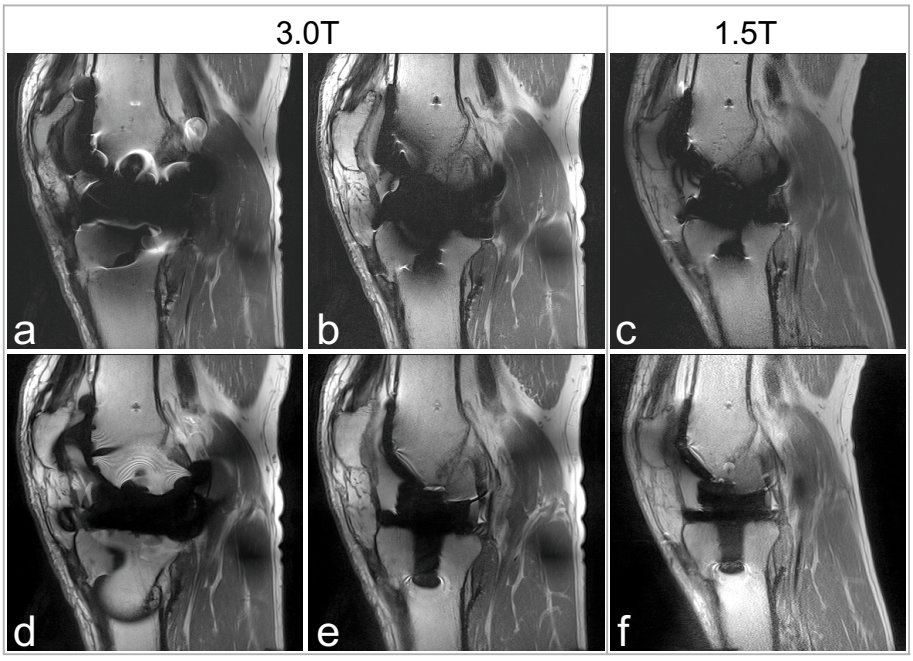

Figure 4.6: Patient #4 with total knee arthroplasty, PD-weighted sagittal: TSE conventional 3 T (a), TSE HiBW 3 T (b), TSE 1.5 T (c), SEMAC conventional 3 T (d), SEMAC HiBW 3 T (e), SEMAC 1.5 T (f).

4.6b,e), distortion is reduced both for TSE (grade 3.0 ± 0.0) and SEMAC (grade 2.0 ± 0.0). In both cases, the level of distortion is comparable to the respective reference scans at 1.5 T (figures 4.6c,f), where the distortion is rated at grade 3.5 ± 0.7 for TSE and at grade 2.0 ± 0.0 for SEMAC. Like in the phantom experiment with $n_S = 8$ (figure 4.5f), the shape of the implant is revealed clearly in the SEMAC acquisition in HiBW mode at 3 T and in the respective image at 1.5 T. Figure 4.7 shows representative slices of patient #5 in STIR and T_1-weighted contrast. In STIR-weighted TSE imaging, the HiBW mode can improve the level of distortion from grade 5.0 ± 0.0 (conventional mode) to grade 3.5 ± 0.7 (figures

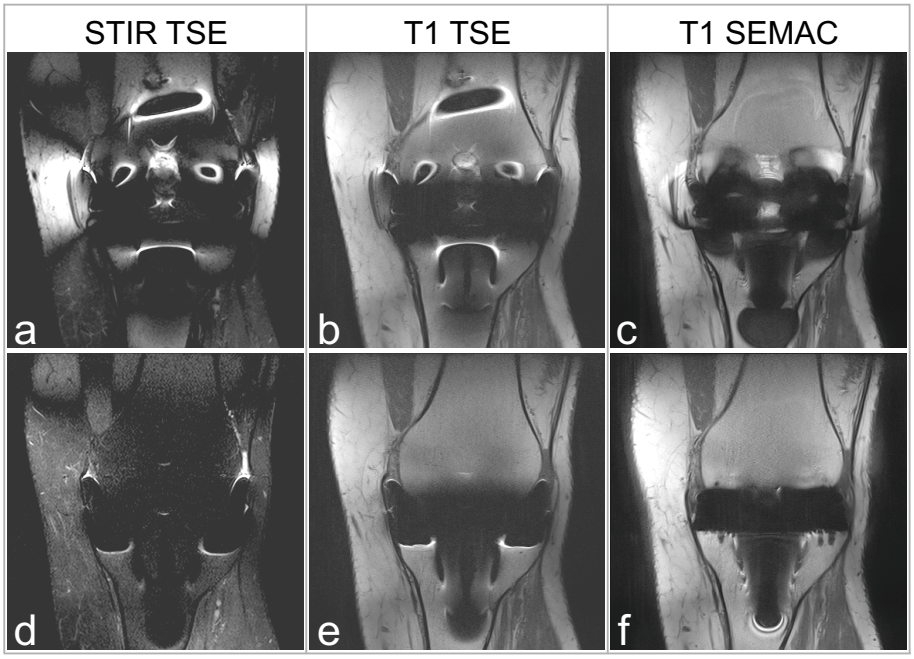

Figure 4.7: Patient #5 with total knee arthroplasty: STIR coronal TSE conventional (a), STIR coronal TSE HiBW (d), T_1-weighted coronal TSE conventional (b), T_1-weighted coronal TSE HiBW (e), T_1-weighted coronal SEMAC conventional (c), T_1-weighted coronal SEMAC HiBW (f).

4.7a,d), while the difference is less significant in T_1-weighted TSE sequences: conventional mode (grade 4.0 ± 0.0) versus HiBW mode (grade 3.5 ± 0.7). Additional improvements of distortion are obtained by the T_1-weighted SEMAC sequence in HiBW mode only, where ripple artifacts in the caudal area of the tibial implant are intensified (figure 4.7f). In the respective conventional mode (4.7c), this type of artifact is replaced by extensive signal void.

Patients With Other Implants

Patient #6 has an intramedullary rod in the tibia, which is made of a titanium alloy. Comparable to patient #4, PD-weighted images of this patient are available both obtained with TSE and SEMAC sequences in both RF modes and at 1.5 T. The results are visualized in figure 4.8. In general, the level of artifacts is relatively low and strongest distortion is induced in TSE conventional mode, where distortion was rated as clearly visible, but without impairment of diagnostic quality. In TSE HiBW mode and any SEMAC acquisition, distortion is minimum at 3 T. Taking the total scan time into account as well, the TSE sequence in HiBW mode at 3 T offers the best option regarding image quality and effectivity. Figures 4.9a-d illustrate the coronal STIR contrast of patient #7 obtained by TSE and SEMAC sequences in both RF modes. The distortion induced by a tibial titanium osteosynthesis is most distinct in TSE conventional mode. Compared to that mode, all other acquisition modes reveal slight improvements. Irrespective of the sequence type, considerable shading occurs in HiBW mode in the area, where the two top screws converge. Coronal T_1-weighted

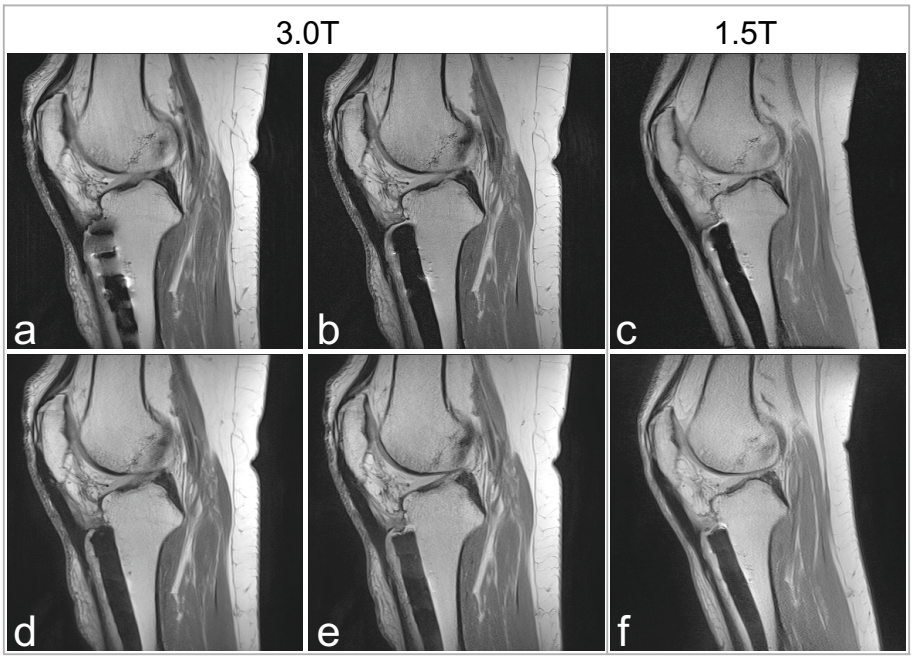

Figure 4.8: Patient #6 with intramedullary rod, PD-weighted sagittal: TSE conventional 3 T (a), TSE HiBW 3 T (b), TSE 1.5 T (c), SEMAC conventional 3 T (d), SEMAC HiBW 3 T (e), SEMAC 1.5 T (f).

images of patient #8 are shown in figures 4.9e-h. The tibial and femoral titanium osteosyntheses comprise titanium screws both approximately perpendicular and parallel to the imaging plane. The femoral ones aligned in parallel to the imaging plane are located in few slice distances to the slice shown. Again, distortion is most pronounced in TSE conventional mode (4.9e) and less intense in all other acquisition modes. While strong signal pile-ups are visible in TSE HiBW mode (4.9f), 8 SEMAC-encoding steps are not sufficient in conventional mode to cover all off-resonances and to suppress folding artifacts (4.9g). Neither signal voids nor wrapping artifacts are visible in SEMAC HiBW mode (4.9h), but ripple artifacts are intensified.

4.2.3 Spine Imaging with a Local Tx/Rx Coil

The flip angle variation after the calibration of the B_1 field distribution targeting 90 ° is illustrated in figure 4.10a. The mean flip angle in the bin in the absence of metal is shown as a function of the distance to the bottom of the bin. The average flip angle in the total bin is 89 °, while in a depth of 2.9 cm, i.e. at the position of the titanium, a mean flip angle of 94 ° is induced. Coronal images of the phantom at the central location of the titanium bar are shown in figures 4.10b and c in conventional and high-bandwidth mode. The red lines in the coronal images cut the metal bar at a position centered between two notches and indicate the position of the corresponding axial reformats (figures 4.10d,e). Comparing the spatial extent in the axial reformats of the V-shaped through-plane distortion including signal voids and pile-ups at the top and bottom end of the "V", the conventional mode expands the bar's diameter from 1.0 cm to 4.0 cm, while the vertical extent of the "V" is

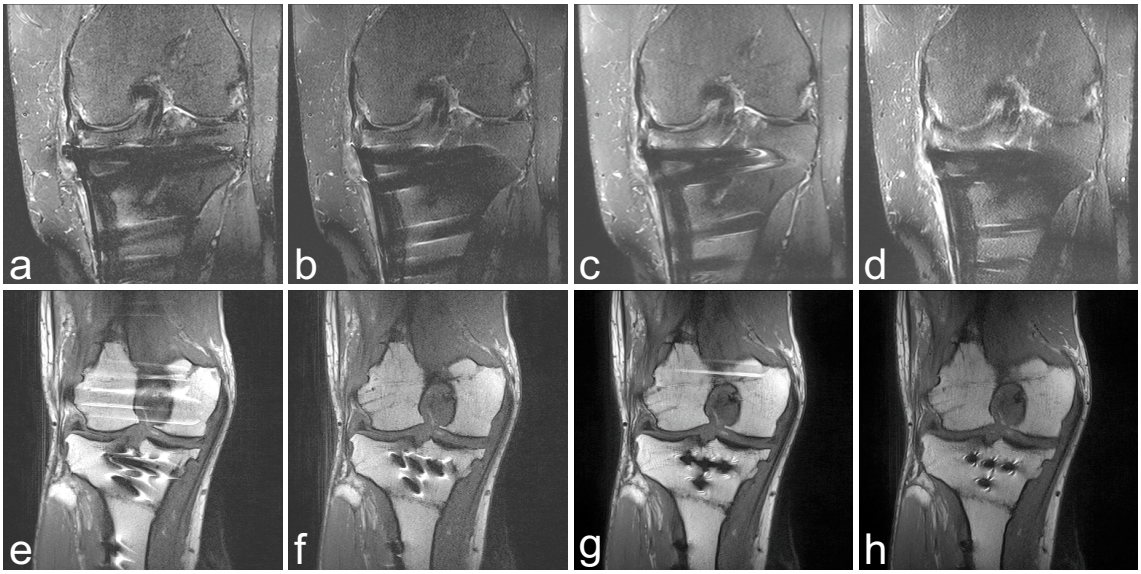

Figure 4.9: Patient #7 with osteosynthesis of the tibia, STIR coronal: TSE conventional (a), TSE HiBW (b), SEMAC conventional (c), SEMAC HiBW (d); Patient #8 with tibial and femoral osteosyntheses, T_1-weighted coronal: TSE conventional (e), TSE HiBW (f), SEMAC conventional (g), SEMAC HiBW (h).

2.6 cm for the high-bandwidth mode. While slight signal pile-ups are visible in the coronal high-bandwidth image, the respective conventional one is impaired by strong signal drop-out. Plastic bricks are neither distorted nor blurred in any RF mode, but noise is slightly enhanced in the high-bandwidth image.

Images of the volunteer (figure 4.11) illustrate the imaging potential of the local transmit/receive spine coil in vivo and allow a comparison with the conventional clinical setup. The receive and excitation field characteristics of the prototype coil result in a distinct modulation of SNR and contrast over the total field of view (figure 4.11b), while the conventional RF mode transmitted by the body coil yields more homogeneous image attributes (4.11a).

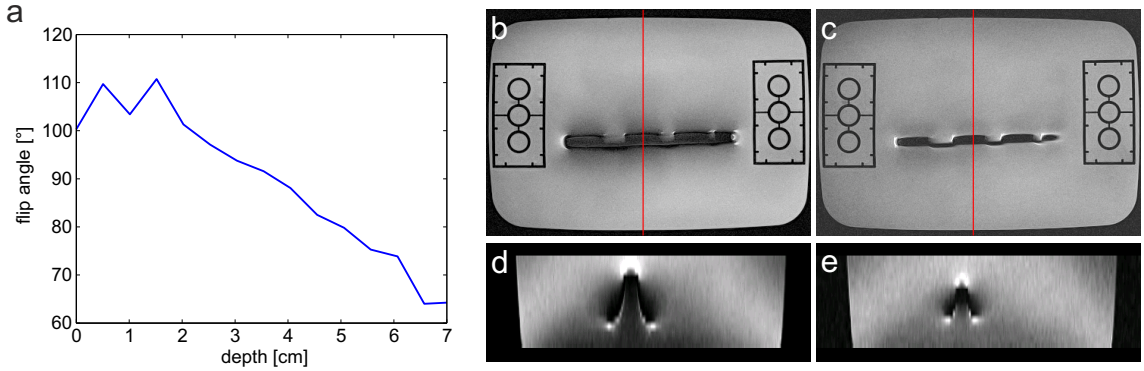

Figure 4.10: (a) Flip angle variation in the phantom along the axis perpendicular to the planar coil; (b-e) results of phantom experiments: coronal TSE images in conventional (b) and high-bandwdith RF mode (c); red lines indicate the positions of the axial reformats (d,e).

Figure 4.11: In-vivo comparison: conventional mode using the transmit body coil and local spine receive coil (a), high-bandwidth mode applied by the transmit/receive spine coil (b).

4.3 Discussion

Through-plane distortion induced by strong differences in susceptibility can be confined by the use of ORS, thin slices and high-bandwidth RF pulses, while advanced methods like MAVRIC and SEMAC can restore distorted signal. Sophisticated methods to resolve through-plane distortion involve a significant increase in scan time, scaling with the level of through-plane distortion. Hence, acquisition time and the associated impairment of patient comfort, economic efficiency and the risk of motion artifacts constitute the downside of these techniques and prevent their application in clinical routine, especially at 3 T. The use of parallel acceleration during the receive process allows to shorten scan time. However, a clinically acceptable scan time cannot be achieved with adequate image quality. ORS cannot only be combined with TSE imaging, but also with SEMAC [42]: The cutoff frequency can be selected such that it equals the spectrum covered by the SEMAC encoding. However, increased signal voids (cf. figure 3.9) are the drawback of this method and the reason for not using this technique in the experiments presented in this chapter. The theoretical analysis in this chapter shows, that thinner slices can contribute to reduced through-plane distortion and hence less required SEMAC-encoding steps as well. Slices with a thickness of 3 mm were selected for imaging protocols in this chapter, which offers a good balance between the reduced spatial distortion perpendicular to the slice and the disadvantage of thin slices, which is mainly the SAR impact: Since SEMAC cannot handle slices which are separated by an arbitrary distance, slices are adjacent to each other with no gap in between. Thus, more slices are required to cover a certain anatomy compared to a setup, where slices can be stretched by a gap in between. Although both TSE and SEMAC are multi-slice techniques, an increased number of slices involves either an extension of the repetition time to include more slices within one T_{R} or a regrouping of encoding steps which results in more repetitions. The reason for this behavior can be found in the general high level of SAR in metal implant imaging at 3 T, which usually does not allow an increase of the temporal density of the RF power.

Experiments with a phantom containing a TKA of CoCr validate the inverse relation of the required SEMAC-encoding steps to the applied RF bandwidth. A specific off-resonance with highly intense signal in the slice considered is excited by the third next slice and the twelfth next slice in HiBW and conventional mode, respectively. This reflects approximately the fraction of the RF bandwidths of HiBW over conventional mode, which equals 4.7. Although through-plane distortion is reduced, high-bandwidth RF pulses degrade in-plane image quality. Since the readout bandwidth remained constant for all RF and acquisition modes, the VAT gradient applied in SEMAC sequences has stronger effects in HiBW mode than in conventional mode: While the view angle is 9.4 ° in conventional mode, it increases to 37.9 ° in HiBW mode and imposes a stronger low-pass filter on the final image [15]. This becomes visible as blurring in readout-direction (vertical one in the phantom study) close to plastic grid and the polyethylene insert, and it is intensified in HiBW mode compared to conventional mode. Methods based on the sparse sampling of k-space edges have been proposed to decrease blurring due to VAT [73, 120], but they have not been tested in combination with SEMAC yet. The comparison of the conventional images of the TKA in the phantom with the respective HiBW images reveals another difference: Ripple artifacts in the HiBW SEMAC images consist of fewer transitions between hypo- and hyperintense signal, but these transitions are more intense than the ripples in the conventional images. The source of this type of artifact lies in a very strong spatial gradient of B_0, which visualizes the spectral properties of the RF pulse and the shape of the slice profile. Recent suggestions for moderate improvement imply a prolongation of scan time [60].

The results of the in-vivo analysis based on the opinion of two radiologists indicate a similar grade of distortion for TSE images in HiBW mode and SEMAC images in conventional mode for patients with titanium fixtures in their knees. It has to be considered that the scan time for the SEMAC acquisition is about four times as high as for the TSE acquisition. Signal voids can be minimized only by the application of SEMAC with sufficient SEMAC-encoding steps to cover the full range of occurring off-resonances. Though, the benefit of additional off-resonance coverage is small, when images of the SEMAC HiBW mode are compared to TSE HiBW images, and it does not justify the long scan time of the SEMAC sequence for titanium plates, nails and screws. Although the SEMAC conventional mode with 8 SEMAC-encoding steps is capable to correct a larger range of off-resonances than the TSE HiBW mode can cover, the final image in SEMAC conventional mode can be degraded by more severe through-plane artifacts: Aliased signal from areas, which are not covered by the SEMAC encoding of a specific slice, appears in the slice of interest. Another advantage of the TSE images in any RF mode is the absence of ripple artifacts. On the basis of the outcome of the three patients with titanium structures, the TSE sequence in HiBW mode offers best image quality for the scan time provided. Locally enhanced shading close to titanium screws indicate impairment of image quality for a specific pathology. This shading is related to the HiBW RF mode and requires further investigation. Possible reasons are eddy currents induced by higher slice-select gradient amplitudes or currents induced by the electric field, which becomes more intense for a stronger transmit B_1 field.

The 3 T-study comprised five patients with TKA of CoCr. In all cases, optimized TSE sequences in any RF mode could not sufficiently reduce artifacts to allow reliable diagnoses. Thus, SEMAC is indispensable. SEMAC equipped with HiBW RF pulses reduces through-plane distortion compared to the conventional mode which in turn demands less SEMAC-encoding steps to correct the spatial distortion. Hence, this technique is highly efficient

in reducing acquisition time and offers clinically accepted scan times at 3 T. This reduces the probability of patient motion and incidental artifacts and leads to increased patient comfort as well as a higher economic efficiency. The presented SEMAC protocols for the patient study last in the range of 7 to 9 minutes and permit 8 SEMAC-encoding steps per slice. Regarding the resulting images, this number of SEMAC-encoding steps offers a good balance between artifact reduction and acquisition time. Since the modulation of B_0 strongly depends on the position, size and material of the implant, the spatial distortion can be different for each patient. Ideally, the minimum amount of SEMAC partitions to cover all relevant off-resonances, $n_{S,r}$, would be determined individually for each patient and slice with the help of a scout scan, i.e. a fast prescan. The acquired SEMAC partitions can be positioned asymmetrically around the slice of interest to save additional scan time [45]. Although the benefits in scan time for a minimum amount of SEMAC-encoding steps are tempting, through-plane ghosting and blurring due to the Fourier transform of a small number of phase-encoding steps can degrade image quality. Overlapping spectral profiles of RF pulses [54], as well as previously mentioned effects due to VAT can affect blurring further on. The impact of high-bandwidth RF pulses on in-plane distortion and blurring may be subject to future studies and be investigated for TSE, VAT and SEMAC sequences. The small sample size of the patient study is a limitation of this work and no statistical implication can be inferred from the data of eight patients. However, this study proves the clinical relevance of the effects demonstrated in the phantom experiments and it illustrates the clinical benefit. Distortion is a subjective measure in this work and an important parameter for image quality. A quantitative evaluation would require exact knowledge about the type and position of the implant. However, this information is not accessible in patient studies.

Investigations using the prototype transmit/receive spine coil reveal both the potential and the limitations of the experimental setup. In contrast to the knee coil, energy is not deposited in the extremities of the patient exclusively and stricter SAR limitations for the body trunk apply. Additionally, very conservative SAR assumptions restrict the imaging performance in vivo. Further investigations are required to overcome this limitation. The declining flip angle in anterior direction is typical for planar transmit coils, but results in a contrast modulation in anterior-posterior direction, which needs to be taken into consideration for diagnoses. A non-optimized receive-coil setup with only two receive channels decreases the signal-to-noise ratio compared to setups using dedicated spine receive coils with multiple channels. Although these downsides are related to the early stage of this prototype, the phantom experiments prove that the specifications of the B_1 field of this coil allow the transmission of high-bandwidth RF pulses which can reduce the spatial through-plane distortion significantly. The indicated extent of the “V”-shaped artifact for both RF modes cannot be used for quantification of the spatial distortion of a single slice like in the phantom experiment with the TKA. Instead, it conveys a sense for the benefit achieved by this coil. The diagnostic value is improved in TSE imaging without increasing scan time or even less scan time is required to compensate for this type of distortion. High-bandwidth RF pulses are not limited to birdcage coils enclosing a preferably small volume, but can also be generated by suitable planar hardware.

To my knowledge, the impact of RF pulse bandwidths on susceptibility-induced distortion has not been studied so far, irrespective of field strength and transmit coil. The benefit of high RF bandwidths is less distinct at 1.5 T compared to 3 T, since their disadvantages

like increased in-plane distortion and blurring apply at 1.5 T equally, but the grade of total distortion is lower and SAR is less limiting at 1.5 T. Using the knee coil for transmission, other postoperative extremities like ankles and wrists could benefit from both the increased RF bandwidth and the reduced SAR limits as well, irrespective of the field strength. The local transmit spine coil used in this chapter enables high-bandwidth RF pulses for postoperative spine imaging. However, savings in scan time are partially abrogated by stricter SAR limits compared to the knee transmit coil.

To sum up, the results of this chapter show that two major limitations in implant imaging at 3 T can be addressed by the use of high-bandwidth RF pulses applied by a local transmit coil: Less restrictive SAR limits apply and through-plane distortion is reduced. Hence, the required amount of SEMAC-encoding steps is decreased; for the specific case of small parts of metal with low differences in susceptibility compared to tissue, SEMAC may become obsolete. Blurring and in-plane distortion may increase for higher RF pulse bandwidths. Homogeneous fat suppression can be obtained by a STIR sequence, whose saturation pulse bandwidth matches the high bandwidth of the excitation RF pulse. In total, all clinically relevant contrasts can be acquired at 3 T with artifacts comparable to 1.5 T without a prolongation of scan time.

5 Shading Close to Metal Structures and Parallel Transmission

This chapter focuses on a type of artifact, which occurs in proximity to elongated metal structures particularly when they are aligned in parallel with the static magnetic field. It is independent of variations of the static magnetic field due to differences in susceptibility and can be addressed separately from the techniques presented and optimized in the previous chapter.

5.1 Materials and Methods

An analysis of the shading close to elongated metal implants and its dependence on the transmit polarization is presented in the beginning of this chapter. The respective theory is validated both numerically and experimentally. Based on this theory, the optimal polarization inducing minimum shading can be determined and it is investigated for different geometries, which are possible for individual patients. The homogeneity of B_1 is reflected in the respective TSE image, which is demonstrated by experiments for various polarizations. In vivo, the analytical model approximating the geometry of the patient is used for optimization of the transmit polarization and compared to an optimization based on experimental B_1 data. The chapter concludes with an exemplary numerical simulation, where improved homogeneity is correlated to the risk of heating.

5.1.1 Theory: Effect of the Transmit Polarization

This section presents a model to describe the modulation of the transmit B_1 induced by hip replacements or other elongated metal structures like proximal femur nails. Their impact on the homogeneity of the total B_1 shall be determined as a function of their spatial position as well as the polarization of a two channel transmit B_1 field. The model assumes the following simplifications: An infinitely long cylinder of radius r_C is filled with liquid of known physical properties. It contains a metal rod of defined length l_R and both the long axis of the cylinder and the metal rod are aligned in parallel with the static magnetic field (figure 5.1). Furthermore, susceptibility effects are neglected. The rod is located at position $\mathbf{p} = (x_p, y_p)$ in the axial plane and the amplitudes of the linearly polarized transmit fields induced by the perpendicular ports in x- and y-direction are given by ${B_1}^x$ and ${B_1}^y$ featuring a phase difference of $\mathrm{d}\varphi$. In the absence of the metal rod, the vector potential inside the

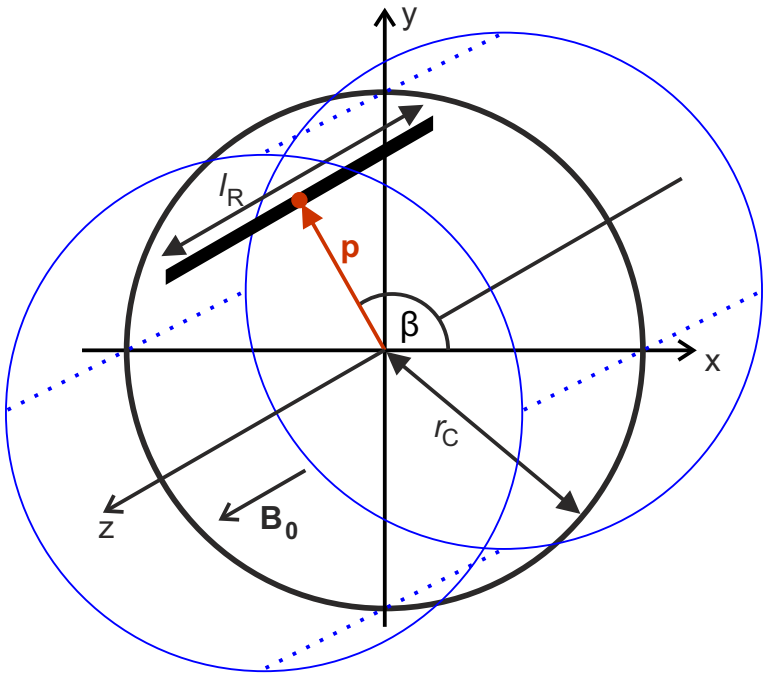

Figure 5.1: Parameters of the cylinder containing a metal rod collinear with $\mathbf{B_0}$ used for the analysis of the homogeneity of B_1.

cylinder is characterized by [113]

$$\mathbf{A}(r,\beta) = -2\,\mathbf{e_z}\,\frac{J_1(k\,r)}{k\,J_0(k\,r_C)}\,(B_1{}^x\,\sin\beta\,e^{id\varphi} - B_1{}^y\,\cos\beta)\ . \tag{5.1}$$

r and β represent the radial and polar coordinates and J_n the Bessel function of nth order. Physical properties of the liquid like its permittivity or electrical conductivity are summarized in k, the magnitude of the complex wave vector. The electric field linked to the vector potential can be derived from the Maxwell's equations [75] and is given by

$$\mathbf{E}(\mathbf{r}) = \frac{i\omega}{2}\,\mathbf{r}\times(\nabla\times\mathbf{A}(\mathbf{r})) \tag{3.11'}$$

for any position $\mathbf{r}$. For the model of an infinitely long cylinder, the vector potential's components in the axial plane are null, hence the electric field is aligned perpendicular to the axial plane and oriented in parallel to the metal rod. This induces a potential difference of

$$U(\mathbf{p}) = l_R\,E_z(\mathbf{p})\ . \tag{5.2}$$

across the rod along the direction of z, which enables the formation of a current in the rod at position $\mathbf{p}$. So far, the analysis of the vector potential and the electric field have been described by the solution of the full Maxwell's equations. This is relevant, since the spatial dimensions of the object can be in the range of the RF wavelength at 3 T field strength. On the contrary, the current in the rod shall be described as a local effect using a near-field approach, as the spatial extent of its impact is small compared to the dimension of the total object. Thus, an electrical equivalent circuit [8] is used for the determination of the impedance of the system (figure 5.2). It contains the inductance L and the resistance R of

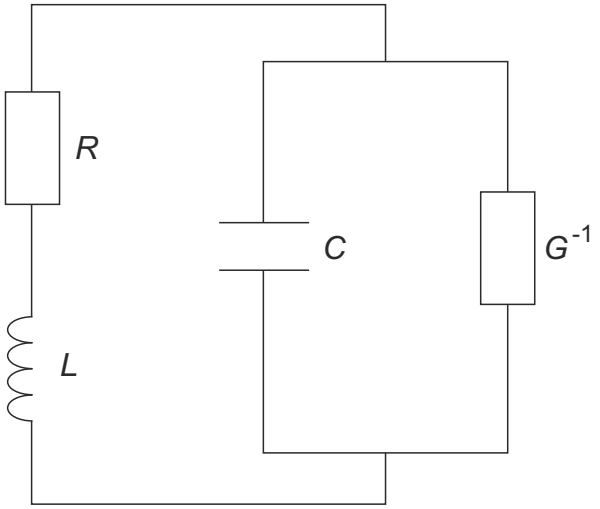

Figure 5.2: Electrical equivalent circuit to derive the impedance of the system.

the rod, as well as the surrounding medium's conductance G and capacitance C. The total impedance Z of the system can be summarized by

$$Z = i\omega L + R + (i\omega C + G)^{-1} \ . \tag{5.3}$$

The resistance R of a metal rod is insignificant compared to the impact of its inductance L at the Larmor frequency of 128 MHz at 3 T field strength. In case of a very short metal rod, the high impedance of the return path through the medium dominates the total impedance and the current will remain small. Though, the share of the impedance of the medium in the total impedance lessens for increasing length of the metal rod, while its longitudinal inductance rises. Assuming a rod of zero resistance embedded in a lossless medium ($G = 0$), inductive and capacitive impedance would cancel if the rod's length equaled half the wavelength of the electromagnetic field (about 13 cm). The significant decline of the impedance involves high currents and it is also known as *resonance effect*. However, the impedance of a conducting medium is smaller. Thus, resonance occurs for rods which are shorter than half the wavelength. For this reason, the total impedance can be approximated solely by the rod's inductance for metal implants longer than about 10 cm and a field strength of 3 T. The current in the metal rod can be approximated by

$$I_z(\mathbf{p}) \approx \frac{l_\mathrm{R}}{i\omega L} E_z(\mathbf{p}) \ . \tag{5.4}$$

Considerable damping related to the resistance of the surrounding medium reduces the intensity of resonance effects. The ratio of capacitive and conductive current of the surrounding medium determines the *Q-factor*, which would be approximately 0.65 for the phantom setup used in this work. Hence, resonance effects are damped and shall not be the primary focus of this work. In accordance with previous publications [8, 34, 90], the impact of the resonance effect is estimated by comparing the wavelength of the RF field to the length of the antenna, i.e. the metal rod.

The induced current gives rise to a magnetic field according to the Biot-Savart law and a conductor of infinite length is assumed for this calculation. The total MR-effective field

$\mathbf{B}_{1,\mathrm{tot}}^{\mathrm{MR}}$ is a composition of the original, undistorted field generated by the two channels of the body coil and the modulation by the current in the rod. It can be approximated by

$$\begin{aligned}\mathbf{B}_{1,\mathrm{tot}}^{\mathrm{MR}}(\mathbf{r}) \approx\ & 0.5\,(\partial_y - i\,\partial_x)\,\mathbf{A}(\mathbf{r}) \\ & + \frac{F}{|\mathbf{r}-\mathbf{p}|}\,(\sin\Psi - i\cos\Psi)\,(y_p\,\partial_y + x_p\,\partial_x)\,\mathbf{A}(\mathbf{r})\ . \end{aligned} \tag{5.5}$$

The angle enclosed by $(\mathbf{r}-\mathbf{p})$ and the abscissa is denoted by Ψ and information about the rod and liquid is included in the scalar

$$F = \frac{\mu_0\mu_r}{8\pi}\,\frac{i\omega l_{\mathrm{R}}}{i\omega L}\ , \tag{5.6}$$

while μ_0 and μ_r represent the vacuum and relative permeability. The original undistorted field is given by the first term in equation (5.5), while the second term of the expression describes the distortion.

According to the model, minimizing the electric RF field at the position of the metal in turn minimizes the current in the metal. Least disturbance of the original transmit B_1 field can be expected in that case. Though, to describe the homogeneity of B_1 in the area of the metal, both the original B_1 and the perturbation must be considered. A nonzero current may act as an RF shim to improve homogeneity.

5.1.2 B_1 Mapping

The theoretical dependence of the modulation of B_1 on the transmit polarization and the position of the metal is verified in phantom studies. In vivo, optimizations based on B_1 maps are performed. These analyses require a technique for B_1 mapping, which is capable to map single transmit channels individually and hence to enable the reconstruction of B_1 maps of any polarization. In addition, considerable off-resonances in the area of the shaft of hip replacements can be induced by the head of the femur replacement, which is often made of CoCr. Hence, insensitivity towards static field inhomogeneity must be considered. A B_1-mapping technique based on a SEMAC sequence focusing on robustness regarding static field inhomogeneities has been introduced [84]. However, acquisition times exceeding 8 minutes per channel are not practicable in vivo. Any B_1 mapping in this work is based on a TurboFLASH sequence equipped with a preceding RF pulse for magnetization preparation [23]. It utilizes slice-selective RF pulses only, which translate static off-resonances into distortion instead of signal drop out (figure 5.3). As additional optimization, all employed slice-select gradients are matched, i.e. the bandwidths of the preparation module and the excitation RF pulse are equal. Thus, no off-resonances are suppressed (cf. ORS). To balance the distortion within the imaging plane and the distortion in slice direction, an RF bandwidth of 1.56 kHz is selected for all applied RF pulses. The nominal flip angle of the RF pulses of the TurboFLASH module is $\alpha_{\mathrm{e}} = 8\,^\circ$. In-plane distortion is limited by the use of a readout bandwidth of 1.5 kHz/Pix. The short echo time ($T_{\mathrm{E}} = 1.83$ ms), which is specific for FLASH sequences, accounts for minimum intravoxel dephasing. A repetition time of 6540 ms is used, as well as a nominal flip angle α_{pre} of $60\,^\circ$ for the preparation RF pulse, which is SINC-shaped. Centric k-space reordering and small matrix sizes are

used to reduce blurring. Any B_1 map in this chapter was obtained with these parameters on a MAGNTEOM Skyra (Siemens Healthcare, Erlangen, Germany). This 3 T scanner is equipped with a body coil enabling two-channel parallel transmission and it was also used for any other image acquisition in this chapter.

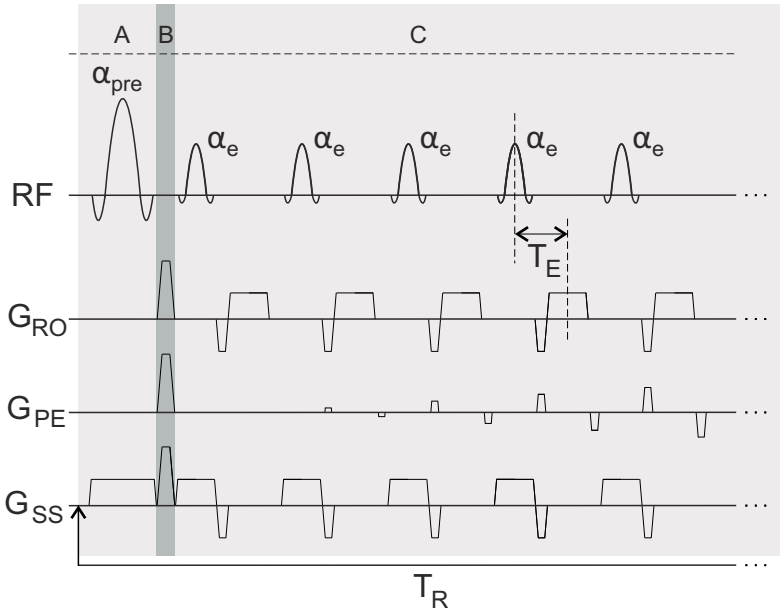

Figure 5.3: B_1-mapping sequence: A preceding preparation RF pulse with a nominal flip angle α_{pre} (A) is followed by spoiler gradients on all three axes (B). A TurboFLASH sequence is used for imaging (C) and α_e denotes the flip angles of the excitation RF pulses.

5.1.3 Validation of the Model

Verification of the model describing B_1 modifications induced by the metal rod as a function of its position and the transmit polarization demands experiments reflecting the true behavior of B_1. In a first step, a B_1 map of a cylindrical phantom was acquired using the technique presented in the previous section. A cylinder filled with doped water (1.25 g hydrated $NiSO_4$ and 5 g NaCl per liter) contains a titanium rod. Both the cylinder and the titanium rod are collinear with $\mathbf{B_0}$. The cylinder's radius r_C is 8.5 cm, it is 36 cm long and the liquid's electrical conductivity and relative permittivity are 0.88 S/m and 80, respectively. The length of the titanium rod is 20 cm and its radius is 0.6 cm. For B_1 mapping, a matrix size of 64×64 resulted in an in-plane resolution of $3.1 \times 3.1\,\mathrm{mm}^2$, the slice thickness was 3 mm and the acquisition of 6 averages yielded a scan time of 3:17 minutes. The phantom was positioned on the patient table of the MR scanner, which resulted in an inevitable spatial shift of 5.3 cm of the isocenter of the phantom with respect to the isocenter of the body coil of the MR scanner. To track possible experimental insufficiency due to differences in susceptibility, a numerical simulation including detailed RF specifications of the scanner was conducted. B_0 determines the Larmor frequency, but the setup neglects the effects related to the static field and it relies on the manufacturer's specification of the two-channel transmit coil. The modulation of B_1 is calculated using the finite integration method of the CST Studio Suite (CST AG, Darmstadt, Germany) and the full Maxwell's

equations were solved for the boundary conditions determined by the experimental setup. The theoretical modulation of B_1 in the cylinder was calculated with the help of Matlab (MathWorks, Natick, USA). The coordinate systems of the analytical and the numerical model were selected to match the scanner's coordinate system. The model was verified for the rod at position $\mathbf{p} = (5\,\text{cm}, 0\,°)$ and for circular polarization, which is the standard polarization and acts as reference. It is described by an amplitude ratio $R = B_1^x/B_1^y$ of 1 and $\mathrm{d}\varphi = 90\,°$.

5.1.4 Dependence of the Optimal Polarization on Geometry

A previous study investigating RF effects correlated to elongated metal implants [34] demonstrated the importance of the radial position of the rod. This statement is substantiated by equation (3.11'), which correlates the electric field to the position of the rod. Therefore, the optimal transmit polarization inducing minimum shading depends on the position of the rod (cf. equation (5.5)) and is different for each patient, just like the combination of implant type and the patient's anatomy is.

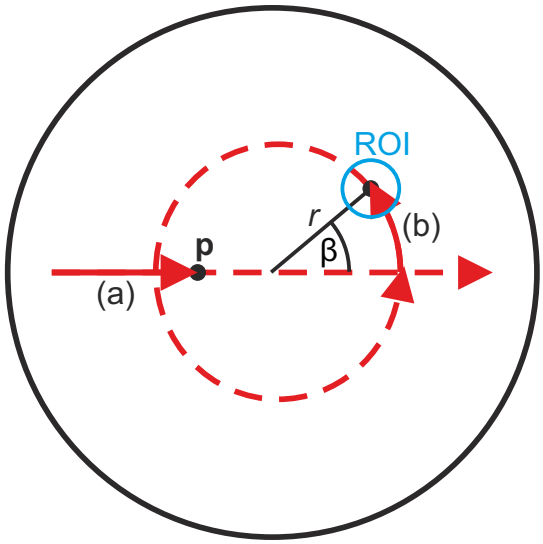

Figure 5.4: Modification of the rod's position and the encircling region of interest (ROI), for which the optimal polarization is determined on basis of the analytical model: alteration of the radial coordinate along the horizontal axis from left to right (a); alteration of the angular coordinate describing a full circle at a constant radial position r (b).

The analytical model was used for investigation of the optimal polarization as a function of the position of the rod: A cylinder ($r_\mathrm{C} = 18\,\text{cm}$) with the electrical properties of the numerical simulation contains a titanium rod ($l_\mathrm{R} = 20\,\text{cm}$), whose position is varied. Figure 5.4 visualizes two different types of modification of the location of the rod. In a first analysis (a), the radial position r of the rod is varied in the range of $-15\,\text{cm}$ to $+15\,\text{cm}$ with an angular position of $\beta = 0\,°$. In a second analysis (b), the polar coordinate covers the range of $\beta = [0\,°;\ 360\,°]$, while the radial coordinate remains constant at $r = 12\,\text{cm}$. For all positions of the rod, the optimal polarization resulting in highest B_1 homogeneity in a region of interest (ROI) was determined. A circular area in the axial plane with the titanium rod

in its center and a radius of 2.5 cm forms the ROI. The standard deviation of B_1 in this area is used as a measure for homogeneity. It was determined for the range of polarizations given by $R = [0.02;\ 45]$ and $\mathrm{d}\varphi = [0\,^\circ;\ 180\,^\circ]$ and homogeneity maps visualizing the standard deviation as a function of transmit polarization are shown for two selected positions of the rod. In addition, graphs reflect the optimal polarization for different geometries.

5.1.5 Homogeneity Correlation of B_1 with TSE Signal Intensity

Previous sections analyze the transmit B_1 field in proximity to metal implants. Clinically relevant sequences for metal implant imaging, however, are based on TSE sequences, which reflect the variations of the transmit B_1 in a complex manner. A locally inaccurate B_1 amplitude results in a modification of the flip angles induced by the RF pulses at this specific position: Each target flip angle is multiplied by a factor, dependent on the true B_1 with respect to the B_1 assumed. Hence, a strong spatial gradient of B_1, which can occur next to metal, can potentially induce a rapid transition of hyper- and hypo-intense signal and affect the contrast of the image. However, not only the transmit B_1, but also its counterpart describing the receive sensitivity (commonly known as B_1^- [51]) is modulated by the presence of the metal. While the body coil is used for the transmission of the B_1 field, multiple dedicated receive coils are used. Nulls may occur where the RF receive fields of the metal rod and single receive coils cancel [90]. These cancelations depend on the orientation of the receive field and are individual for each coil setup. Performing a sum-of-squares combination of all receive coils, the total receive profile may be smeared. Hence, the total receive sensitivity differs from the transmit sensitivity, but both sensitivities modulate the signal intensity in the final image spatially. In contrary, the contrast of the TSE image can be modified during the transmit process only. Please note that all techniques to visualize the B_1 field in this work reflect the transmit B_1 field only and they are not influenced by the receive sensitivity, independent of the receive coils used.

The aim of this section is to link the homogeneity of B_1 to the quality of clinically relevant TSE images. For this purpose, the homogeneity in a specific region of interest of B_1 maps was correlated experimentally with the homogeneity of the signal intensity in respective TSE images. TSE images and B_1 maps of each individual transmit channel were obtained of the phantom used in 5.1.3 with the rod positioned at the same location ($\mathbf{p} = (5\,\mathrm{cm}, 0\,^\circ)$). Dedicated local receive coils were used for signal detection. While one acquisition of the B_1 map was sufficient to generate a homogeneity map for a random range of polarizations, single TSE images were acquired for each polarization separately. The range of polarizations covered amplitude ratios R from 0.1 to 1 in steps of 0.1 and their inverses and thus spaned $[0.1;\ 10]$ in total. Each amplitude ratio was scanned with phase differences from $0\,^\circ$ to $180\,^\circ$ in steps of $15\,^\circ$. The TSE sequence was applied with refocusing pulses of $\alpha_\mathrm{r} = 180\,^\circ$, a readout bandwidth of 700 Hz/Pix and a voxel size of $0.8 \times 0.8 \times 2\,\mathrm{mm}^3$. The turbo factor was 7 and further sequence parameters were $T_\mathrm{E} = 18\,\mathrm{ms}$ and $T_\mathrm{R} = 4000\,\mathrm{ms}$. Parameters for B_1 mapping are identical to the ones used in section 5.1.3. The standard deviation in a ROI encircling the titanium rod with a radius of 2.5 cm was used for the generation of homogeneity maps, both for TSE images and the B_1 data. The range of polarizations was matched. In order to link the homogeneity of the TSE sequence and the transmit B_1 field, the spatial distribution of the signal intensity of a spin echo was simulated on the basis of

the transmit B_1 field as an intermediate step [11]: Neglecting the signal modulation in a spin echo sequence due to relaxation and sequence timing (i.e. T_E, T_R), the signal intensity S can be approximated by

$$S = \sin(\alpha_e)\ \sin^2\left(\frac{\alpha_r}{2}\right)\ . \tag{5.7}$$

The desired flip angles are $\alpha_e = 90\,^\circ$ and $\alpha_r = 180\,^\circ$ and their deviation relates linearly to the B_1 inhomogeneity. The signal intensity of an ideal spin echo is modulated accordingly. On the basis of the resulting spin echo image, the homogeneity in the ROI was determined and besides the homogeneity map for the TSE image and for the distribution of B_1, a homogeneity map for the spin echo image was generated. While the first map is influenced by the receive process, the latter two are not.

5.1.6 Patient Measurements

This section demonstrates the clinical relevance of parallel transmission in respect of shading close to elongated titanium structures in parallel to $\mathbf{B_0}$. The aim is to evaluate two procedures to determine the optimal polarization (based on an experimental B_1 map and on the cylindrical model) and to compare these techniques.

Common examples for degraded image quality due to shading are patients with THA, where this effect occurs next to the femoral stem. Although the stem is commonly made of titanium, the head usually consists of metal alloys introducing considerable off-resonances in the area of the stem. For this reason, the imaging plane used for B_1 mapping is aligned perpendicular to the long axis of the shaft of the implant. Its distal position is defined by the central longitudinal position of the titanium rod, where least effects due to differences in susceptibility are expected. Since the elongated metal structure is approximately collinear with $\mathbf{B_0}$, the plane used for B_1 mapping is almost located in the axial plane. Another imaging plane used for visualization is defined by the x-axis of the scanner and the long axis of the metal structure. For simplification, these planes are referred to as axial^m and coronal^m, respectively, as these are the orientations defined by the coordinate system of the metal. Based on the acquired axial^m B_1 map, a homogeneity map is generated for a circular ROI with a radius of 3 cm aligned with the center of the stem. This map is compared to the respective results of the analytical model approximating the shape of the patient: On the basis of an axial^m TSE image in high resolution, a circle enclosing the body and the position of the titanium are selected manually (figure 5.5). The analytical approach assumes an electrical conductivity of 0.8 S/m and a permittivity of 80 and the homogeneity map is generated for the same ROI as in the experimental analysis. The two resulting homogeneity maps are compared and the optimal polarization is determined and applied in subsequent coronal^m and axial^m TSE imaging. Reference scans in circular polarization are acquired for comparison.

This method was tested in vivo. The study was approved by the institutional review board and two patients signed informed consent. A first patient (#1) had a THA of his left hip with a titanium stem and the head and cup made of a CoCr alloy. Patient #2 had a femoral nail fixation of titanium with a length of 40 cm in the right thigh. Scan parameters of the B_1 map in axial^m orientation were as follows: matrix size 54×96, slice thickness of 3 mm, isotropic

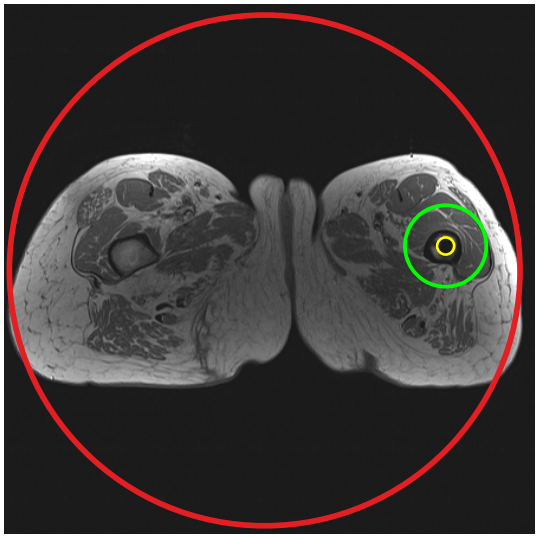

Figure 5.5: Setup used for cylindrical approximation of the body (red circle). The rod (yellow circle), as well as the region of interest (green circle) is valid for both the experimental and the analytical determination of the optimal homogeneity.

resolution in-plane of 3.9 mm and 4.1 mm for patient #1 and #2, respectively. Compared to the phantom study, voxel size in this mapping sequence was enlarged, which increases SNR; hence, the number of averages was lowered to 4 and resulted in a total acquisition time of 2:11 minutes. The comparison of optimized polarization versus circular polarization was visualized using axial^{m} and coronal^{m} T_1-weighted TSE sequences: $T_E = 13\,ms$, $T_R = 750\,ms$, readout bandwidth of 795 Hz/Pix, matrix size axial^{m} $= 189 \times 448$, matrix size coronal^{m} $= 336 \times 448$ resulting in voxel sizes of $1.1 \times 0.8 \times 2\,mm^3$ and $1.2 \times 0.9 \times 2\,mm^3$ for patient #1 and #2, respectively. Local receive coils were utilized for signal detection.

5.1.7 B_1 Homogeneity and Local SAR in a Numerical Human Model

The model in section 5.1.1 is based on the assumption that the intensity of the modulation of B_1 correlates with the strength of the induced current in the metal. As the current scales linearly with the electric field at the position of the metal, stronger heating at the ends of the metal can be expected for polarizations resulting in heavy modulation of B_1 than for optimal polarization [90]. An established parameter for the quantification of heating is the local SAR averaged over 10 g of tissue (SAR_{10g}) [97]. For evaluation of this hypothesis, an approach based on numerical simulation was selected. This allows to monitor the local SAR and thus heating for different polarizations. In addition, not only simple structures like cylindrical phantoms can be examined, but the local SAR in models reproducing human anatomy and tissue properties. Since information about local SAR in patients cannot be gained experimentally within reasonable effort, this opens new ways to correlate modifications of B_1 with local SAR, dependent on the transmit polarization.

For numerical analysis, the simulation setup including a two-channel body coil at 3 T (CST Studio Suite, cf. section 5.1.3) was used. The anatomical model of the adult female named

Ella of the virtual family [22] formed the object and a titanium rod (length 10 cm, radius 3 mm) was placed in its left femur with the top end positioned in the femoral head. As the titanium rod is located within the torso, the analytical model was used to determine the optimal polarization: The shape of the body in the plane perpendicular to the titanium rod and located in the rod's longitudinal center was approximated by a circle and the position of the titanium was adapted. On the basis of this data, optimal polarization resulting in highest B_1 homogeneity in a circular ROI with a radius of 2.5 cm was determined. Using the software for numerical simulation, three-dimensional B_1 maps of Ella in optimal and circular polarization were generated, as well as the corresponding maps representing the value SAR_{10g}. The latter maps do not reflect the magnitude of SAR_{10g} for the corresponding B_1 maps, but they are individually normalized to an average whole-body SAR of 2 W/kg, which corresponds to the limits stated by the International Electrotechnical Commission [52]. This is less biased, as the scanner's specific transmit adjustments are not accessible in case of a numerical simulation.

5.2 Results

This section describes and visualizes the results of the previously described experiments regarding the validation of the analytical model and the analysis of the influence of the position of the rod. It correlates the amplitude of B_1 with signal intensity in TSE imaging and with local SAR.

5.2.1 Validation of the Model

The comparison of the three approaches to determine the B_1 distribution in a cylinder containing doped water and a metal rod is visualized in figure 5.6. Figure 5.6a shows the experimental, b the numerical and c the analytical B_1 map. In close proximity to the metal, all B_1 distributions are in accordance and areas of in- and decreased B_1 coincide. The distribution of B_1 in the analytical model deviates from the other images in larger distance

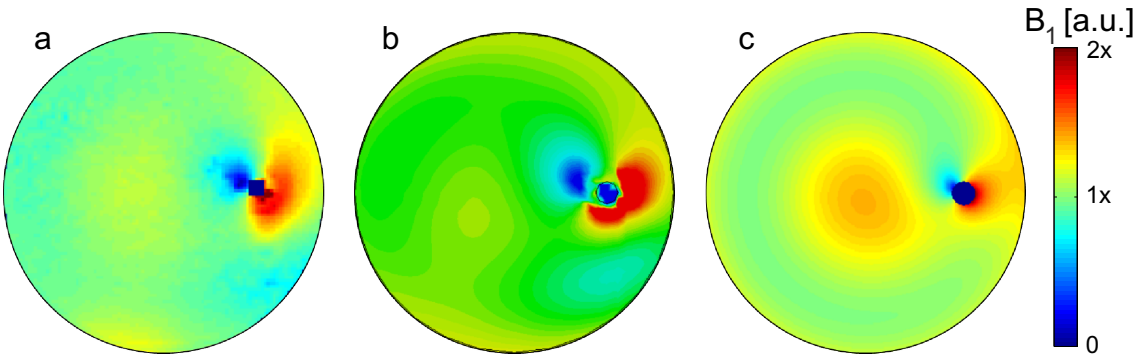

Figure 5.6: Axial B_1 maps of a cylindrical object with a titanium rod at 3.0 T; $r_C = 8.5$ cm and $\mathbf{p} = (5\,\text{cm}, 0\,°)$; these field maps were obtained by experimental B_1 mapping (a), numerical simulation (b) and the analytical model (c).

to the metal. Furthermore, the degree of the modulation by the metal is less intense for the analytical model than for the numerical and the experimental case.

5.2.2 Dependence of the Optimal Polarization on Geometry

The analysis of the dependence of the optimal polarization on the geometry of the object shows strong variations for different positions of the rod. For two setups, not only the optimal polarization, but the homogeneity map, representing the standard deviation within the ROI (figure 5.4) are shown: Figure 5.7a represents the homogeneity as a function of the polarization for the rod at position $\mathbf{p} = (12\,\mathrm{cm}, 0\,^\circ)$, while in b, $\mathbf{p} = (12\,\mathrm{cm}, 45\,^\circ)$. The abscissa represents the phase difference $d\varphi$ and the amplitude ratio is scaled on the logarithmic ordinate. For the rod positioned on the horizontal axis, the optimal polarization is given by $R = 11.0$ and $\mathrm{d}\varphi = 146\,^\circ$, while $R = 0.90$ and $\mathrm{d}\varphi = 174\,^\circ$ result in highest homogeneity for the rod rotated by $45\,^\circ$. Both homogeneity maps feature global extrema only and no rapid changes in homogeneity for slight deviations in transmit polarization.

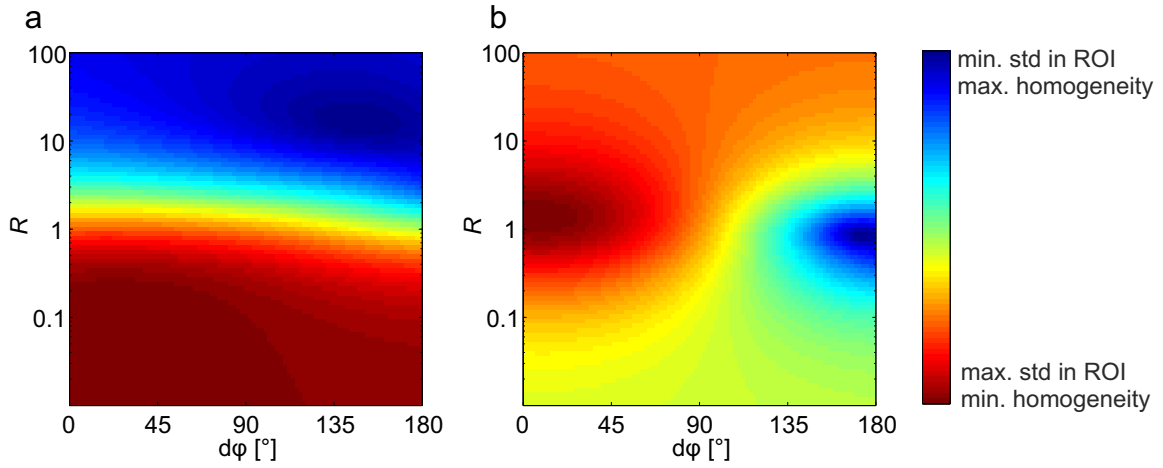

Figure 5.7: Homogeneity maps representing the standard deviation in the region of interest encircling the rod at angular positions of $\beta = 0\,^\circ$ (a) and $\beta = 45\,^\circ$ (b). The values are mapped as a function of the phase difference $d\varphi$ of both channels and their amplitude ratio R.

The optimal polarization as a function of the radial variation of the rod is given in figure 5.8a. For a distance larger than 11 cm from the center of the cylinder, the amplitude of the horizontal port outweighs the vertical one by a minimum factor of 10, i.e. it is almost the sole contributor to the total B_1. Hence, the optimal polarization is approximately linear. With decreasing radial component of the rod, the optimal polarization approaches circular excitation ($R = 1$ and $\mathrm{d}\varphi = 90\,^\circ$), which is the optimum for the rod located in the center of the cylinder. At this position, the electric field component of both transmit ports equals zero, i.e. no current can be induced in the metal, which in turn could create a secondary magnetic field. This relation is independent of the selected polarization. Thus, the transmit polarization generating highest homogeneity in the center of the cylinder in absence of metal remains unchanged, when a metal rod is positioned in its center. Assuming linear polarization ($B_1{}^y = 0$), the zero level of the electric field coincides with the plane described by $y = 0$ and inhomogeneity in a ROI encircling the rod during radial analysis

emanates solely from the inherent inhomogeneity of linear excitation, not from the metal. As this effect increases with decreasing radial component, there is a transition of the optimal polarization from linear to circular with decreasing radial distance of the rod to the center of the cylinder.

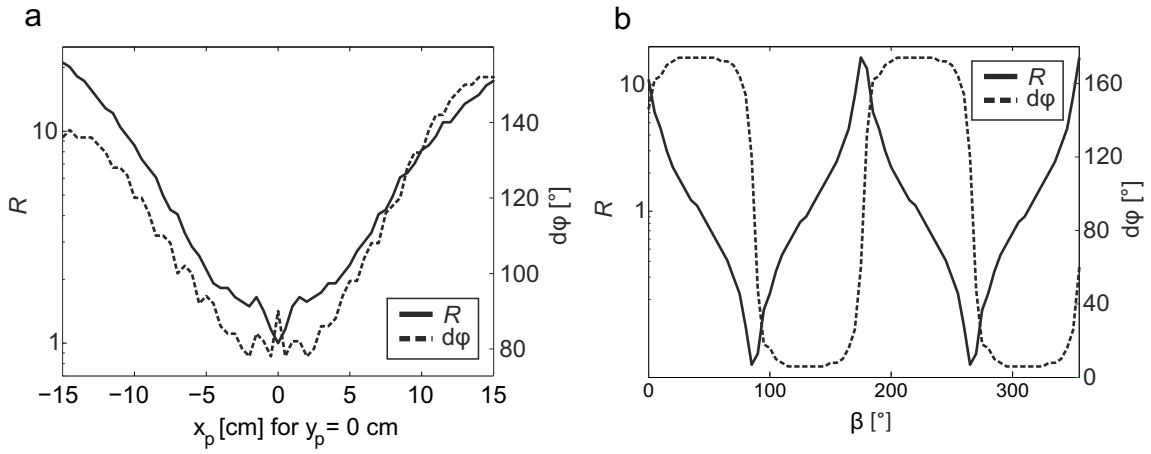

Figure 5.8: Graphs representing the polarization for the highest homogeneity in the region of interest for the variation of the position of the rod as indicated in figure 5.4: variation of its radial (a) and angular position (b).

Figure 5.8b depicts the results of the variation of the polar coordinate β of the rod in the scope of $[0\,°;\ 360\,°]$. The radial component $r = 12\,\text{cm}$ is in the range, where highest homogeneity is achieved for approximately linear polarization as seen in figure 5.8a for the plane described by $y = 0$. The polar analysis supports these results: For polar positions described by $\beta = 90\,°$ and $\beta = 270\,°$, the linear transmit field induced by the vertical channel only results in optimal polarization. Considering the total polar analysis, the values for R and $\mathrm{d}\varphi$ inducing highest homogeneity are periodic to generate a zero level of E_z, which is congruent with the plane described by β.

5.2.3 Homogeneity Correlation of B_1 and TSE Signal Intensity

Figure 5.9 summarizes homogeneity maps obtained by different approaches to allow a comparison between the homogeneity in the regarded B_1 maps and in the TSE images used for clinical purposes. Comparing the homogeneity map based on the experimental B_1 data (figure 5.9a) to the respective homogeneity map obtained on basis of the generated SE images (figure 5.9b), least standard deviation in the ROI is obtained for the same polarization ($R = 9$, $\mathrm{d}\varphi = 120\,°$). While small B_1 inhomogeneity is reflected similarly in the homogenetiy of SE images, this is no longer true for strong B_1 inhomogeneities: Polarizations yielding strong variations of B_1 in the ROI generate even more intense inhomogeneities in the respective SE signal. The higher susceptibility of the spin echo to strong inhomogeneities originates from the signal intensity's dependence on the flip angles according to equation (5.7). In contrast, the homogeneity map based on TSE images differs. The extended area of polarizations resulting in relatively good homogeneity within the ROI (marked in light to dark blue) is approximately in agreement with the results based on the SE and B_1 data.

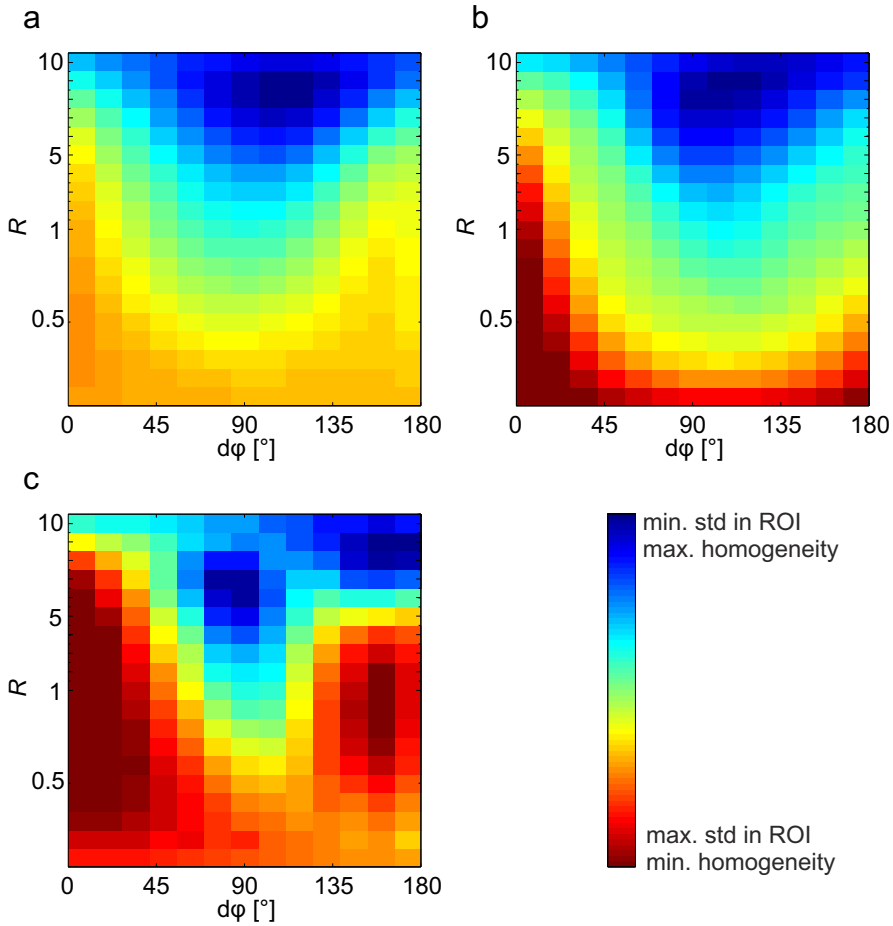

Figure 5.9: Homogeneity maps based on the experimental B_1 map (a), SE images generated on the basis of the B_1 data (b) and based on acquired TSE images (c) for the phantom setup shown in figure 5.6.

Though, excellent polarizations according to the B_1 map (R in the range of 7 to 10 and dφ in the range of 90 ° to 135 °) are not reflected as excellent polarization in the TSE images. In addition, inhomogeneities in TSE images for polarizations resulting in medium to strong B_1 inhomogeneities are intensified compared to SE images. Subdividing all three homogeneity maps in figure 5.9 into good and bad polarizations, the results are roughly the same. The optimal polarization determined on basis of a B_1 map can be expected to yield a relatively homogeneous TSE image.

5.2.4 Patient Measurements

Figure 5.10 visualizes homogeneity maps of both patients, obtained by acquired B_1 maps and cylindrical approximation. The procedure to assign the cylinder's circumference and the location of the rod and the ROI is shown exemplarily for patient #1 in figure 5.5. For this patient, the homogeneity map based on experimental data features highest homogeneity, i.e. minimum standard deviation in the ROI, for the optimal polarization described by the amplitude ratio of $R = 3.7$ and the phase difference of d$\varphi = 180\,°$ (figure 5.10a). Highest

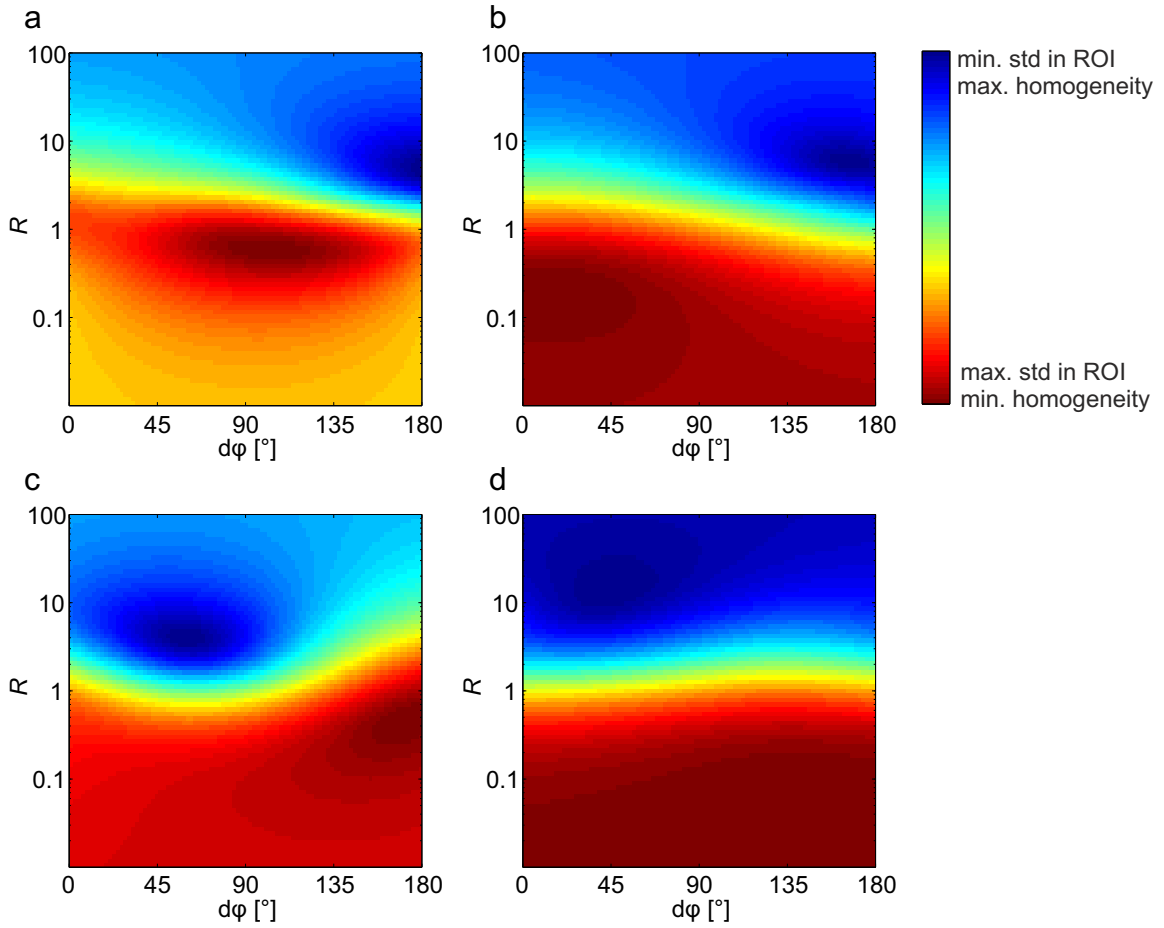

Figure 5.10: Homogeneity maps determined in different modes representing the standard deviation in the region of interest for both patients; experimental (a) and analytical mode (b) for patient #1 and experimental (c) and analytical mode (d) for patient #2.

standard deviation, i.e. strongest inhomogeneity is obtained for $R = 0.7$ and $\mathrm{d}\varphi = 98\,^\circ$, which is close to quadrature polarization. The respective cylindrical approach (figure 5.10b) results in an optimal polarization of $R = 4.4$ and $\mathrm{d}\varphi = 168\,^\circ$. According to the homogeneity map based on B_1 data for patient #2 (figure 5.10c), optimal polarization is given for $R = 3.3$ and $\mathrm{d}\varphi = 60\,^\circ$. The respective map for the cylindrical model encircling both legs predicts an optimal polarization of $R = 9.0$ and $\mathrm{d}\varphi = 44\,^\circ$. The plane used for B_1 mapping is in central longitudinal position of the gamma nail, which is positioned outside the body trunk; i.e. a considerable air gap separating both thighs cannot be captured in the cylindrical model. The optima based on B_1 data in vivo illustrate the relevance of the analysis of the dependence of the optimal polarization on the cylinder geometry (cf. section 5.2.2) for clinical use: The right hip implant of patient #1 is located at a polar angle of $\beta_1 = 8\,^\circ$, while $\beta_2 = 170\,^\circ$ for patient #2. Comparing the corresponding optimal polarizations of the analytical angular study (figure 5.8b), the phase difference for a small polar angle ($\beta \approx 10\,^\circ$) describing the position of the rod is significantly larger than for the rod mirrored at the vertical axis, while the amplitude ratios are comparable. For both patients, the optimal polarization requires a minimum amplitude ratio of 3.3, i.e. the horizontal port is the main contributor to the total B_1.

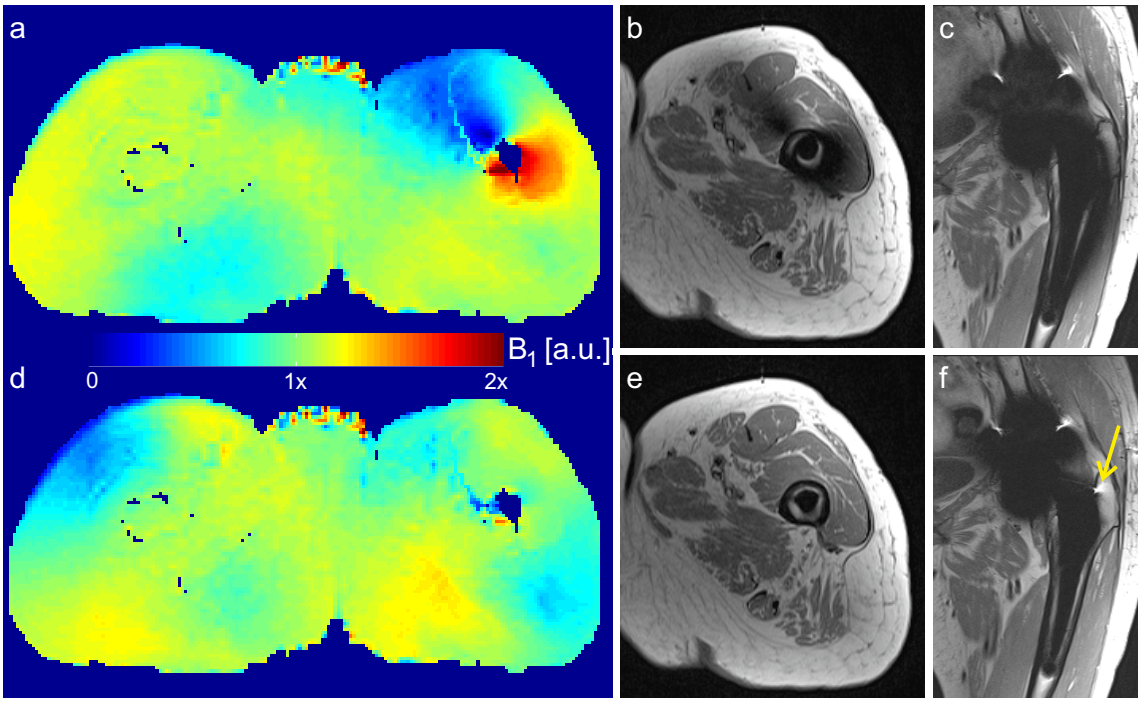

Figure 5.11: B_1 maps in circular (a) and optimal polarization ($R = 3.7$, $d\varphi = 180\,°$) (d) for patient #1 and the corresponding images acquired with a T_1-weighted TSE sequence: axial^m (b) and coronal^m (c) in circular polarization for visualization of the extent of the shading and the same slices in optimal polarization (e,f); additional signal pile-ups become visible in optimal polarization (yellow arrow).

The effect of the optimized polarization in comparison to standard quadrature imaging is visualized in figure 5.11 for patient #1. The B_1 map in circular polarization (5.11a) features its maximum amplitude in the bottom right corner of the hip stem, which is 2.1 times the average B_1 of the total slice, while in the opposite corner, B_1 converges zero. The corresponding axial^m TSE image in circular polarization (figure 5.11b) suffers from signal loss in the top left corner, while high B_1 in the opposite corner accounts for a rapid transition between hyper- and hypointense signal. The extent of the area of signal drop-out becomes visible in the coronal^m image in this polarization (5.11c), where a black vertical band in varying distance to the titanium shaft is visible. In contrast, homogeneous B_1 in the area close to the metal is obtained in optimal polarization ($R = 3.7$ and $d\varphi = 180\,°$) in figure 5.11d. This improved homogeneity eliminates shading and RF imaging artifacts are limited to slight variations in signal intensity inside the femur in immediate adjacency to the titanium (figures 5.11e,f). The area of the femoral head, which is of CoCr, is strongly affected by signal loss and pile-up artifacts, irrespective of the polarization of the transmit field. One location affected by signal pile-up in optimal polarization (yellow arrow in figure 5.11f) is not visible in circular polarization, where shading superimposes.

The effect of optimal polarization ($R = 3.3$, $d\varphi = 60\,°$) for patient #2 is visualized in figure 5.12. Although the polarization inducing highest inhomogeneity ($R = 0.5$, $d\varphi = 174\,°$) for patient #2 deviates more from circular polarization than for patient #1, the B_1 map in circular mode (figure 5.12a) shows strong variations in the region of interest around the femoral nail fixation compared to the map in optimal polarization (figure 5.12d).

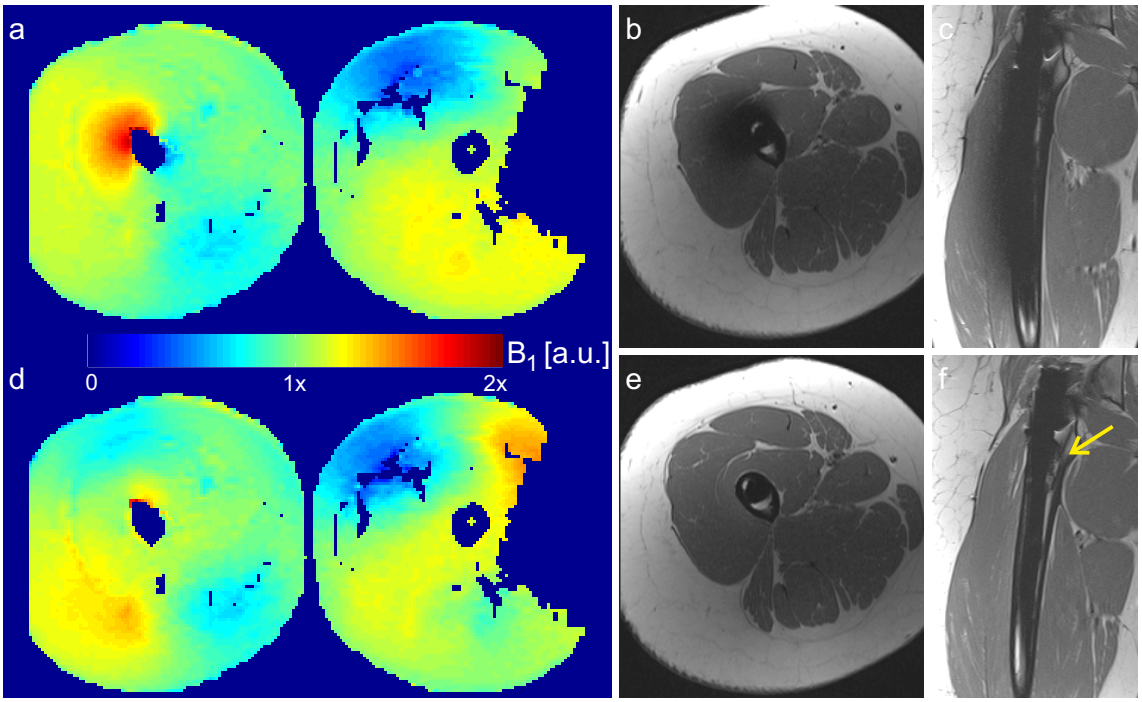

Figure 5.12: B_1 maps in circular (a) and optimal polarization ($R = 3.3$, $d\varphi = 60\,°$) (d) for patient #2 and the corresponding images acquired with a T_1-weighted TSE sequence: axial^m (b) and coronal^m (c) in circular polarization for visualization of the extent of the shading and the same slices in optimal polarization (e,f); fractures become visible in optimal polarization (yellow arrow).

Asymmetric positioning of the receive coils to improve signal intensity in the region of interest results in slight information loss on the left thigh. In quadrature polarization, the intensity of B_1 in the top left corner of the titanium is 2.0 times the average B_1 of that slice. In the respective axial^m TSE image (5.12b), the increased B_1 results in a rapid transition between hyperintense signal inside the femur and hypointense signal in the adjacent muscle. The shading is also visible in the respective coronal^m image on the left side of the implant (figure 5.12c). TSE imaging in optimal polarization (figures 5.12e,f) limits artifacts to sparse and irregular changes of contrast inside the femur and makes healed fractures visible (arrow in figure 5.12f).

5.2.5 B_1 Homogeneity and Local SAR in a Numerical Human Model

Figure 5.13b illustrates an axial^m B_1 map of Ella in circular polarization. The model contains a titanium rod inside the left femur. The cylindrical model approximating the body is defined by a radius of 22.6 cm and the position of the titanium rod is given by $\mathbf{p} = (12.5\,\text{cm}, 1.5\,\text{cm})$. The resulting optimal polarization based on the analytical approach is given by $R = 5.47$ and $d\varphi = 166\,°$. Figure 5.13c demonstrates the respective B_1 map in optimal polarization. Figures 5.13a and d illustrate the coronal^m distribution of B_1 for both polarizations. It is important to note that the optimal polarization is only an approximation based on the analytical model. Other polarizations might provide equal or better

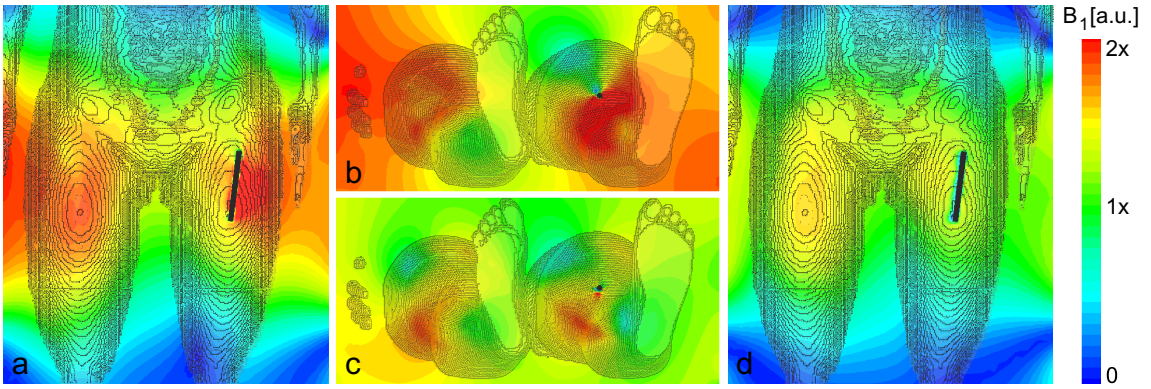

Figure 5.13: B_1 maps in circular (a, b) and optimal polarization ($R = 5.47$, $d\varphi = 166\,°$) for Ella (c, d). A titanium rod was inserted in the model's left femur.

B_1 homogeneity close to the metal. Still, comparing circular to the given optimal polarization, a significant difference becomes visible: While the rod separates areas of strong B_1 amplification from areas of strong B_1 attenuation in circular polarization (figures 5.13a,b), both the amplitude and the spatial extent of areas of amplified B_1 are reduced significantly in optimal polarization. Furthermore, increased homogeneity in proximity to the rod in optimal polarization does not cause degradation of B_1 in areas in farther distance to the rod. Maps visualizing the distribution of SAR averaged over a volume of 10 g of tissue are shown in figure 5.14. This measure does not exist for the surrounding air, but within the object, only. The coronal^m SAR_{10g} map in circular polarization (5.14a) depicts a significant increase of the local SAR at both ends of the titanium rod, while the one in optimal polarization (5.14d) shows excellent homogeneity. The respective axial^m maps unveil areas of intense SAR away from the metal in optimal polarization (5.14c), which is less distinct in circular polarization (5.14b) for the axial^m map positioned in the longitudinal center of the rod. Though, the peak value of SAR_{10g} in the entire body is 44.3 W/kg in circular polarization in a distance of only 5 mm to the top end of the metal rod. In contrast, the peak SAR_{10g} is 39.8 W/kg in optimal polarization located 5 cm in posterior direction of the metal rod. It is important to note that both SAR_{10g} maps do not necessarily reflect the impact of equal underlying RF pulses or flip angles. They merely reflect the local SAR distribution, when the maximum whole-body averaged SAR of 2 W/kg is exploited for the respective polarization.

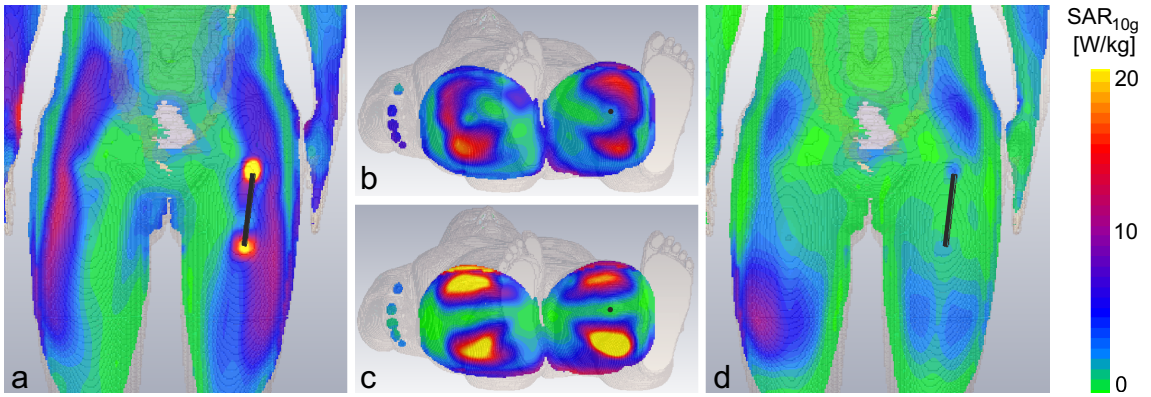

Figure 5.14: Maps reflecting SAR_{10g} in circular (a, b) and optimal polarization for Ella (c, d).

5.3 Discussion

In this chapter, shading in proximity to long metal structures due to currents induced by the transmit RF field is analyzed and its dependence on the polarization of the transmit field is investigated. Two techniques are introduced to determine optimal polarization resulting in considerably less shading compared to circular polarization. One technique is based on B_1 mapping, where the underlying sequence is an adaption of the turboFLASH sequence. The respective B_1 maps are little sensitive to differences in susceptibility and within the resolution of the map, no intra-voxel dephasing can be noted close to titanium. Since the head of total hip replacements is often made of metals other than titanium, e.g. CoCr, positive off-resonances of $\mathbf{B_0}$ can occur in the area of the shaft [109]. Orienting the imaging plane for B_1 mapping perpendicular to the long axis of the shaft, the impact of susceptibility-induced distortion on B_1 maps can be decreased. An experimentally obtained B_1 map of a phantom is in agreement with the respective result from a numerical simulation, which includes all relevant RF data from the experimental setup. Hence, eddy currents due to gradient switching [26, 35] and other effects, which are not reproduced in the numerical simulation, do not affect the observed shading. The assumption, that shading originates exclusively from the transmit RF field, is valid within the limits of experimental accuracy.

The B_1 map generated by the analytical model for this experiment differs slightly. Deviations in farther distance to the metal can be explained by the near-field approach, which is used to describe the current in the metal rod and its impact on the total B_1 field. Another source of currents in metal structures of this size is the B_1-field component perpendicular to the surface of the metal. According to Farady's law, shielding currents are induced along the surface of the rectangular cross-section of the rod [34]. This effect is also modeled in the numerical simulation and it is independent of the electric RF field. However, the ratio of the shielding current to the current induced by the electric RF field is very small unless $E_z(\mathbf{p})$ approaches zero. In addition, the behavior of the shielding current can be described by a line dipole, whose induced B_1 field declines faster with increasing radial distance than the one induced by the electric RF field, which can be described by a line monopole. Hence, the impact of the shielding current on the total B_1 can be neglected in the utilized phantom setup in circular polarization. Areas of amplified and attenuated B_1 are reflected correctly in the analytical model, but the degree of the perturbation is underestimated: The intensity of amplification and attenuation of B_1 declines faster compared to the experiment and the numerical analysis. This deviation might be caused by an undervalued current in the rod, as resonance effects were not considered for analytical modeling. Since half the wavelength of the RF field (resonance length) is 13.1 cm in the surrounding medium at 3 T and the length of the rod is 20 cm, the system is not supposed to be in resonance. Though, the spatial properties of the phantom restrict the validity of the simplifications made for the analytical model: The volume of the medium surrounding the rod is limited due to the vicinity of the rod to the wall of the phantom (3.5 cm). Hence, the conductance of the medium is reduced compared to the assumptions made for the model, which in turn undervalues the impedance of the liquid. As a consequence, the relative contribution of capacitive currents is higher than expected. This increases both the half-wave resonance length and the Q-factor, which in turn can be expected to raise the current in the rod due to resonance effects. In comparison to the analytical model, the resonance current would increase the absolute deviation of B_1, i.e., both amplification and attenuation. Yet, the aim

of the analytical model is to describe the homogeneity in a ROI in immediate proximity to the rod and to enable the optimization of the polarization based on these results. Upon condition that the undistorted, original B_1 can be assumed to be constant within this ROI for any transmit polarization, the underestimation of the current has no impact on the final result, which is to describe the homogeneity of the signal in the ROI.

Homogeneity maps were introduced to describe the standard deviation in a ROI encircling the metal as a function of the polarization of the transmit field. All homogeneity maps illustrated in this chapter, both based on the analytical model and experimental data, and the ones used for the analysis of the optimal polarization as a function of the position of the metal rod, feature global extrema only. In addition, a significant difference between optimal polarization and the one inducing strongest inhomogeneity in the ROI can be observed in all illustrated homogeneity maps. Furthermore, their gradient is rather small. Hence, homogeneity degrades little for transmit polarizations slightly differing from the optimal polarization. Theoretical analyses demonstrate the particular importance of the optimal polarization compared to circular polarization for an increasing radial coordinate of the rod. Since the electric field component of the transmit field scales approximately linearly with the radial coordinate, no current is induced in the metal at the central position of the cylinder. In human anatomy, hip replacements and femoral fixations are located laterally. In such areas, strong inhomogeneities became visible both in B_1 maps and TSE images in circular polarization. As long as the metal structure is positioned within the torso, the spatial variation of B_1 can be approximated well by the cylindrical model. This is valid for total hip replacements, but not for long intramedullary rods mainly located in the femur, where the influence of the air gap between both legs on the B_1 amplitude cannot be considered in the cylindrical model (cf. patient #2). To sum up, the presented results verify the hypothesis that the simple analytical model is valid for the prediction of B_1 close to elongated metal structures, as long as these are positioned in the trunk and approximately collinear with $\mathbf{B_0}$. Under these circumstances, the necessary spatial parameters can be extracted for each individual patient and used for the optimization of the transmit polarization. A localizer image might be convenient and time-saving, since the acquisition of a separate B_1 map would be redundant. If a B_1 map is required, for example due to the position of the metal in the thigh, the presented sequence could be applied with fewer averages to save scan time at the cost of SNR. The latter two suggestions have not been investigated with respect to robustness, yet. A software package for investigations on a larger patient group has been prepared and a cooperation with a clinical research group is active. These investigations may also correlate certain parameters describing the geometry of the object to the optimal polarization: Factors like the laterality of the implant, patient weight and gender might allow the approximation of the optimal polarization. This information could redundantize sophisticated calculations or additional measurements like B_1 maps.

In clinical imaging, not the transmit B_1 field itself is decisive, but its impact on the final image. Since TSE-based sequences are commonly used in metal implant imaging, a homogeneity map based on TSE images was correlated to the respective one based on B_1 data. As an intermediate step, SE images were generated on the basis of the B_1 distribution. Substantial inhomogeneity of B_1 appears intensified in the corresponding hypothetical spin echo image and even stronger in the respective acquired TSE image. The enhancement of strong B_1 inhomogeneity for hypothetical spin echoes can be explained by signal rollovers for B_1 amplitudes higher than twice the average. In areas of good B_1 homogeneity, B_1 amplitudes

do not span a range larger than twice the average B_1 amplitude. Hence, signal rollovers do not occur and B_1 inhomogeneity is not intensified in the respective spin echo image. In contrast, the signal intensity in experimental TSE images is more complex: Besides the increased number of refocusing pulses introducing a more complicated dependence of the signal intensity on the transmit B_1, sequence timing and receive sensitivity affect the spatial distribution of the signal. This is one possible reason for the intensification of substantial inhomogeneity of B_1. In addition, polarizations yielding highest B_1 homogeneity appear slightly more inhomogeneous than neighboring polarizations in TSE images. The excellent homogeneity of the transmit field generates both a constant signal intensity and a uniform contrast within the area regarded. However, signal intensity is also modulated by the receive sensitivity of the individual coil setup, which differs from the transmit sensitivity of the body coil. The impact of the receive process on the total signal intensity is presumably small compared to the transmit process, since the performed signal combination (sum-of-squares) of multiple receive coils mitigates local signal cancelations that may be present in single coil images. However, this effect is independent of the transmit process and may influence the signal intensity visibly for the optimal transmit polarization. It is important to note, that the receive sensitivity cannot be mapped as easily as the transmit sensitivity and its impact on the final TSE image is minor. These results verify the investigations in this chapter, where the polarization for TSE imaging in vivo is optimized on the basis of B_1 maps, since optimization based on TSE images is not feasible due to the related scan time. B_1 mapping to determine the optimal polarization is a time-saving option yielding good accuracy.

In hip implant imaging, the correct visualization of the tissue in immediate distance to the femoral stem is critical. The determination of the optimal polarization generating highest homogeneity in a ROI with a diameter of 6 cm can exclude misinterpretations such as regarding mechanical loosening or circumferential fibrous membrane formation. Not only in the regions of interest, but also in the whole axial slices of both patients, B_1 in optimal polarization does not appear to be more inhomogeneous than in circular polarization. However, there is one parameter, which imposes limitations on the free selection of optimal polarization: The whole-body SAR is minimal for circular polarization, since it generates a perfectly forward-polarized field distribution [28]. Though, strong inhomogeneities in proximity to the metal occur in circular polarization in both patients and optimal polarization is created mainly by the horizontal port, which outweighs the vertical one by a factor of at least 3.3. Hence, optimal polarization is approximately linear. For pure linear polarization, the whole-body SAR doubles in comparison to circular polarization [28]. This is critical, since SAR restrictions are a general challenge in orthopedic imaging with metal implants [47], especially at 3 T field strength [121]. Methods for the reduction of SAR generally include the use of low refocusing flip angles, which in turn degrade the image contrast and hence image quality [1], and an increase of scan time to lower the density of applied RF pulses averaged over time [47]. Therefore, the application of RF pulses in optimal polarization can minimize shading, but it also can be linked to an increased scan time compared to circular polarization due to increased SAR deposition. The smooth behavior of the homogeneity maps for both patients indicates little degradation of B_1 homogeneity for a polarization imposing slightly less SAR than the optimal polarization.

Safety in MRI in the presence of metal is an active field of research. Studies covering heating and safety are fundamental for interventional MRI. Various publications have investigated

RF effects in guide wires and analyzed the heating of the surrounding medium in MR imaging to improve safety [91, 93, 119]. Latest research also exploited the capabilities of parallel transmission [29, 30]. Publications focusing on RF effects in hip replacements [85, 97, 103] and intramedullary rods made of titanium [86] analyzed heating and safety aspects: According to a numerical study, local SAR and hence the risk of heating caused by bilateral hip replacements made of CoCr is not increased at 3 T compared to 1.5 T [97]. In a phantom experiment, titanium implants were less prone to heating than replacements of CoCr [85]. In this work, the homogeneity of B_1 was correlated to local SAR which is a measure for heating. Using a numerical simulation, this analysis was performed for a female human model. Again, homogeneity of the B_1 field was improved compared to circular polarization by the determination and selection of the optimal polarization. The CST Studio allowed the calculation of the global and local SAR averaged over a volume of 10 g of tissue. For the specific human model comprising a titanium rod in its hip, improved homogeneity of B_1 resulted in less local SAR deposition at the ends of the metal rod. Hence, heating and burns at these specific locations harming the patient are less likely for optimal polarization than for circular polarization. Though, the optimal polarization for the human model tends towards linear polarization primarily sustained by the horizontal channel, which is in rough agreement with the optimal polarizations obtained for both patients. Despite the significant increase in homogeneity for this transmit polarization, local SAR deposition increases in areas close to the anterior and posterior surface of the trunk. This effect is independent of the presence of metal and must be considered in the model used for SAR monitoring. Still, the peak SAR in this setup is higher in circular polarization than in optimal polarization. This analysis shows that the use of the optimal polarization in MRI is capable to reduce heating in immediate proximity to the metal. In turn, the optimal polarization may increase the total SAR or introduce spots of enhanced SAR independent of the metal. Generally, heating cannot be quantified by the size of RF induced artifacts or the spatial extent of the B_1 perturbation, as the electrical properties of the environment are decisive for heating. In a surrounding medium characterized by low damping, for example, severe perturbations of B_1 are hardly related to heating. Though, for a given setup with constant electric properties, effects like damping are not influenced by the transmit polarization. Likewise, a polarization nullifying the electric field component of the transmit field at the position of the metal reduces the current in the rod compared to any other polarization. To predict the heating related to the current in the metal and hence the induced RF artifacts, fundamental knowledge about the whole setup is essential and thus individual for each object. For a substantiated statement about the correlation of increased homogeneity and improved safety, more profound numerical simulations and experimental studies are required. However, appropriate investigations would exceed the extent of this work.

The aim of this chapter is the analysis of B_1 shading close to elongated metal implants and the presentation of techniques how to eliminate this effect. This was presented for two patients. For both cases, the horizontal transmit channel outweighed the vertical one in optimal polarization, but the respective phase differences varied. It is important to note, that shading is an effect independent of susceptibility-induced artifacts and hence can be tackled independently. This work used optimal polarization combined with TSE sequences optimized for metal implant imaging. However, any MR imaging sequence, including MSI or SPI techniques to minimize susceptibility-related artifacts, can be combined with the optimal transmit polarization. In addition, the individual adjustment of the transmit po-

larization is not limited to metal implants in the region of the hip. Other important clinical applications, e.g. imaging of metal rods along the spine or intramedullary rods in the humerus, could benefit from this technique as well.

To conclude, RF-induced shading in proximity to long metal structures is described as a function of the polarization of a two-channel transmit B_1 field in this chapter. The modification of the MR-effective B_1 close to the metal and the involved artifacts are influenced strongly by both the original B_1 and by the location and orientation of the metal inside the object or the patient. The correct selection of the transmit polarization can ameliorate arising artifacts, while this polarization can be selected by different options: either on the basis of the analytical model presented in this chapter or on the basis of a B_1 map. This chapter presents images of elongated metal implants at 3 T, which are not disrupted by shading. This proves that two independent transmit channels are capable to perform B_1 shimming close to hip implants and gamma nails such that RF artifacts at 3 T are reduced substantially.

6 Discussion and Outlook

The clinical impact of magnetic resonance imaging in the presence of metal implants is significant. Artifact-free images can improve diagnoses to determine inflammations and water accumulation indicating the loosening of metal implants, for example. The increasing number of surgeries involving temporary or permanent metal fixtures and joint replacements and the improved availability of MR scanners increase the share of the population to benefit from techniques which enable MRI with minimum artifacts in the presence of metal. With the establishment of 3 T in clinical routine, solutions are required to counter the increased scan time for artifact correction, involving less patient comfort, higher likeliness of motion artifacts and restricted economic benefit. So far, no dedicated solutions for 3 T have been presented except for acceleration methods, which allow to spend the benefit in scan time on additional encoding at 3 T. In this work, two approaches have been investigated to face the enhanced level of artifacts at 3 T in a limited scan time.

The first study of this work focused on the exploitation of the hardware limits of a dedicated transmit/receive knee coil at 3 T. The higher peak B_1 as well as the local SAR deposition in the extremities allow the application of RF pulses with bandwidths up to 4 kHz. In contrast, the body coil is capable to generate RF pulses with similar slice profiles of about 1 kHz bandwidth. Through-plane distortion relates inversely to the RF pulse bandwidth. Its correction is time-consuming and acquisition time for correction scales linearly to the distortion. Thus, the application of high-bandwidth RF pulses decreases scan time substantially, when optimal artifact reduction is desired. For patients with total knee replacements or plate osteosyntheses in the region of the knee, 3 T MRI is no longer impedimental. This technique is not limited to MRI at 3 T in the presence of metal, but can also be used at lower field strength, when local transmit coils are available. Though, less benefit is expected at lower field strength: Usually, body coils of 1.5 T scanners are designed with higher peak B_1 compared to 3 T scanners such that higher RF pulse bandwidths can be achieved by the body coil. Thus, the gap to the RF pulse bandwidths induced by local transmit coils decreases. Still, further studies may investigate the benefit of local transmit knee coils at 1.5 T and test the impact of these coils in a clinical environment, both at 1.5 T and 3 T. Similar advantages can be obtained by a local spine transmit coil. A variety of applications are possible, provided that suitable hardware is available. Considering the active field of coil research in MRI, future applications may include more joints than the knee. A general advantage of local transmit coils is the limited region, that is irradiated by the RF field. Using a body coil for transmission, the user must assume the whole object to be affected by the RF pulses. Thus, for a limited FoV in the body trunk, cautious selection of its spatial extent and positioning of the receive coils are required to avoid aliasing artifacts. In musculoskeletal MRI, hip implant imaging is particularly challenging due to the desired high resolution. For this application, a local transmit coil may be beneficial not because of SAR, but because of the limited volume to be excited, which may even redundantize

oversampling in direction of phase encoding. Additionally, its enhanced peak B_1 may be exploited for the bandwidth of the RF pulse. Though, this coil may be difficult to build due to highly differing body circumferences among the population. Another active field of research related to metal implants deals with their safety in MRI. This is a very complex topic and must be studied for high-bandwidth RF pulses. Experiments in this work considered the global SAR limits; the global SAR comprises the enhanced power of high-bandwidth RF pulses compared to conventional RF pulses. However, there is not yet a general SAR model considering the effects of metal inserts and their individual setup. Hence, currents in the metal have not been correlated to RF pulse bandwidths yet. Results indicate B_1 shading possibly induced by currents, which becomes visible for high-bandwidth RF pulses only and might introduce local heating. A numerical analysis is required to model the complex structure of implants inside the body and to determine the local SAR distribution, which is commonly used as a measure for heating and thus safety. The general clinical acceptance of high-bandwidth RF pulses is expected to be high, as its implementation allows a straightforward application. The results of this work show substantial improvement in artifact reduction and even enable scan time reduction. Those benefits are widely desired by clinicians.

In this work, shading close to elongated metal implants and its dependence on the transmit polarization were analyzed for the first time. The analytical model illustrated the effect in detail and the transmit polarization proved as a powerful tool to control the shading. The effect was highly subject to the position of the metal and the spatial extent of the object. As quadrature polarization resulted in strong shading artifacts in both patient cases, the optimal polarization must be determined individually. A larger group of patients is required to investigate correlations between optimal polarization and patient-specific parameters like implant laterality. Again, the safety analysis for hip replacements and their dependence on the transmit polarization has not been finalized. Initial numerical simulations showed reduced local SAR in immediate proximity to the metal for the optimal polarization compared to the reference, but enhanced local SAR in other parts of the body. Its impact on safety should be studied in an experimental setup. So far, the foundation for an MRI application has been developed and final application procedures have been drafted. Moreover, clinical images proved the high impact of the transmit polarization and thus the benefit of this technique. Subject to the condition that the optimal polarization is easily ascertainable and can be robustly applied for each patient, this technique is a potential feature in future clinical MRI. Considering the enhanced global SAR of the optimal polarization compared to circular polarization, optimal polarization will be combined most effectively with TSE and VAT sequences. Since their acquisition times are short compared to MSI techniques, a penalty in scan time due to the enhanced global SAR in optimal polarization is less critical. Thus, shading can be addressed independently of susceptibility-induced artifacts and the clinical protocol will be a mixture of TSE or VAT sequences in optimal polarization and SEMAC or MAVRIC-SL in circular polarization or polarizations balancing SAR and B_1 homogeneity. For hip stems of titanium and heads of CoCr, this is a viable option, while for intramedullary rods of titanium, SEMAC is not required. This combination will satisfy clinical needs until a method for substantial acceleration of SEMAC or MAVRIC-SL has proven robust in clinical routine.

In general, techniques to counter susceptibility-induced through-plane artifacts are still time-consuming. In addition, the functionality of frequency encoding is limited in regions

of extreme gradients of the static magnetic field. Single-point techniques offer the only option to bypass this limitation, but these methods are even more challenging in terms of scan time than MSI techniques. Either approach must be accelerated by factors higher than three or four, which can be achieved by parallel imaging compared to full k-space sampling dependent on the utilized receive coils. Ideally, the sparsity of off-resonant bins or partitions is exploited, as well as their spatial properties and the sensitivity of different receive coils to achieve at least tenfold acceleration. An acceleration technique combining parallel imaging, ORE (cf. section 3.5) and iterative reconstruction, for example compressed sensing, may have the potential to prove robust in clinical environment. As SPI for metal implant imaging is still in its infancy compared to MSI techniques, either SEMAC or MAVRIC-SL can be expected to both benefit from extremely high acceleration factors and to be accepted in clinical routine in the near future. Residual artifacts due to frequency encoding must be accepted in the current implementation of multispectral imaging. It is important to note, that the level of susceptibility artifacts depends strongly on the type of metal which the implant is manufactured of. Results in this work indicate the redundancy of MSI techniques for certain titanium implants and fixtures. Thus, different acquisition strategies should be established for different materials and suitable information should be collected prior to the imaging sequence. Either the patient's health record indicates the metal type or information about MRI related off-resonances is gathered in a scout scan. Although a detailed prediction of required SEMAC steps or off-resonance bins in MAVRIC cannot be provided on the basis of current scout implementations, the impact of the metal on the encoding process can be estimated roughly. Incorporating this information in the selection of imaging sequences and protocols, the scan time and level of artifact reduction can be balanced ideally. Optimizing the MRI procedure is one option to obtain best image quality for patients with implants. On the other hand, implant manufacturers could consider MR-related artifacts in their selection of materials. While titanium is beneficial with respect to artifacts in MRI, its physical properties do not meet the demands of weight-bearing components. Though, ceramic or ceramic-coated metal can replace femoral heads of total hip arthroplasties instead of CoCr, for example. In general, the use of ceramics for orthopedic implants is an active field of research. Though, the bulk of implants currently used by surgeons and the majority of implants distributed among the population is made of metal as described in section 3.1.2. Even though new materials with improved MRI compatibility may be used in future, the acceptance in clinical routine will be a process lasting at least a decade and the current population with metal implants must be served with MRI.

Considering latest improvements in metal implant imaging in general and for 3 T in particular, artifacts can be suppressed effectively. Still, the level of susceptibility-induced distortion will be higher at 3 T than at 1.5 T, even if high-bandwidth RF pulses are applied in both cases provided that local transmit coils are available in both cases. Shading artifacts are visible at 1.5 T, but enhanced at higher field strength. However, there are currently no commercial 1.5 T scanners, which are equipped with parallel transmit technology. Thus, this technique cannot be used to eliminate B_1 artifacts at 1.5 T and below. As long as local transmit coils are not commercially available for all orthopedic applications, the benefits in metal implant imaging at lower field strength outweigh the improvements shown in this work at 3 T. Provided that a larger variety of local transmit coils will be available in the future, routine metal implant imaging may be performed on 3 T and 1.5 T scanners likewise. Though, current methodology suggests the use of 1.5 T instead of 3 T, when scanners of both field strengths are available. Still, a radiological practice focusing on musculoskeletal

imaging with only one MR scanner should take the benefit of the higher resolution and shorter scan time provided by a 3 T scanner. Challenges arising from metal implants are no longer an obstacle at 3 T.

Bibliography

[1] D. C. Alsop, "The sensitivity of low flip angle RARE imaging", *Magnetic Resonance in Medicine*, vol. 37, no. 2, pp. 176–184, 1997.

[2] C. Armenean, E. Perrin, M. Armenean, O. Beuf, F. Pilleul, and H. Saint-Jalmes, "RF-induced temperature elevation along metallic wires in clinical magnetic resonance imaging: influence of diameter and length", *Magnetic Resonance in Medicine*, vol. 52, no. 5, pp. 1200–1206, 2004.

[3] N. S. Artz, D. Hernando, V. Taviani, A. Samsonov, J. H. Brittain, and S. B. Reeder, "Spectrally resolved fully phase-encoded three-dimensional fast spin-echo imaging", *Magnetic Resonance in Medicine*, vol. 71, no. 2, pp. 681–690, 2014.

[4] N. Artz, M. Smith, and S. Reeder, "Multiband RF excitation for accelerating magnetic resonance imaging in the presence of metal", in *Proceedings of the 22nd Annual Meeting of the ISMRM, Milan, Italy*, 2014, p. 650.

[5] T. J. Bachschmidt and M. Nittka, "Optimierung der Schichtselektion zur Reduktion von Suszeptibilitätsartefakten in der MRT", German pat. req. 102014206397.3, 2014.

[6] T. J. Bachschmidt, M. Nittka, and P. M. Jakob, "A fast and robust method for off-resonance detection in metal implant imaging", in *Proceedings of the 21st Annual Meeting of the ISMRM, Salt Lake City, USA*, 2013, p. 2561.

[7] B. J. Balcom, "SPRITE imaging of short relaxation time nuclei", in *Spatially Resolved Magnetic Resonance*. Wiley-VCH Verlag GmbH, 1998, pp. 75–86.

[8] V. Ballweg, F. Eibofner, and H. Graf, "RF tissue-heating near metallic implants during magnetic resonance examinations: An approach in the AC limit", *Medical Physics*, vol. 38, no. 10, pp. 5522–5529, 2011.

[9] K. Bartusek, Z. Dokoupil, and E. Gescheidtova, "Magnetic field mapping around metal implants using an asymmetric spin-echo MRI sequence", *Measurement Science and Technology*, vol. 17, no. 12, p. 3293, 2006.

[10] L. H. Bennett, P. S. Wang, and M. J. Donahue, "Artifacts in magnetic resonance imaging from metals", *Journal of Applied Physics*, vol. 79, no. 8, pp. 4712–4714, 1996.

[11] M. A. Bernstein, K. E. King, X. J. Zhou, and W. Fong, *Handbook of MRI Pulse Sequences*. Academic Press, 2005.

[12] M. R. van den Bosch, M. A. Moerland, J. J. W. Lagendijk, L. W. Bartels, and C. A. T. van den Berg, "New method to monitor RF safety in MRI-guided interventions

based on RF induced image artefacts", *Medical Physics*, vol. 37, no. 2, pp. 814–821, 2010.

[13] K. J. Bozic, S. M. Kurtz, E. Lau, K. Ong, V. Chiu, T. P. Vail, H. E. Rubash, and D. J. Berry, "The epidemiology of revision total knee arthroplasty in the united states", *Clinical Orthopaedics and Related Research*, vol. 468, no. 1, pp. 45–51, 2010.

[14] R. J. Brumback, S. Uwagie-Ero, R. P. Lakatos, A. Poka, G. H. Bathon, and A. R. Burgess, "Intramedullary nailing of femoral shaft fractures. Part II: Fracture-healing with static interlocking fixation", *The Journal of Bone & Joint Surgery*, vol. 70, no. 10, pp. 1453–1462, 1988.

[15] K. Butts, J. M. Pauly, and G. E. Gold, "Reduction of blurring in view angle tilting MRI", *Magnetic Resonance in Medicine*, vol. 53, no. 2, pp. 418–424, 2005.

[16] C. R. Camacho, D. B. Plewes, and R. M. Henkelman, "Nonsusceptibility artifacts due to metallic objects in MR imaging", *Journal of Magnetic Resonance Imaging*, vol. 5, no. 1, pp. 75–88, 1995.

[17] M. Carl, K. Koch, and J. Du, "MR imaging near metal with undersampled 3D radial UTE-MAVRIC sequences", *Magnetic Resonance in Medicine*, vol. 69, no. 1, pp. 27–36, 2013.

[18] H. Chang and J. M. Fitzpatrick, "A technique for accurate magnetic resonance imaging in the presence of field inhomogeneities", *Medical Imaging, IEEE Transactions on*, vol. 11, no. 3, pp. 319–329, 1992.

[19] W. Chen, P. Beatty, K. M. Koch, and A. Brau, "Parallel MRI near metallic implants", in *Proceedings of the 17th Annual Meeting of the ISMRM, Honolulu, USA*, 2009, p. 2783.

[20] Z. H. Cho, D. J. Kim, and Y. K. Kim, "Total inhomogeneity correction including chemical shifts and susceptibility by view angle tilting", *Medical Physics*, vol. 15, no. 1, pp. 7–11, 1988.

[21] S.-J. Choi, K. M. Koch, B. A. Hargreaves, K. J. Stevens, and G. E. Gold, "Metal artifact reduction with MAVRIC SL at 3-T MRI in patients with hip arthroplasty", *American Journal of Roentgenology*, vol. 204, no. 1, pp. 140–147, 2015.

[22] A. Christ, W. Kainz, E. G. Hahn, K. Honegger, M. Zefferer, E. Neufeld, W. Rascher, R. Janka, W. Bautz, J. Chen, *et al.*, "The virtual family-development of surface-based anatomical models of two adults and two children for dosimetric simulations", *Physics in Medicine and Biology*, vol. 55, no. 2, N23, 2010.

[23] S. Chung, D. Kim, E. Breton, and L. Axel, "Rapid B1+ mapping using a preconditioning RF pulse with turboflash readout", *Magnetic Resonance in Medicine*, vol. 64, no. 2, pp. 439–446, 2010.

[24] M. F. Dempsey, B. Condon, and D. M. Hadley, "Investigation of the factors responsible for burns during MRI", *Journal of Magnetic Resonance Imaging*, vol. 13, no. 4, pp. 627–631, 2001.

[25] O. Dössel, *Bildgebende Verfahren in der Medizin*. Springer Verlag, 2000.

[26] K. El Bannan, W. Handler, B. Chronik, and S. P. Salisbury, "Heating of metallic rods induced by time-varying gradient fields in MRI", *Journal of Magnetic Resonance Imaging*, vol. 38, no. 2, pp. 411–416, 2013.

[27] A. Elixhauser and R. M. Andrews, "Profile of inpatient operating room procedures in us hospitals in 2007", *Archives of Surgery*, vol. 145, no. 12, pp. 1201–1208, 2010.

[28] Y. Eryaman, B. Akin, and E. Atalar, "Reduction of implant RF heating through modification of transmit coil electric field", *Magnetic Resonance in Medicine*, vol. 65, no. 5, pp. 1305–1313, 2011.

[29] Y. Eryaman, B. Guerin, C. Akgun, J. L. Herraiz, A. Martin, A. Torrado-Carvajal, N. Malpica, J. A. Hernandez-Tamames, E. Schiavi, E. Adalsteinsson, and L. L. Wald, "Parallel transmit pulse design for patients with deep brain stimulation implants", *Magnetic Resonance in Medicine*, vol. 73, no. 5, pp. 1896–1903, 2015.

[30] Y. Eryaman, E. A. Turk, C. Oto, O. Algin, and E. Atalar, "Reduction of the radiofrequency heating of metallic devices using a dual-drive birdcage coil", *Magnetic Resonance in Medicine*, vol. 69, no. 3, pp. 845–852, 2013.

[31] C. Farrelly, A. Davarpanah, S. Brennan, M. Sampson, and S. J. Eustace, "Imaging of soft tissues adjacent to orthopedic hardware: comparison of 3-T and 1.5-T MRI", *American Journal of Roentgenology*, vol. 194, no. 1, W60–W64, 2010.

[32] M. Geetha, A. K. Singh, R. Asokamani, and A. K. Gogia, "Ti based biomaterials, the ultimate choice for orthopaedic implants–a review", *Progress in Materials Science*, vol. 54, no. 3, pp. 397–425, 2009.

[33] J. S. van Gorp, C. J. Bakker, F. Zijlstra, J. Smink, J. G. Bouwman, and P. R. Seevinck, "Geometrically undistorted imaging of orthopedic implants using compressed sensing accelerated phase encoded imaging", in *Proceedings of the 22nd Annual Meeting of the ISMRM, Milan, Italy*, 2014, p. 1680.

[34] H. Graf, U. A. Lauer, A. Berger, and F. Schick, "RF artifacts caused by metallic implants or instruments which get more prominent at 3 T: an in vitro study", *Magnetic Resonance Imaging*, vol. 23, no. 3, pp. 493–499, 2005.

[35] H. Graf, G. Steidle, P. Martirosian, U. A. Lauer, and F. Schick, "Metal artifacts caused by gradient switching", *Magnetic Resonance in Medicine*, vol. 54, no. 1, pp. 231–234, 2005.

[36] G. H. Griffin, K. J. T. Anderson, H. Celik, and G. A. Wright, "Safely assessing radiofrequency heating potential of conductive devices using image-based current measurements", *Magnetic Resonance in Medicine*, vol. 73, no. 1, pp. 427–441, 2015.

[37] M. A. Griswold, P. M. Jakob, R. M. Heidemann, M. Nittka, V. Jellus, J. Wang, B. Kiefer, and A. Haase, "Generalized autocalibrating partially parallel acquisitions (GRAPPA)", *Magnetic Resonance in Medicine*, vol. 47, no. 6, pp. 1202–1210, 2002.

[38] A. Guermazi, Y. Miaux, S. Zaim, C. G. Peterfy, D. White, and H. K. Genant, "Metallic artefacts in MR imaging: effects of main field orientation and strength", *Clinical Radiology*, vol. 58, no. 4, pp. 322–328, 2003.

[39] L. B. Gutierrez, B. H. Do, G. E. Gold, B. A. Hargreaves, K. M. Koch, P. W. Worters, and K. J. Stevens, "MR imaging near metallic implants using MAVRIC SL", *Academic Radiology*, vol. 22, no. 3, pp. 370–379, 2015.

[40] E. M. Haacke, R. W. Brown, M. R. Thompson, and R. Venkatesan, *Magnetic Resonance Imaging: Physical Principles and Sequence Design*. John Wiley & Sons, Inc., 1999.

[41] N. P. Hailer, G. Garellick, and J. Kärrholm, "Uncemented and cemented primary total hip arthroplasty in the swedish hip arthroplasty register: evaluation of 170,413 operations", *Acta Orthopaedica*, vol. 81, no. 1, pp. 34–41, 2010.

[42] C. den Harder, U. A. Blume, and C. Bos, "MR imaging near orthopedic implants using slice-encoding for metal artifact correction and off-resonance suppression", in *Proceedings of the 19th Annual Meeting of the ISMRM, Montreal, Canada*, 2011, p. 3170.

[43] C. den Harder, G. H. van Yperen, U. A. Blume, and C. Bos, "Off-resonance suppression for multispectral MR imaging near metallic implants", *Magnetic Resonance in Medicine*, vol. 73, no. 1, pp. 233–243, 2015.

[44] C. den Harder, G. H. van Yperen, U. A. Blume, and C. Bos, "Ripple artifact reduction using slice overlap in slice encoding for metal artifact correction", *Magnetic Resonance in Medicine*, vol. 73, no. 1, pp. 318–324, 2015.

[45] B. A. Hargreaves, G. E. Gold, J. M. Pauly, and K. B. Pauly, "Adaptive slice encoding for metal artifact correction", in *Proceedings of the 18th Annual Meeting of the ISMRM, Stockholm, Sweden*, 2010, p. 3083.

[46] B. A. Hargreaves, W. Chen, W. Lu, M. T. Alley, G. E. Gold, A. Brau, J. M. Pauly, and K. B. Pauly, "Accelerated slice encoding for metal artifact correction", *Journal of Magnetic Resonance Imaging*, vol. 31, no. 4, pp. 987–996, 2010.

[47] B. A. Hargreaves, P. W. Worters, K. B. Pauly, J. M. Pauly, K. M. Koch, and G. E. Gold, "Metal-induced artifacts in MRI", *American Journal of Roentgenology*, vol. 197, no. 3, pp. 547–555, 2011.

[48] O. Heid and M. Deimling, "Rapid single point (RASP) imaging", in *Proceedings of the 3rd SMR Annual Meeting, Nice, France*, 1995, p. 684.

[49] J. Hennig, "Multiecho imaging sequences with low refocusing flip angles", *Journal of Magnetic Resonance*, vol. 78, no. 3, pp. 397 –407, 1988.

[50] J. Hennig, A. Nauerth, and H. Friedburg, "RARE imaging: a fast imaging method for clinical MR", *Magnetic Resonance in Medicine*, vol. 3, no. 6, pp. 823–833, 1986.

[51] D. I. Hoult, "The principle of reciprocity in signal strength calculations - A mathematical guide", *Concepts in Magnetic Resonance*, vol. 12, no. 4, pp. 173–187, 2000.

[52] International Electrotechnical Commission (IEC), "Medical electrical equipment: Part 2-33. Particular requirements for the safety of magnetic resonance equipment for medical diagnosis", *IEC 60601-2-33 ed 2.2. Consolidated with amendments 1 and 2*, 2008.

[53] P. Jezzard and R. S. Balaban, "Correction for geometric distortion in echo planar images from B0 field variations", *Magnetic Resonance in Medicine*, vol. 34, no. 1, pp. 65–73, 1995.

[54] K. M. Koch, A. C. Brau, W. Chen, G. E. Gold, B. A. Hargreaves, M. Koff, G. C. McKinnon, H. G. Potter, and K. F. King, "Imaging near metal with a MAVRIC-SEMAC hybrid", *Magnetic Resonance in Medicine*, vol. 65, no. 1, pp. 71–82, 2011.

[55] K. M. Koch, B. A. Hargreaves, K. B. Pauly, W. Chen, G. E. Gold, and K. F. King, "Magnetic resonance imaging near metal implants", *Journal of Magnetic Resonance Imaging*, vol. 32, no. 4, pp. 773–787, 2010.

[56] K. M. Koch, R. Hinks, and K. King, "Empirical and computed B0 perturbations induced by metallic implants", in *Proceedings of the 16th Annual Meeting of the ISMRM, Toronto, Canada*, 2008, p. 1180.

[57] K. M. Koch and K. F. King, "Combined parallel imaging and compressed sensing on 3D multi-spectral imaging near metal implants", in *Proceedings of the 19th Annual Meeting of the ISMRM, Montreal, Canada*, 2011, p. 3172.

[58] K. M. Koch, M. A. Koff, and H. G. Potter, "Jacobian-based correction of 3D-MSI images near implanted metal devices", in *Proceedings of the 19th Annual Meeting of ISMRM, Montreal, Canada*, 2011, p. 3173.

[59] K. M. Koch, K. F. King, and M. G. C., "B1 effects when imaging near metal implants at 3T", in *Proceedings of the 18th Annual Meeting of the ISMRM, Stockholm, Sweden*, 2010, p. 3082.

[60] K. M. Koch, K. F. King, M. Carl, and B. A. Hargreaves, "Imaging near metal: the impact of extreme static local field gradients on frequency encoding processes", *Magnetic Resonance in Medicine*, vol. 71, no. 6, pp. 2024–2034, 2014.

[61] K. M. Koch, J. E. Lorbiecki, R. S. Hinks, and K. F. King, "A multispectral three-dimensional acquisition technique for imaging near metal implants", *Magnetic Resonance in Medicine*, vol. 61, no. 2, pp. 381–390, 2009.

[62] K. M. Koch and G. C. McKinnon, "On the feasibility of overcoming frequency encoding limitations near metal implants with broadband single-point imaging on clinical MR systems", in *Proceedings of the 22nd Annual Meeting of the ISMRM, Milan, Italy*, 2014, p. 1679.

[63] M. Kretzschmar, L. Nardo, M. M. Han, U. Heilmeier, C. Sam, G. B. Joseph, K. M. Koch, R. Krug, and T. M. Link, "Metal artefact suppression at 3 T MRI: comparison of MAVRIC-SL with conventional fast spin echo sequences in patients with hip joint arthroplasty", *European Radiology*, pp. 1–9, 2015.

[64] R. Kuo, M. Panchal, L. Tanenbaum, and J. V. Crues, "3.0 Tesla imaging of the musculoskeletal system", *Journal of Magnetic Resonance Imaging*, vol. 25, no. 2, pp. 245–261, 2007.

[65] S. Kurtz, F. Mowat, K. Ong, N. Chan, E. Lau, and M. Halpern, "Prevalence of primary and revision total hip and knee arthroplasty in the united states from 1990 through 2002", *The Journal of Bone & Joint Surgery*, vol. 87, no. 7, pp. 1487–1497, 2005.

[66] S. Kurtz, K. Ong, E. Lau, F. Mowat, and M. Halpern, "Projections of primary and revision hip and knee arthroplasty in the united states from 2005 to 2030", *The Journal of Bone & Joint Surgery*, vol. 89, no. 4, pp. 780–785, 2007.

[67] M. E. Ladd, P. Erhart, J. F. Debatin, B. J. Romanowski, P. Boesiger, and G. C. McKinnon, "Biopsy needle susceptibility artifacts", *Magnetic Resonance in Medicine*, vol. 36, no. 4, pp. 646–651, 1996.

[68] U. A. Lauer, H. Graf, A. Berger, C. D. Claussen, and F. Schick, "Radio frequency versus susceptibility effects of small conductive implants - a systematic MRI study on aneurysm clips at 1.5 and 3 T", *Magnetic Resonance Imaging*, vol. 23, no. 4, pp. 563–569, 2005.

[69] M.-J. Lee, S. Kim, S.-A. Lee, H.-T. Song, Y.-M. Huh, D.-H. Kim, S. H. Han, and J.-S. Suh, "Overcoming artifacts from metallic orthopedic implants at high-field-strength MR Imaging and multi-detector CT", *Radiographics*, vol. 27, no. 3, pp. 791–803, 2007.

[70] M. H. Levitt, *Spin dynamics: Basics of Nuclear Magnetic Resonance*. John Wiley & Sons, Inc., 2001.

[71] G. Li, M. Nittka, D. Paul, and W. Zhang, "Distortion scout in metal implants imaging", in *Proceedings of the 19th Annual Meeting of the ISMRM, Montreal, Canada*, 2011, p. 3169.

[72] G. Li, M. Nittka, D. Paul, and L. Lauer, "MSVAT-SPACE for fast metal implants imaging", in *Proceedings of the 19th Annual Meeting of the ISMRM, Montreal, Canada*, 2011, p. 3171.

[73] G. Li, B. Zhang, H. Guo, and Q. Zhang, "BLADE-VAT for geometric distortion correction", in *Proceedings of the 16th Annual Meeting of the ISMRM, Toronto, Canada*, 2008, p. 1355.

[74] H. Liebl, U. Heilmeier, S. Lee, L. Nardo, J. Patsch, C. Schuppert, M. Han, I.-C. Rondak, S. Banerjee, K. Koch, *et al.*, "In vitro assessment of knee MRI in the presence of metal implants comparing MAVRIC-SL and conventional fast spin echo sequences at 1.5 and 3 T field strength", *Journal of Magnetic Resonance Imaging*, vol. 41, no. 5, pp. 1291–1299, 2015.

[75] C.-Y. Liu, K. Farahani, D. S. K. Lu, G. Duckwiler, and A. Oppelt, "Safety of MRI-guided endovascular guidewire applications", *Journal of Magnetic Resonance Imaging*, vol. 12, no. 1, pp. 75–78, 2000.

[76] Y. Liu, J. Chen, F. G. Shellock, and W. Kainz, "Computational and experimental studies of an orthopedic implant: MRI-related heating at 1.5-T/64-MHz and 3-T/128-MHz", *Journal of Magnetic Resonance Imaging*, vol. 37, no. 2, pp. 491–497, 2013.

[77] M. Long and H. J. Rack, "Titanium alloys in total joint replacement-a materials science perspective", *Biomaterials*, vol. 19, no. 18, pp. 1621–1639, 1998.

[78] W. Lu, K. B. Pauly, G. E. Gold, J. M. Pauly, and B. A. Hargreaves, "Compressive slice encoding for metal artifact correction", in *Proceedings of the 18th Annual Meeting of the ISMRM, Stockholm, Sweden*, 2010, p. 3079.

[79] W. Lu, K. B. Pauly, G. E. Gold, J. M. Pauly, and B. A. Hargreaves, "Slice encoding for metal artifact correction with noise reduction", *Magnetic Resonance in Medicine*, vol. 65, no. 5, pp. 1352–1357, 2011.

[80] W. Lu, K. B. Pauly, G. E. Gold, J. M. Pauly, and B. A. Hargreaves, "SEMAC: slice encoding for metal artifact correction in MRI", *Magnetic Resonance in Medicine*, vol. 62, no. 1, pp. 66–76, 2009.

[81] M. Lustig, D. Donoho, and J. M. Pauly, "Sparse MRI: the application of compressed sensing for rapid MR imaging", *Magnetic Resonance in Medicine*, vol. 58, no. 6, pp. 1182–1195, 2007.

[82] T. Miclau and R. E. Martin, "The evolution of modern plate osteosynthesis", *Injury*, vol. 28, A3–A6, 1997.

[83] M. M. Mikhael, A. D. Hanssen, and R. J. Sierra, "Failure of metal-on-metal total hip arthroplasty mimicking hip infectiona report of two cases", *The Journal of Bone & Joint Surgery*, vol. 91, no. 2, pp. 443–446, 2009.

[84] U. D. Monu, P. W. Worters, K. Sung, K. M. Koch, G. E. Gold, and B. A. Hargreaves, "B1 mapping near metallic implants", in *Proceedings of the 19th Annual Meeting of the ISMRM, Montreal, Canada*, 2011, p. 3175.

[85] H. Muranaka, T. Horiguchi, Y. Ueda, S. Usui, N. Tanki, and O. Nakamura, "Evaluation of RF heating on hip joint implant in phantom during MRI examinations.", *Nihon Hoshasen Gijutsu Gakkai Zasshi*, vol. 66, no. 7, pp. 725–733, 2010.

[86] H. Muranaka, T. Horiguchi, S. Usui, Y. Ueda, O. Nakamura, and F. Ikeda, "Dependence of RF heating on SAR and implant position in a 1.5 T MR system", *Magnetic Resonance in Medical Sciences*, vol. 6, no. 4, pp. 199–209, 2007.

[87] A. M. Naraghi and L. M. White, "Magnetic resonance imaging of joint replacements", in *Seminars in Musculoskeletal Radiology*, vol. 10, 2006, pp. 098–106.

[88] M. Nittka, R. Otazo, L. D. Rybak, K. T. Block, C. Geppert, D. K. Sodickson, and M. P. Recht, "Highly accelerated SEMAC metal implant imaging using joint compressed sensing and parallel imaging", in *Proceedings of the 21st Annual Meeting of the ISMRM, Salt Lake City, USA*, 2013, p. 2561.

[89] W. R. Nitz, G. Brinker, D. Diehl, and G. Frese, "Specific absorption rate as a poor indicator of magnetic resonance-related implant heating", *Investigative Radiology*, vol. 40, no. 12, pp. 773–776, 2005.

[90] W. R. Nitz, A. Oppelt, W. Renz, C. Manke, M. Lenhart, and J. Link, "On the heating of linear conductive structures as guide wires and catheters in interventional MRI", *Journal of Magnetic Resonance Imaging*, vol. 13, no. 1, pp. 105–114, 2001.

[91] P. Nordbeck, I. Weiss, P. Ehses, O. Ritter, M. Warmuth, F. Fidler, V. Herold, P. M. Jakob, M. E. Ladd, H. H. Quick, *et al.*, "Measuring RF-induced currents inside implants: impact of device configuration on MRI safety of cardiac pacemaker leads", *Magnetic Resonance in Medicine*, vol. 61, no. 3, pp. 570–578, 2009.

[92] J. Olsrud, J. Lätt, S. Brockstedt, B. Romner, and I. M. Björkman-Burtscher, "Magnetic resonance imaging artifacts caused by aneurysm clips and shunt valves: depen-

dence on field strength (1.5 and 3 T) and imaging parameters", *Journal of Magnetic Resonance Imaging*, vol. 22, no. 3, pp. 433–437, 2005.

[93] W. R. Overall, J. M. Pauly, P. P. Stang, and G. C. Scott, "Ensuring safety of implanted devices under MRI using reversed RF polarization", *Magnetic Resonance in Medicine*, vol. 64, no. 3, pp. 823–833, 2010.

[94] J. B. Park and J. D. Bronzino, *Biomaterials: Principles and Applications*. crc press, 2002.

[95] D. Paul, K. Liu, and T. J. Bachschmidt, "SEMAC-based metal scout", U.S. pat. req. 61/918,786, 2014.

[96] J. Pauly, P. Le Roux, D. Nishimura, and A. Macovski, "Parameter relations for the Shinnar-Le Roux selective excitation pulse design algorithm [NMR imaging]", *Medical Imaging, IEEE Transactions on*, vol. 10, no. 1, pp. 53–65, 1991.

[97] J. Powell, A. Papadaki, J. Hand, A. Hart, and D. McRobbie, "Numerical simulation of SAR induced around Co-Cr-Mo hip prostheses in situ exposed to RF fields associated with 1.5 and 3 T MRI body coils", *Magnetic Resonance in Medicine*, vol. 68, no. 3, pp. 960–968, 2012.

[98] M. N. Rahaman, A. Yao, B. S. Bal, J. P. Garino, and M. D. Ries, "Ceramics for prosthetic hip and knee joint replacement", *Journal of the American Ceramic Society*, vol. 90, no. 7, pp. 1965–1988, 2007.

[99] P. Ramos-Cabrer, J. P. M. Van Duynhoven, A. Van der Toorn, and K. Nicolay, "MRI of hip prostheses using single-point methods: in vitro studies towards the artifact-free imaging of individuals with metal implants", *Magnetic Resonance Imaging*, vol. 22, no. 8, pp. 1097–1103, 2004.

[100] M. Rea, X. Boullier, I. Young, and D. McRobbie, "Phase encoded acquisition with compressed sensing", in *Proceedings of the 22nd Annual Meeting of the ISMRM, Milan, Italy*, 2014, p. 1509.

[101] M. D. Robson, P. D. Gatehouse, M. Bydder, and G. M. Bydder, "Magnetic resonance: an introduction to ultrashort TE (UTE) imaging", *Journal of Computer Assisted Tomography*, vol. 27, no. 6, pp. 825–846, 2003.

[102] J. Ruoff, C. Würslin, H. Graf, and F. Schick, "Resolution adapted finite element modeling of radio frequency interactions on conductive resonant structures in MRI", *Magnetic Resonance in Medicine*, vol. 67, no. 5, pp. 1444–1452, 2012.

[103] G. Schäfers and H. Kugel, "A basic investigation of heating effects on total hip prostheses in combination with a simulated skin contact of the inner thighs during magnetic resonance imaging (MRI) with an 1.5 Tesla MR system", in *Proceedings ISMRM Workshop on MRI Safety: Update, Practical Information and Future Implications*, 2005.

[104] J. F. Schenck, "The role of magnetic susceptibility in magnetic resonance imaging: MRI magnetic compatibility of the first and second kinds", *Medical Physics*, vol. 23, no. 6, pp. 815–850, 1996.

[105] J. Schöpfer, K. Huber, S. Biber, S. Martius, and H. Greim, "A novel design approach for planar local transmit/receive antennas in 3T spine imaging", in *Proceedings of the 22nd Annual Meeting of the ISMRM, Milan, Italy*, 2014, p. 1313.

[106] L. Shapiro, M. Harish, B. Hargreaves, E. Staroswiecki, and G. Gold, "Advances in musculoskeletal MRI: technical considerations", *Journal of Magnetic Resonance Imaging*, vol. 36, no. 4, pp. 775–787, 2012.

[107] L. Shapiro, E. Staroswiecki, and G. Gold, "MRI of the knee: optimizing 3T imaging", in *Seminars in Roentgenology*, NIH Public Access, vol. 45, 2010, p. 238.

[108] A. Shenhav and H. Azhari, "Gradient field switching as a source for artifacts in MR imaging of metallic stents", *Magnetic Resonance in Medicine*, vol. 52, no. 6, pp. 1465–1468, 2004.

[109] M. R. Smith, N. S. Artz, K. M. Koch, A. Samsonov, and S. B. Reeder, "Accelerating sequences in the presence of metal by exploiting the spatial distribution of off-resonance", *Magnetic Resonance in Medicine*, vol. 72, no. 6, pp. 1658–1667, 2014.

[110] M. R. Smith, N. S. Artz, C. Wiens, D. Hernando, and S. B. Reeder, "Characterizing the limits of MRI near metallic prostheses", *Magnetic Resonance in Medicine*, 2014.

[111] R. Sutter, R. Hodek, S. F. Fucentese, M. Nittka, and C. W. A. Pfirrmann, "Total knee arthroplasty MRI featuring slice-encoding for metal artifact correction: reduction of artifacts for STIR and proton density–weighted sequences", *American Journal of Roentgenology*, vol. 201, no. 6, pp. 1315–1324, 2013.

[112] B. Sveinsson, P. W. Worters, G. E. Gold, and B. A. Hargreaves, "Hexagonal undersampling for faster MRI near metallic implants", *Magnetic Resonance in Medicine*, vol. 73, no. 2, pp. 662–668, 2015.

[113] J. Tropp, "Image brightening in samples of high dielectric constant", *Journal of Magnetic Resonance*, vol. 167, no. 1, pp. 12–24, 2004.

[114] E. J. Ulbrich, R. Sutter, R. F. Aguiar, M. Nittka, and C. W. Pfirrmann, "STIR sequence with increased receiver bandwidth of the inversion pulse for reduction of metallic artifacts", *American Journal of Roentgenology*, vol. 199, no. 6, W735–W742, 2012.

[115] J. E. Vandevenne, F. M. Vanhoenacker, P. M. Parizel, K. B. Pauly, and P. K. Lang, "Reduction of metal artefacts in musculoskeletal MR imaging", *JBR BTR*, vol. 90, no. 5, p. 345, 2007.

[116] S. Wong, L. Steinbach, J. Zhao, C. Stehling, C. B. Ma, and T. M. Link, "Comparative study of imaging at 3.0 T versus 1.5 T of the knee", *Skeletal Radiology*, vol. 38, no. 8, pp. 761–769, 2009.

[117] A. D. Woolf and B. Pfleger, "Burden of major musculoskeletal conditions", *Bulletin of the World Health Organization*, vol. 81, no. 9, pp. 646–656, 2003.

[118] P. W. Worters, K. Sung, K. J. Stevens, K. M. Koch, and B. A. Hargreaves, "Compressed-sensing multispectral imaging of the postoperative spine", *Journal of Magnetic Resonance Imaging*, vol. 37, no. 1, pp. 243–248, 2013.

[119] C. J. Yeung, P. Karmarkar, and E. R. McVeigh, "Minimizing RF heating of conducting wires in MRI", *Magnetic Resonance in Medicine*, vol. 58, no. 5, pp. 1028–1034, 2007.

[120] S. Y. Zho and D. H. Kim, "Spiral imaging with view angle tilting for application to metal artifact correction", in *Proceedings of the 19th Annual Meeting of the ISMRM, Montreal, Canada*, 2011, p. 4618.

[121] S. Y. Zho, M. O. Kim, K. W. Lee, and D. H. Kim, "Artifact reduction from metallic dental materials in T1-weighted spin-echo imaging at 3.0 Tesla", *Journal of Magnetic Resonance Imaging*, vol. 37, no. 2, pp. 471–478, 2013.

List of Publications

Journal Articles

- Polarized Multi-Channel Transmit MRI to Reduce Shading near Metal Implants. Bachschmidt T, Köhler M, Nistler J, Geppert C, Jakob P, Nittka M. Magnetic Resonance in Medicine, doi: 10.1002/mrm.25621.

- Knee Implant Imaging at 3T using High-Bandwidth RF Pulses. Bachschmidt T, Sutter R, Jakob P, Pfirrmann C, Nittka M. Journal of Magnetic Resonance Imaging, vol. 41, no. 6, pp. 1570-1580, 2015. doi: 10.1002/jmri.24729.

Conference Contributions

- Imaging of the Spine with Metal Implants Using High-Bandwidth RF Pulses from a Local Tx/Rx Coil. Bachschmidt T, Schöpfer J, Biber S, Jakob P, Nittka M. In: Proceedings of ISMRM, Toronto, 2015, p.2507.

- Correlation of improved local SAR deposition with reduced shading close to hip implants. Lottner T, Nittka M, Bachschmidt T, Meyer H, Nitz W. In: Proceedings of ISMRM, Toronto, 2015, p.1860.

- Polarized Multi-Channel Transmit MRI to Reduce B1-Shading near Metal Implants. Bachschmidt T, Jakob P, Vester M, Nistler J, Nittka M. In: Proceedings of ISMRM, Milan, 2014, p.1675.

- Improved Imaging of Total Knee Arthroplasty (TKA) at 3T Using High-Bandwidth RF Pulses. Bachschmidt T, Jakob P, Sutter R, Nittka M. In: Proceedings of ESMRMB, Toulouse, 2013, p.411.

- A Fast and Robust Method for Off-Resonance Detection in Metal Implant Imaging. Bachschmidt T, Nittka M, Jakob P. In: Proceedings of ISMRM, Salt Lake City, 2013, p.2561.

- Narrowband Excitation for Simultaneous 3D MRI of Separated Fat and Water. Bachschmidt T, Fautz H, Gumbrecht R, Quick H, Paul D. In: Tagungsband der Jahrestagung DS-ISMRM, Berlin, 2011, p.P3.

Patents

- Fat-Water Separation in SPACE using band-selective excitation. Paul D, Fautz H, Gumbrecht R, Bachschmidt T. 2011P27582 DE patent granted (02/27/2014). US, CN patent published. JP, KR patent pending.

- Schnelle und robuste Methode zur Quantifikation von starken Off-Resonanzen in der MRT. Bachschmidt T, Nittka M. 2013P01477 DE patent granted (11/20/2014). US, CN patent published. KR patent pending.

- Reduzierung von B1-Artefakten in der Nähe von länglichen Metallformen durch die Verwendung von parallel Transmit in der Magnetresonanztomographie. Bachschmidt T, Nittka M. 2013P09745 DE, US patent published. CN, JP, KR patent pending.

- Paul D, Liu K, Bachschmidt T. 2013P27290 US patent pending.

- Bachschmidt T, Paul D. 2014P04224 DE patent pending.

- Bachschmidt T, Nittka M. 2014P03798 DE patent pending.

- Bachschmidt T, Nittka M. 2014P18133 DE patent pending.

- Grodzki D, Raithel E, Meyer H, Nittka M, Bachschmidt T. 2014P20209 DE patent pending.

- Bachschmidt T, Nittka M, Fenchel M, Jakoby B. 2014E17278 DE patent pending.

Acknowledgements

The work described here is the result of collaborations with a number of individuals that I would like to acknowledge for their support and assistance over the past years. I would particularly like to express my gratitude to my thesis advisors Prof. Dr. Peter Jakob of the University of Würzburg and Dr. Mathias Nittka, employee of Siemens AG, for their continuous loyalty, support and kindness. Their advices and ideas considerably helped me during my research and diverse and fruitful discussions enriched my work. It has been a privilege and an honor to work under their supervision.

I am also indebted to many MR hardware and software specialists who shared their knowledge generously. I would like to thank

- Dr. Markus Vester for his incessant attempt to transform an an engineer's perspective of electromagnetic questions into a physicist's perspective
- Jürgen Nistler for his comprehensive instructions for numerical modeling
- Dr. Stefan Biber and Johanna Schöpfer for the successful consolidation of hardware and software prototypes
- and Dr. Michael Köhler for the introduction to efficient B_1-mapping in the presence of metal.

I would like to thank Siemens AG gratefully for funding this project. Special thanks go to Dr. Heiko Meyer for his commitment to feature my results and to enable international collaborations, which enriched my work over the past years.

I would like to thank PD Dr. Reto Sutter and Prof. Dr. Christian Pfirrmann, MBA, of the Orthopedic University Hospital Balgrist, Zurich, for sharing their clinical perspective on the impact of high-bandwidth RF pulses. My thanks also belong to the Department of Radiology at New York University for hosting me during the soccer world cup 2014. In particular, I would like to thank Dr. Christian Geppert, Dr. David Faul, Mary Bruno, Dr. Martijn Cloos, Prof. Dr. Fernando Boada and Prof. Dr. Daniel Sodickson for their support, divers discussions and helpful advices.

At last, I want to give my personal thanks to my friends and my family who supported me in many ways. Special thanks belong to Sebastian for his encouragement and patience. I complete this thesis in memory of my father.